TU Delft

eternalsunspire

REDUCING MEASUREMENT UNCERTAINTY OF TEMPERATURE COEFFICIENTS OF PHOTOVOLTAIC MODULES

Tijmen Slikker

Reducing measurement uncertainty of temperature coefficients of Photovoltaic Modules

by

Tijmen Slikker

to obtain the degree of Master of Science
at the Delft University of Technology,
to be defended publicly on Thursday June 4, 2020 at 15:00 PM

Student number: 4163516
Project duration: January 2019 - June 2020

Thesis committee:
Dr. Olindo Isabella, TU Delft PVMD group, chair
Dr. Patrizio Manganiello, TU Delft PVMD group, TU Delft daily supervisor
Dr. Gautham Ram Chandra Mouli, TU Delft DCE&S Group
Stefan Roest, CTO Eternalsun Spire, company supervisor

An electronic version of this thesis is available at http://repository.tudelft.nl/.

Preface

After encountering measurement uncertainty in practice during my internship at Eternalsun Spire, this project has enabled me to learn so much more about the underlying components and propagation into the measurements. I hope that this work can support PV industry and function as reference material to reduce the measurement uncertainty of temperature coefficients of PV modules and reduce financial risk for utility scale PV projects. Hereby I would like to thank my supervisors Dr. Olindo Isabella, Dr. Patrizio Manganiello and especially my company supervisor Stefan Roest for all the feedback and guidance during this thesis. Also I owe my gratitude to my colleagues at Eternalsun Spire, who would always get out of their way to help me with any problem and would support me when I needed it. Because of you I've learned so much more than expected and you've helped me to become a better engineer in the widest sense of the word. I would also like to thank Dr. Heusdens for the exchange of thoughts on the developed uncertainty model, as well as Dr. Muellejans and Dr. Mihaylov for the valuable insights they gave me in their work and uncertainty analyses in general.

Abstract

In temperature coefficient measurements of PV modules, a low level of agreement in results is observed between different laboratories, with deviations up to $\pm 10\%$ for P_{max} temperature coefficients. Such deviations are considered as an uncertainty component in PV energy yield assessments, and are seen as financial risk by investors and purchasers. A $\pm 10\%$ error in the P_{max} temperature coefficient can result in more than 1% error in estimated energy yield (and thus financial return on investment), which is significant especially for utility scale PV. The goal of this work is to reduce the uncertainty of the P_{max} temperature coefficients from $\pm 10\%$ down to $\pm 5\%$, which will reduce financial risk and therefore support the roll-out of utility scale PV.

This thesis will focus on identification and reduction of measurement uncertainty of the temperature coefficients. A measurement setup for PV module temperature coefficients, integrating a solar simulator and a temperature chamber, was developed by Eternalsun Spire. This setup will be evaluated using a Monte Carlo based uncertainty analysis. Additionally, uncertainty drivers - relevant for current, typical industry practice - will be demonstrated, contributing to further understanding of observed deviations between temperature coefficient measurement results from different laboratories.

The k=2 expanded measurement uncertainty for the relative temperature coefficient for a PV module measured in the Temperature Coefficient Lab Flasher is approximated at 4.05%. Three major uncertainty components are: 1. Temperature induced spectral mismatch (2.46%) 2. STC uncertainty of the solar simulator (1.09%); 3. Temperature correction of the monitor cell (0.41%). Additionally, it is demonstrated that: 1. silicon heterojunction PV modules can exhibit non-linear temperature behaviour and therefore coefficients that are dependent on the range of measurement; 2. significant measurement errors can occur when the cell temperature and backsheet temperature are not in thermal equilibrium, which typically applies for the currently widely applied ”hot potato” method for determination of temperature coefficients; 3. the simulator spectrum can significantly affect the temperature coefficient measurement even for solar simulators with A+ rating for spectral match.

Based on the uncertainty analysis it is shown that the temperature coefficient measurement setup can be used to achieve a measurement uncertainty of PV module temperature coefficients below 5%. Additionally, the demonstrated uncertainty drivers encountered in typical industry practice can support awareness and thus mitigation of uncertainty drivers previously not aware of. For this purpose, recommendations from this work have been included in an international IEC standard for measurement of temperature coefficients.

List of Figures

List of Tables

Contents

1 Introduction

1.1 The energy problem

Global energy consumption has been increasing approximately 2 percent a year for the last 30 years as a result of economic growth and increasing population [9]. Most of the future energy scenarios predict this growth to continue for the next few decades [10][11]. This continuous increase in consumption creates new challenges with respect to energy security and environmental issues.

Currently the majority of energy production relies on non-renewable fossil fuel sources, which are being consumed in a pace order of magnitudes higher than they are growing. While there are still increases in efficiency and cost-effectivity of extraction and conversion of these resources, it is expected the world will run out of (affordable) fossil based resources [12] within this or next century. This can have enormous impact on daily life, as energy is one of the fundamentals for economic activity in modern societies. In general, the higher the living standard in a country, the more energy is being used per capita. As energy and economy are interdependent, it is not surprising even brief moments of energy shortage can have large effects on local economies [13]. It is of high importance for society to adapt and ensure high levels of energy security considering the depletion of fossil fuel sources.

The depletion of these sources is not the only problem foreseeable in the near future as there is also a large environmental effect to consider. Many of these fossil fuels are based on hydrocarbons formed in the crust of the earth over the last hundreds of millions of years as a result of pressure and heat. Burning these fuels breaks up these compounds, releasing stored energy. A downside of this process is the formation of so called greenhouse gases, of which the most commonly known is carbon dioxide, CO_2. A large part of these greenhouse gases are stored in the atmosphere, increasing its thermally insulating properties. While the CO_2 concentration present in the atmosphere undergoes natural fluctuations, an excessively high increase in CO_2 concentration is observed in the last few hundred years. Since this coincidences with the start of the industrial era, also the start of larger scale fossil fuel consumption, this increase is likely the result of human activities. Together with the increased CO_2 concentration, increasing temperatures have also been observed as shown in Figure 1. Effects of this increased thermal insulation by the atmosphere have become more evident over the last decades [14]. Average temperatures have been slowly rising and for 2050 an average temperature increase over 2 degrees compared to pre-industrial levels is expected. This is however only one effect of the changing climate [15]. Extreme temperatures are likely to occur both more severe and more often, sea levels will rise, droughts will occur more often and in larger regions and many more effects on the climate are expected.

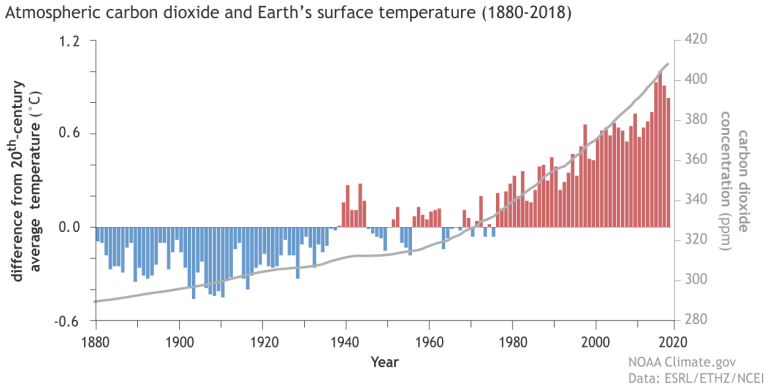

Figure 1: Temperature difference from 20^{th}-century average compared to atmospheric carbon dioxide concentration. Data from NOAA NCEI, IAC and NOAA ESRL. Original graph: Dr. Howard Diamond NOAA ARL, adapted by NOAA Climate.gov

These effects will not be limited to climate and environment, but can have major impacts on social well-being in many areas. Rising sea levels reduce the availability of fresh water, increasing already existing conflicts over the ownership of water. Land areas will become unsuitable to grow food putting pressure on local food security and prices, large numbers of people will be forced to move and find a more suitable place to live. These are a few of the foreseen consequences, however one can imagine serious social tensions as a result, which will likely only be enlarged when the availability of energy (as a result of fossil fuel depletion) becomes problematic. Aforementioned consequences will have the most impact on those that are the least able to adapt [16], which is generally the less privileged part of the worlds' society. So an indirect consequence could be an even further increase in the already growing wealth gap in the world.

It should be clear there is a need for affordable, reliable, renewable, sustainable, clean energy sources. One of the energy sources that is expected to play a major part in the future energy mix is solar energy [17].

1.2 Overcoming the energy problem: Solar Energy

The sun is by far the largest source of energy available on earth, providing sufficient energy to cover more than 1000 times the current global energy consumption at any moment. Therefore, much effort is put in converting this solar energy into energy usable for general purposes. One of the most commonly used methods to perform this conversion is by the use of photovoltaic technology. This technology is mostly encountered in the form of a photovoltaic module and exploits the photovoltaic effect: a process where radiation is converted into electricity.

Figure 2: PV modules in the field; Illustration by: Gemeente Houten, accessed 30/10/2019, www.zonneveldenhouten.nl/zonnevelden/voorbeelden-zonnevelden/

While photovoltaic devices have already been under development and applied in space industry for many years, energy produced by photovoltaic devices can be offered to the market at competitive prices only since the last few years. The amount of installed PV modules is increasing at an almost exponential level [18], while the system price keeps decreasing as a result of advances in technology and upscaling of the industry.

Photovoltaic devices have a much lower carbon footprint compared to fossil fuels. As the PV device does not require burning fossil fuels to produce energy, the full carbon footprint is related to the production and recycling of the module. As a result, the carbon footprint of PV electricity is much lower compared to electricity from fossil fuel sources and mainly depends on the fuels used in the supply chain itself [19]. At the end of life of a PV module, which is typically 20 to 30 years, a large part of the materials can already be recycled; however still a lot of effort is needed to improve the efficiency of the recycling processes [20]. From a sustainability point of view, one could even argue to optimize the recyclability of the module and cells rather than optimizing the energy yield.

Photovoltaics can also introduce opportunities for developing countries. In a large part of these countries, the climate offers great potential for photovoltaics. Compared to conventional, fossil based technologies, renewable energies and especially PV modules create significantly more jobs per unit of created energy [21]. As photovoltaics can be implemented at both small and large scale and at almost every location, there is a lot of flexibility in where to create these jobs. This independence on location offers more advantages. Unlike the developed countries, a properly functioning electricity grid is often not self-evident. Transport losses can be significant and often the grid is sensitive to failures. This independence also solves issues where utility systems are centrally owned by less stable governments, where political instability can introduce large fluctuations in electricity price.

Despite the many advantages of photovoltaic energy, there are also some important challenges that need to be overcome before PV can replace fossil based energy generation. Probably the most important is the storage of energy. PV energy generation is intermittent, it follows a daily and seasonal pattern. There is no sun, thus no energy, during the evening and night and there is generally less sun in winter compared to the summer. Also, periods can occur where the sky is clouded for weeks and less energy is generated than usual or vice versa. To overcome these issues, both short and long term storage of energy are required. The development of large scale, efficient and sustainable ways to store energy will likely be one of the major challenges for the coming decades. Energy storage is not only a requirement for PV, but is one of the main requirements for a future based on renewable energies.

Photovoltaics will very likely play an important role in a future based on renewable energy generation and can be a key ingredient to overcome the energy problem. While it is financially interesting for the western world, there are additional advantages for emerging economies. With the low carbon footprint and competitive price, energy storage is currently the main challenge for large scale implementation of photovoltaics.

1.3 Bankability of Solar Energy projects: Long Term Energy Yield Predictions

Section 1.2 shows photovoltaic (PV) energy can play a significant role in overcoming the energy problem and cost competitiveness is one of the main contributors to this. As PV projects require a large upfront investment and will then produce power for the remaining lifetime at relatively small costs, especially for large scale PV projects many components are taken into account to evaluate bankability of a project. One of the main parameters used to assess investments in projects relating energy production is the levelized cost of electricity (LCOE). The LCOE represents the cost to produce one kWh of electricity by a power production facility [1]. The LCOE can be compared with local energy sales prices to see whether electricity can be sold at a competitive level, thus can be used to evaluate return on investment (ROI) of a project. Such a comparison for PV systems in Germany is shown in Figure 3. It can be seen that especially large rooftop and utility scale PV are already very competitive with the non-renewable fuel sources, especially at locations with high insolation.

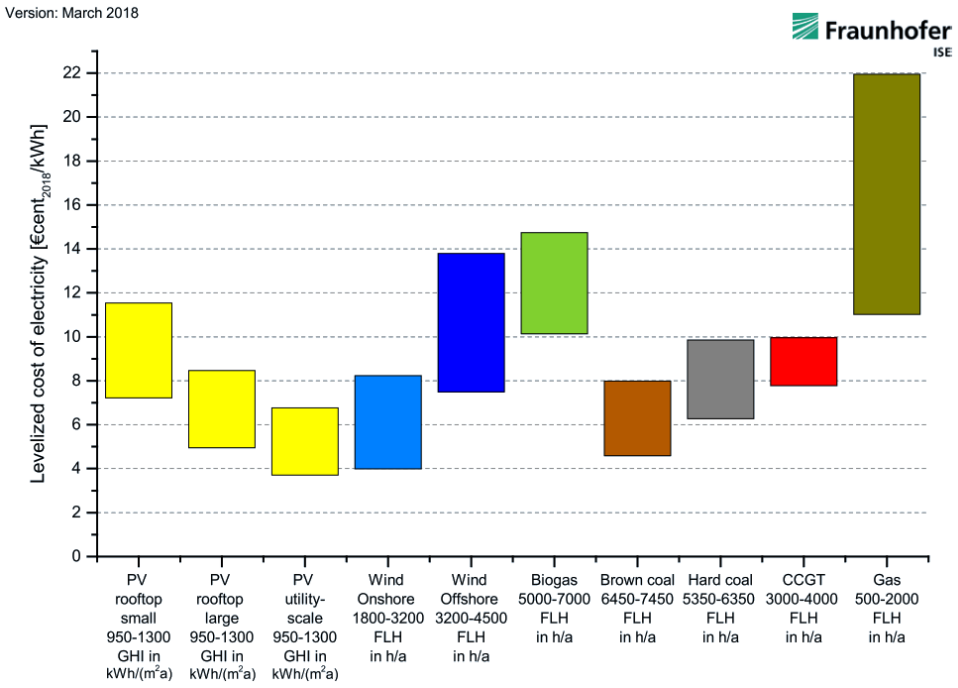

Figure 3: Levelized cost of electricity for various energy sources in Germany; Illustration by Fraunhofer ISE, Levelized Cost of Electricity - Renewable Energy Technologies, March 2018

A simplified equation for the LCOE is given in equation 1. In this equation I_t represents the investments, M_t the operational and maintenance expenditures, F_t the fuel expenditures (these are 0 for photovoltaics) and E_t the electricity yield, all in the year t. The systems lifetime is represented by n and r represents the discount rate (the weighted average cost of capital). The discount rate can be affected by various components such as time value of money and risk level of investments, which depends (among others) on the location and financing of the project [22].

$$LCOE = \frac{\sum_{t=1}^{n} \frac{I_t + M_t + F_t}{(1+r)^t}}{\sum_{t=1}^{n} \frac{E_t}{(1+r)^t}} \tag{1}$$

Some components of the LCOE are calculated based on estimates of future values. The expected electricity yield is generally estimated by the use of long term energy yield predictions. These energy yield predictions usually integrate various models, simulating local climate, the solar system configuration, technical performance of the components and much more. As the inputs and thus outcomes of these simulations generally are based on statistics and assumptions, it is important to consider the underlying uncertainty of the calculated outcome when evaluating the LCOE.

Differences between estimated energy yield and actual measured yields of utility scale photovoltaics are generally up to $\pm$ 10% [23]. These differences directly propagate into the LCOE, which is significant in the very price competitive energy market. This uncertainty in energy yield estimation however also can be seen as a risk by the investors and could affect interest rates and so have additional effects on the LCOE [24], further reducing financial competitiveness of a PV system.

Energy yield predictions can be optimized by improving the input variables for the model such as local irradiance data, technical specifications of the various components and by improved understanding of system degradation and external factors. This thesis aims to improve accuracy of these energy yield predictions by reducing the measurement uncertainty of one of the relevant input parameters for energy

yield forecasting: the temperature coefficient of the PV module.

1.4 Thesis structure: Problem statement, objectives and outline

Multiple round-robin studies have shown large lab-to-lab variations, thus uncertainties, when measuring temperature coefficients on the same set of PV modules [25] [8]. Reducing these uncertainties will improve energy yield predictions of PV systems and so reduce investment risk. Reducing investment risks leads to lower financing costs for PV system, thus supports faster roll-out of utility scale PV. A test setup and procedure was developed by Eternalsun Spire to measure these temperature coefficients more accurately, which is in need for validation and optimization.

This thesis aims to contribute to the reduction of measurement uncertainty of temperature coefficients by:

1. Identification of uncertainty drivers for temperature coefficients
2. Evaluation of the developed setup
    - Quantification of known uncertainty drivers present in the developed test setup
    - Identification and quantification of new uncertainty drivers in the developed test setup
    - Validation through uncertainty analysis and comparisons with alternative methods
3. Recommendations to further reduce measurement uncertainties of temperature coefficients in PV industry

To realize these objectives, a literature study is performed to get familiar with known uncertainty drivers for temperature coefficient measurements. Then the setup is evaluated, based on experimental results and effects of known and possibly new uncertainty drivers are studied. Based on these results, an uncertainty analysis will be performed to estimate if the developed setup can be used as a tool to reduce measurement uncertainty. Finally some theoretical and practical cases of uncertainty will be elaborated.

2 Performance of Photovoltaic Modules

2.1 Basic working principles of photovoltaic cells and modules

A solar cell is designed to convert solar irradiation into electrical energy. It does so by exploiting the so-called “photovoltaic effect”. This effect can be described as the generation of an electric potential at the junction of two materials as a result of electromagnetic radiation (such as light). Three steps can be distinguished: generation, separation and collection.

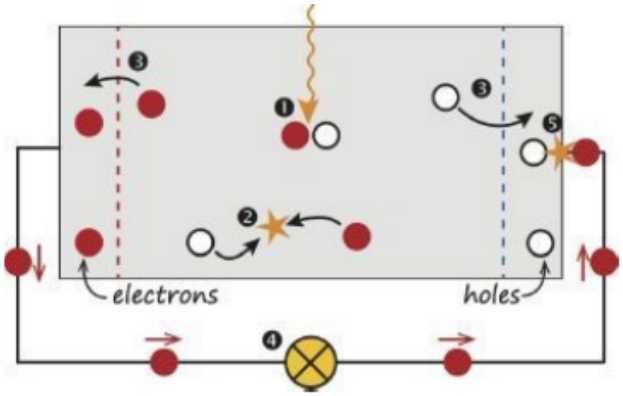

Figure 4: Basic working principles from a solar cell. 1: Generation of an electron hole pair by absorption of a photon. 2: Recombination of an electron-hole pair. 3: Separation of an electron-hole pair through a ”semipermeable membrane”, created by an electric field attracting or repelling negatively charged electrons. 4: Electrons flowing through an external load. 5: Electrons recombining with the holes at the positive terminal. *Figure: A. Smets, K. Jager, O. Isabella, R. v. Swaaij and M. Zeman, Solar energy: The physics and Engineering of Photovoltaic conversion technologies and systems. Delft: UIT Cambridge, England, 1st ed., 2016 [1]*

If a photon (an energy quantum of light) with sufficient energy is incident on a semiconductor, it can be absorbed in the material and generate an electron-hole pair (Figure 4-1). It does so by exciting electrons from the atoms from an initial energy level, in which they occupy the so called “valence band” to a higher energy level, the “conduction band”. The valence band is the outermost band around an atom at which the electrons are bound to the atom, electrons in the conduction band are free to flow through the material. To be absorbed, the photon should have more energy than the difference between the energy level in the conduction band and the valence band.

Generally, the electron-hole pair will fall back from conduction band and recombine (Figure 4-2) with a hole in the valence band after generation. The energy released in this process can be either radiative (the LED working principle), or transferred into the lattice (in the form of heat). However by using a semipermeable membrane (which allows either holes or electrons to flow out), the electron and hole can be separated (Figure 4-3).

After travelling through the electric field, the carriers will be collected at the terminals. The presence of excess electrons at one terminal and excess of holes (physically a deficit of electrons) at the other terminal will create a potential difference between the two terminals. As a result, upon connection of the terminals current will flow, which can be used to power an external circuit (Figure 4-4). After going through the external load, the electron will recombine with a hole at the positive terminal (Figure 4-5).

2.2 The electrical parameters of the PV module

The electrical behaviour of a solar cell is commonly described by the one- or two-diode model. The one-diode model is shown in Figure 5. A parallel circuit consisting of a current source, a diode and a parallel (shunt) resistor, is placed in series with a (series) resistor. This model for a single cell can be extended towards a PV module by placing a number of these circuits in series or parallel (or just the same circuit, with module equivalent parameters).

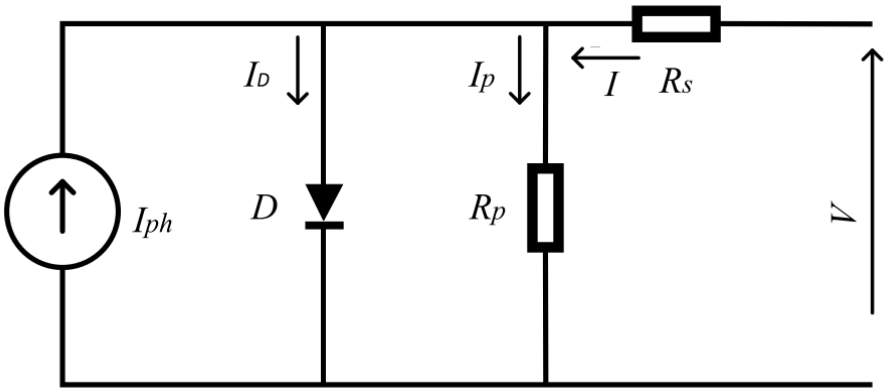

Figure 5: One-diode equivalent circuit for a photovoltaic cell. *Figure: M. Derick, C. Rani, M. Rajesh, M. E. Farrag, Y. Wang and K. Busawon, "An improved optimization technique for estimation of solar photovoltaic parameters,"Solar Energy, vol. 157, no. November,pp. 116–124, 2017 [2]*

The mathematical form of the one-diode model is given in Equation 2. Note that in this equation current densities are used instead of currents, to make the used parameters independent of cell size. In this equation, J_D represents the saturation current density of the diode, J_{ph} represents the photo generated current density, A the cell area, T the temperature, R_s the series resistance, R_p the parallel (shunt) resistance, n the diode ideality factor and k_B the Boltzmann constant.

$$J = J_D * (e^{\frac{q(V-AJR_s)}{nk_BT}} - 1) + \frac{V - AJR_s}{R_p} - J_{ph} \tag{2}$$

The one-diode model is commonly used to describe the electrical behaviour of a solar cell, however this model assumes the solar cell behaves as an ideal diode. A slightly more complex model, the two-diode model is shown in Figure 6. In the two-diode model, an additional diode is added to the circuit in parallel to include the effect of additional recombination in the p-n junction [1].

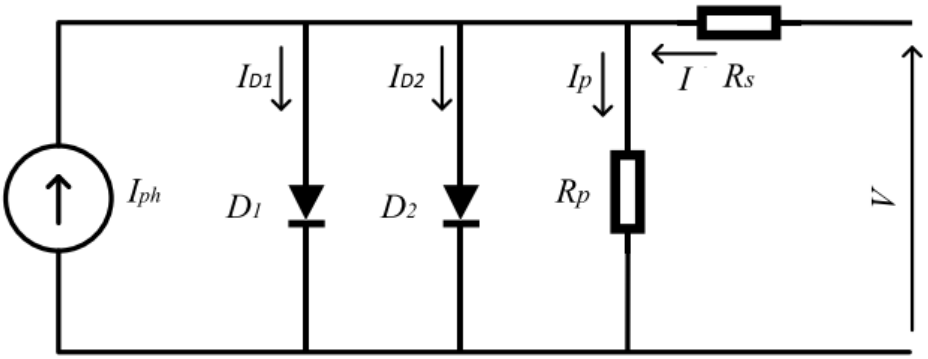

Figure 6: Two-diode equivalent circuit for a photovoltaic cell. *Figure: M. Derick, C. Rani, M. Rajesh, M. E. Farrag, Y. Wang and K. Busawon, "An improved optimization technique for estimation of solar photovoltaic parameters,"Solar Energy, vol. 157, no. November,pp. 116–124, 2017 [2]*

The mathematical expression of the two-diode model is given in Equation 3, which is very similar to the one-diode model, with the addition of the extra saturation current density J_{D2} of the diode and the diode ideality factors n_1 and n_2. Often it is simply assumed one of the diodes is ideal ($n_1 = 1$) and the other is non-ideal ($n_2 > 1$).

$$J = J_{D1} * (e^{\frac{q(V-AJR_s)}{n_1 k_B T}} - 1) + J_{D2} * (e^{\frac{q(V-AJR_s)}{n_2 k_B T}} - 1) + \frac{V - AJR_s}{R_p} - J_{ph} \tag{3}$$

Solving this equation for the typical operating range of a PV module returns the so-called JV (or IV) curve as shown in Figure 7. This curve is key in PV cell or module characterization as it contains most of the relevant electrical properties such as:

- Short-circuit current (I_{sc}): the current when the potential difference between both terminals is 0V, the maximum current the solar cell or module can deliver.
- Open circuit voltage (V_{oc}): the voltage when no external current is flowing, the maximum voltage the solar cell or module can deliver.
- Maximum power (P_{max}): the power output at the maximum power point (where the product of the voltage and current reaches a maximum)
- Voltage (V_{mp}) and Current (I_{mp}) at maximum power point
- The Fill Factor (FF), which is the ratio of the product of I_{mp} and V_{mp} to the product of I_{sc} and V_{oc}.

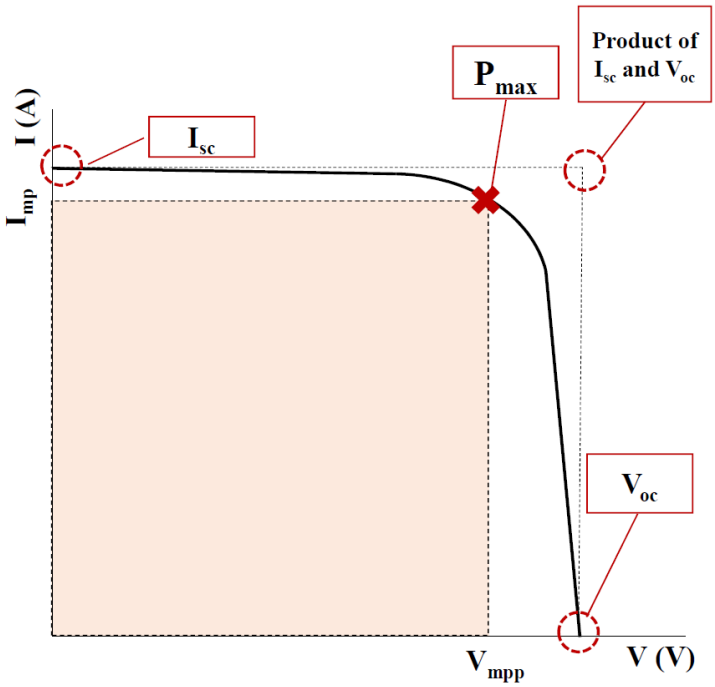

Figure 7: Typical IV curve of a PV cell or module, including the main parameters: Short-circuit current (I_{sc}), open circuit voltage (V_{oc}), maximum power (P_{max}), fill factor (FF), maximum power point voltage (V_{mp}) and maximum power point current (I_{mp})

The shape of this curve is affected by various cell properties such as the series resistance (R_s) and parallel resistance (R_p). The effects of series and parallel resistance are shown in Figure 8. Series resistance is the result of poor conduction and should be as low as possible. Some ways to do this are improving charge carrier transport through the emitter and bulk of the solar cell, or reducing the metal-semiconductor interface resistance. Parallel resistance is the resistance against leakage currents in the cell or the module and should be as high as possible. Leakage currents can be caused by shunts in the junction, enabling generated charge carriers to recombine without going through the external load.

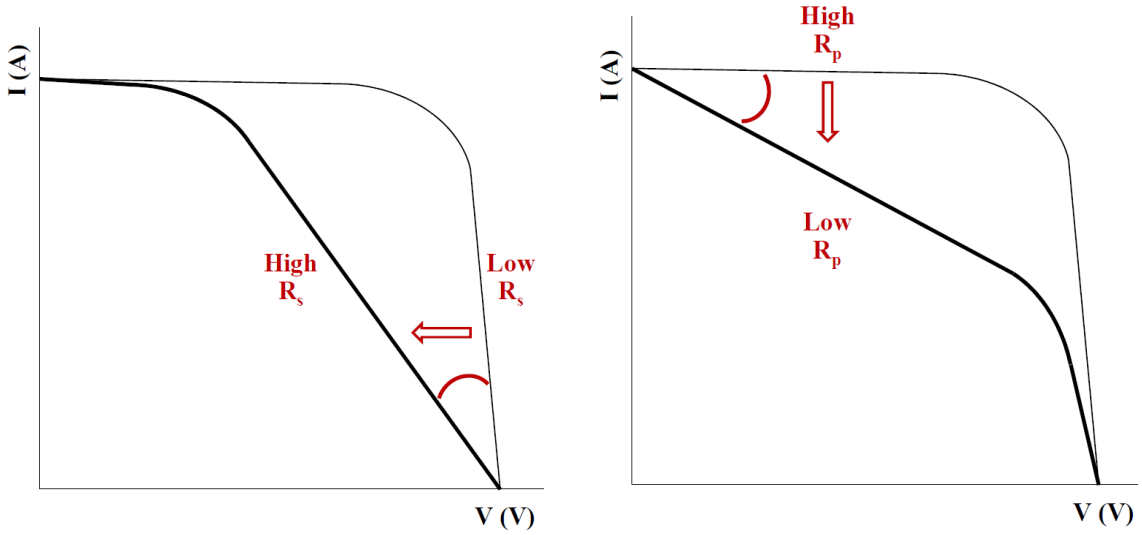

Figure 8: IV curves of the same PV module with different series and parallel resistances. Changes in series resistance mainly affect the slope near open circuit voltage, changes in parallel resistance mainly affect the slope near short-circuit current.

2.3 Characterization of PV modules

In practice, these IV curves are obtained by illuminating the cell or module, applying a variable load to the terminals and measuring the generated voltage and current using a 4-wire connection. A schematic overview is seen in Figure 9. Besides the device under test, also a reference device is measured. A reference device is a PV cell or module which is calibrated by an accredited institute, and allows for a directly traceable measurement of the incident irradiance. In the developed setup, which will be discussed in Section 3, such a reference device will be used to calibrate a monitor cell. The monitor cell is a cell integrated in the solar simulator, which is used to control the level of irradiance. While the monitor cell then acts as a reference as well, in the rest of this work, when a reference device (cell or module) is mentioned, this is always describing the external device, calibrated by an accredited institute.

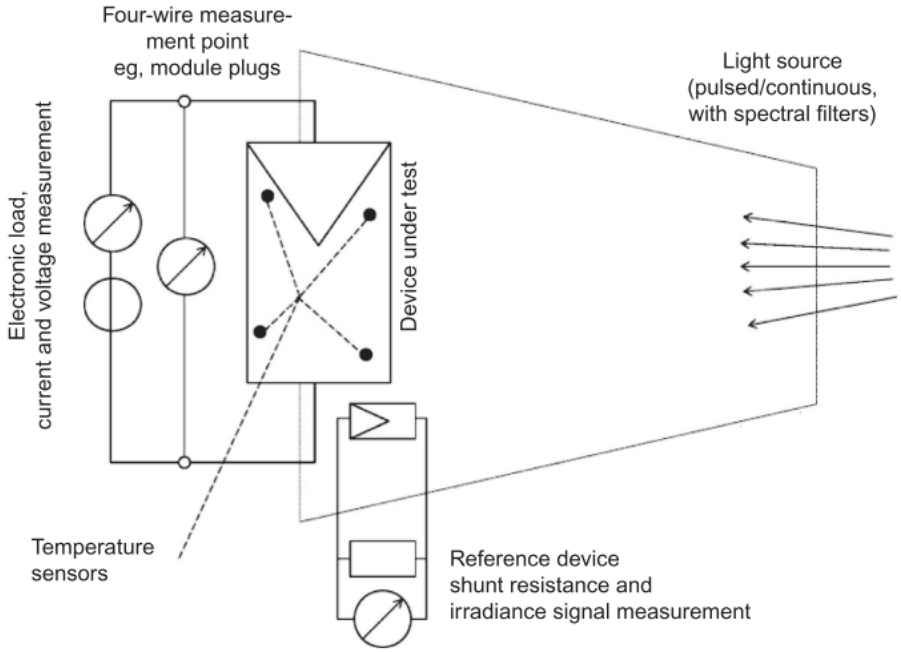

Figure 9: Schematic overview: IV measurement and illumination. *Figure adapted from: D. Dirnberger, Photovoltaic module measurement and characterization in the laboratory. Elsevier Ltd., 2017 [3]*

The measured IV curves, thus the electrical parameters, are not only affected by cell or module properties, but also by temperature, electrical connection and incident illumination. Generally speaking, higher irradiance moves the curve up, higher temperatures move the current up and the voltage down, as visible in Figure 10.

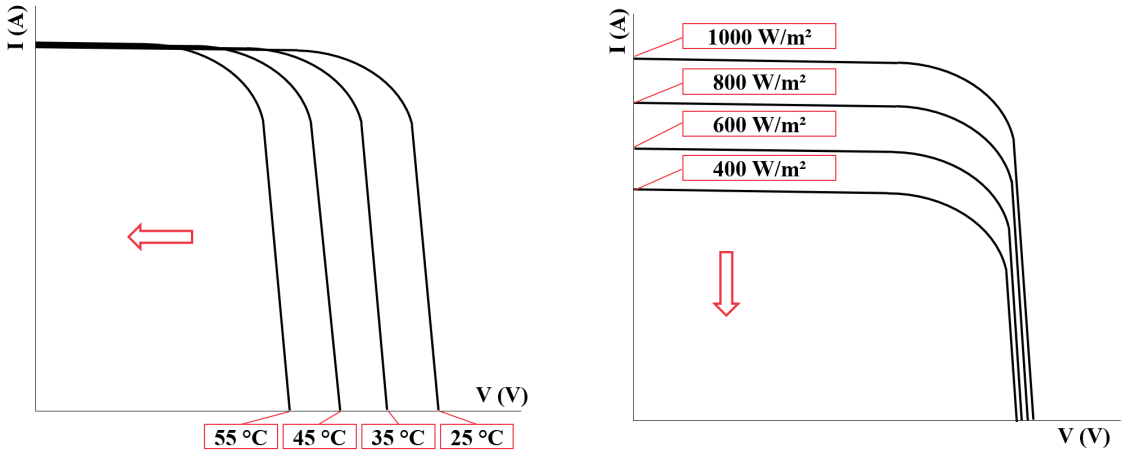

Figure 10: IV curves of the same PV module at different temperatures (left) and different levels of irradiance (right). The temperature affects mainly module voltage whereas the irradiance affects mainly module current

For direct comparability of the measurements, these external factors must be the same, or at least the differences should be taken into consideration in evaluation of the results. To perform trustworthy and reproducible measurements, various equipment has been developed and internationally agreed upon norms have been developed supporting standardization of equipment, testing conditions and operating procedures. A PV module datasheet usually provides measurement data for at least two specified conditions: standard testing conditions (STC) and nominal module operating temperature (NMOT, formerly: NOCT: nominal operating cell temperature). STC prescribes an irradiance of 1000 W/m^2 according to the AM1.5g spectrum, with a cell temperature of 25°C. NMOT conditions prescribe an irradiance of 800 W/m^2 with an air temperature of 20°C and a wind velocity $<$1 m/s.

2.3.1 Equipment for PV module characterization

To measure the illuminated IV curve of a PV cell or module in a way consistent with industry standards, one needs a variable load, current and volt meter, a source of illumination (with known spectrum), a reference device to measure the irradiance and a thermal sensor.

Figure 11: Outdoor (left) and indoor (right) characterization of PV modules. The outdoor setup shows the two-axis tracker installed at Sandia National Laboratories. *Figure: Tara Camacho Lopez, 2012, Two-Axis Tracking, accessed 01/16/2020, "https://pvpmc.sandia.gov/modeling-steps/1-weather-design-inputs/array-orientation/two-axis-tracking/"*. The indoor setup is a climate chamber integrated continuous solar simulator developed by Eternalsun Spire.

The illumination can be either real sunlight (outdoor) or artificial sunlight (from solar simulators), Figure 11 shows some examples of PV measurement setups. The outdoor method requires a two-axis tracker

to ensure the reference device and the device under test (DUT) are normal to the direct solar beam. The alternative, is to use a solar simulator to create artificial sunlight. There are roughly two types of solar simulators: steady state (continuous) and pulse-based (flash) solar simulators.

The main advantage of the outdoor method is that there is no need for a relatively costly solar simulator. The main disadvantage is that the user is dependent on the environmental conditions, such as temperature, cloudiness and on the time of day, making it impractical for high volume testing for manufacturers. Solar simulators do not face these limitations and the latest generation of solar simulators can provide very accurate, reproducible results with high module testing throughput, however come at a higher costs. Pulsed-based solar simulators are mostly used to obtain instant results of PV performance under specified irradiance and/or temperature conditions, whereas steady state simulators are used more for research purposes such as studying effects on power stability, degradation and other effects related to real world behaviour of PV.

Over the last years there has been increasing interest in PV measurements at non-standard conditions, tests aimed to predict real world behaviour more accurately. This is mainly driven by a focus on LCOE bankability for utility scale plants, including optimization of PV system design for different local climates. An example of this is the IEC61853-1 power rating, where a matrix is formed by a set of irradiance levels and temperatures at which the module parameters are determined. Compared to the P_{max} at STC and NOCT, which are currently the main performance indicators, this matrix offers more detailed information of PV module performance at a wide range of conditions. Furthermore, this matrix can be used for energy yield predictions based on reference climates and is also an interesting tool to study outdoor module behaviour [26].

Irradiance	Spectrum		Module temperature		
$W \cdot m^{-2}$		15 °C	25 °C	50 °C	75 °C
1 100	AM1,5	NA			
1 000	AM1,5				
800	AM1,5				
600	AM1,5				
400	AM1,5				NA
200	AM1,5			NA	NA
100	AM1,5			NA	NA

Figure 12: Test Matrix from IEC61853-1. This matrix of measurement results is used to create climate specific energy ratings, which offer a more intuitive performance indicator compared the the currently used P_{max} at STC. *Figure: IEC61853-1 Irradiance and temperature performance measurements and power rating, 2011 [4]*

To perform these type of measurements, various methods are used. Irradiance levels are changed by adjusting lamp intensities, applying filters or performing measurements while the light is fading at the end of a flash from a pulsed solar simulator. Temperatures are controlled using ovens, heating pads, radiative heaters, blowers, or natural heating in front of a steady state solar simulator. compared to STC measurements, the norms for non-standard conditions are less restrictive. Differences in used method however, can impact the accuracy and repeatability of the measurement. As a result there is (relative to STC measurements) more variation between measurement results performed at different laboratories using different setups and methods.

A number of different methods is in use to vary the temperature of the module, as the standards are not too strict about this. This results in various types of equipment with differences between temperature uniformities, temperature sensors and calibration and different temperature gradients from cell to backsheet. A visual representation of some of these is presented in Figure 13 as presented by M. Joshi and S. Rajeev in "Reliable module temperature measurement: considerations for indoor performance testing, 2014" [27] assuming a pulse based solar simulator. In case of steady state illumination, the temperature

gradients would look different, because of frontside and internal heating.

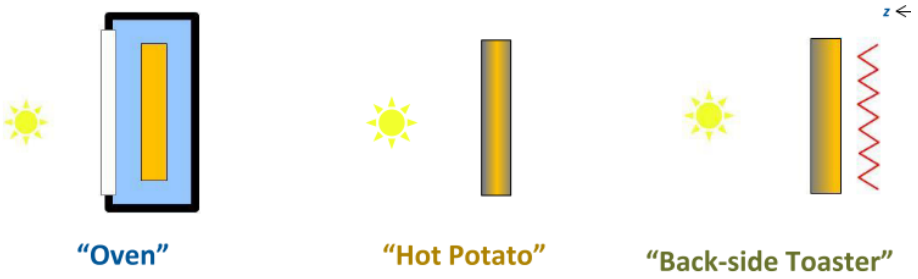

Figure 13: Three different methods used to heat a PV module, all resulting in different temperature profiles. Figure: M. Joshi and S. Rajeev in "Reliable module temperature measurement: considerations for indoor performance testing, 2014"

In the "Oven" procedure, a module is heated on all sides and kept at constant temperature for a sufficient amount of time ensuring the inside and outside to reach equilibrium. The oven has a window, which allows a solar simulator to illuminate the modules and obtain IV curves. Assuming an ideal oven, that can regulate module temperature fully uniformly, the temperature would be same at the front, inside and at the back of the module. In the "Hot Potato" procedure, a module is heated in an oven, then moved out and placed into a solar simulator and IV measurements are performed while the module cools down to ambient temperature. Because of thermal inertia the inside of the module will likely be hotter compared to the outside of the module and because of natural convection, the front and back temperature will also be different. It will thus be harder to determine the correct temperature of the cell junction. The "Back-side Toaster" procedure assumes a constant (adjustable) heat source at the back surface. A temperature gradient will exist, however the module can be kept at the same temperature longer allowing the module to thermally stabilize to steady state, improving accuracy of the results compared to the hot potato procedure.

2.3.2 Norms on PV module characterization

The most generally implemented norms for IV measurements of PV devices are developed by the International Electrotechnical Committee (IEC). The most relevant norms for this work are summarized below, in particular the norm on the determination of temperature coefficients of PV modules.

- IEC60904: Photovoltaic Devices

  This norm consists out of 10 sub parts and aims to standardize IV measurements of PV modules. The norms define (amongst others) requirements regarding illumination levels, standard testing conditions, solar spectra, calibration, traceability and testing equipment. For the illumination level, it is important that the intensity is measured with a PV reference device or pyranometer that is in some way traceable to international primary standards. These standards can either be SI units, or the World Radiometric Reference. The purpose is to ensure comparability between different labs and provide knowledge on the trustworthiness of the measured result. As the response of semiconductors is a function of the wavelength of the incident photons, not only the absolute intensity is of importance but also the spectral distribution of the incident light. A reference spectrum, AM1.5g is defined, with an integrated irradiance of 1000 W/m2, resulting from specified atmospheric and environmental conditions, after light has travelled 1.5 times the thickness of the atmosphere. In practice, the incident light is often somewhat different from the AM1.5g reference spectrum. Preferably, the reference device has a spectral response similar to the device under test (DUT). If this is not the case corrections can be applied, however in that case detailed information about the incident spectra and the spectral response of both the DUT and the reference

device should be known. Additionally, this norm sets requirements to the electrical measurements regarding measurement accuracy and defines a number of operating procedures for photovoltaic measurements. Finally a subsection of this norm states how to determine linearity of a module. PV module linearity is a requirement to perform procedures in which module performance is translated to different temperatures and/or irradiance levels.

- IEC 61853: Photovoltaic (PV) Modules and Energy Rating

  This norm consists out of 4 subparts and aims to define a standard for determination of PV energy yield for reference climates. These climate specific energy ratings should offer a better, more intuitive performance indicator compared to the maximum power output at STC. An important tool for these energy ratings is the power matrix as discussed in section 2.3.

- IEC60981: Procedures for Temperature and Irradiance Corrections To Measured I-V Characteristics

  In Figure 10 it can be seen that especially the V_{oc} and P_{max} of the PV module are a function of temperature. The relation between these module parameters and the module temperature can for most technologies be described by a linear function through by the use of the so called temperature coefficient. The temperature coefficient describes how much the module parameter changes, as a result of a known change in temperature. Amongst others, the IEC60891 norm defines procedures to determine these temperature coefficients. The most relevant temperature coefficients are the I_{sc} temperature coefficient "α", the V_{oc} temperature coefficient "β" and the P_{max} temperature coefficient "γ". Most of the c-Si based modules can be considered as linear PV devices, for such linear devices the temperature coefficients are valid over a range of $\pm 30\%$ around the irradiance at which they are measured.

  The used instrumentation should comply with the IEC60904-1 and in case a solar simulator is used, this should be at least be a BBB class simulator according to IEC60904-9. At least four temperature sensors should be applied.

  The module must be cooled or heated to the temperature of interest until the temperature is uniform within $\pm 2\%$°C. The irradiance should be set to the desired level, after which at least the I_{sc}, V_{oc} and P_{max} should be measured. The module temperature should be changed in steps of approximately 5°C, over a range of at least 30°C.

  After the measurements the parameters should be plotted as a function of temperature and a linear fit should be applied. The absolute temperature coefficient is then the slopes of these fits. In practice, often the relative temperature coefficient is provided, which is the slope divided by the value of the parameter at 25°C.

2.4 Physics of temperature coefficients

This section will briefly discuss the physics underlying the temperature coefficients, following the reasoning and equations presented in Yang Yang et al, "Understanding the uncertainties in the measurement of temperature coefficients of Si PV modules" [8]. Many of the derivations made in this work are based on the one-diode model discussed in section 2.2. The most relevant temperature coefficient for industry is the P_{max} temperature coefficient, as this is coefficient can be directly applied to predict energy yield at non-standard temperatures. The P_{max} temperature coefficient can be decomposed into three different components: the I_{sc}, V_{oc} and fill factor (FF) temperature dependencies through equation 4:

$$\frac{1}{P_{max}}\frac{dP_{max}}{dT} = \frac{1}{V_{oc}}\frac{dV_{oc}}{dT} + \frac{1}{I_{sc}}\frac{dI_{sc}}{dT} + \frac{1}{FF}\frac{dFF}{dT} \tag{4}$$

2.4.1 The Short-Circuit Current Temperature Coefficient

The Short-Circuit Current, I_{sc}, is the current when the voltage potential between the terminals is zero, i.e. when the cell or module is short-circuited. The temperature coefficient of the I_{sc}, often expressed as α, is positive with increasing temperature. For Silicon, α is usually around 0.05 %/K, thus the contribution to P_{max} temperature coefficient is relatively small. The I_{sc} temperature coefficient is a direct result of the temperature dependency of the silicon band gap, which is given in Equation 5, with X and Ψ 7.021e-4eV/K and 1108K respectively [28].

$$E_g(T) = E_g(0) - \frac{XT^2}{T + \Psi} \tag{5}$$

With increased temperature, thus increased thermal (vibration) energy of the electrons, the additional energy required to move from the valence to the conduction band reduces. As a result, photons have a higher probability to be absorbed and generate electron-hole pairs. The temperature coefficient is thus a function of the temperature dependence of the cell response (indicated by the external quantum efficiency EQE) in combination with the spectrum of the incident photons (ϕ) through Equation 6:

$$J_{sc}(T) = \int_{\lambda_0}^{\lambda_{BG}} EQE(\lambda, T)\phi(\lambda)d\lambda \tag{6}$$

2.4.2 The Open-Circuit Voltage Temperature Coefficient

Open-Circuit Voltage (V_{oc}), is the cell voltage when no external current is flowing, thus when the rate of photogeneration equals the rate of recombination in the cell. It is a function of temperature T, saturation current density J_0 (also the recombination parameter) and the short-circuit cell current J_{sc}. With magnitudes in the order of -0.3%/K for c-Si based technologies, the V_{oc} temperature coefficient, often expressed as β, is the largest contributor to the P_{max} temperature coefficient. The V_{oc} can be expressed as a function of temperature, short circuit current and saturation current density through equation 7. In this equation both J_{sc} and J_0 are a function of temperature.

$$V_{oc} = \frac{kT}{q} ln(\frac{J_{sc}}{J_0} + 1) \tag{7}$$

The temperature dependency of V_{oc} is then determined through differentiation of Equation 7 with respect to temperature. Assuming the temperature dependency of J_{sc} is relatively small and $J_{sc} \gg J_0$ differentiation of Equation 7 yields:

$$\frac{dV_{oc}}{dT} = \frac{V_{oc}}{T} - \frac{kT}{q}(\frac{1}{J_0}\frac{dJ_0}{dT}) \tag{8}$$

The temperature dependence of the V_{oc} thus depends the V_{oc} itself, the saturation current density J_0 and its temperature dependency. J_0 can be simplified to $J_0 = CT^3 \exp(-\frac{E_g}{kT})$ [29] with C a constant. Using this simplified form and the temperature dependency of the bandgap as given in Equation 5, the V_{oc} temperature coefficient can eventually be written as Equation 9, again with X and Ψ 7.021e-4eV/K and 1108K respectively. The V_{oc} coefficient is mainly determined by the difference between V_{oc} and the bandgap and the changes of the bandgap with temperature.

$$\frac{dV_{oc}}{dT} = \frac{V_{oc}}{T} - (\frac{3k}{q} + \frac{E_g(0)}{T} + \frac{XT}{(T+\Psi)^2}) \tag{9}$$

2.4.3 The Fill Factor Temperature Coefficient

The fill factor is the ratio of P_{max} to the product of V_{oc} and I_{sc}. If assumed that the cell behaves as an ideal diode (n=1), the fill factor is given by Equation 10 [30] with $v_{oc} = \frac{q}{k_B T} V_{oc}$. In this approximation it is assumed the only recombination mechanism is recombination of minority carriers in the quasi-neutral regions in the silicon bulk [1]. In practice there are most likely also other recombination mechanisms present, reducing the fill factor and the V_{oc}.

$$FF_0 = \frac{v_{oc} - ln(v_{oc} + 0.72)}{v_{oc} + 1} \tag{10}$$

The temperature coefficient of the fill factor is generally in the order of -0.15%/K. A simplified equation for the temperature dependency of the fill factor is given in Equation 11 [31], In which effects of series and parallel (shunt) resistance are ignored.

$$\frac{1}{FF}\frac{dFF}{dT} \approx (1 - 1.02FF_0)(\frac{1}{V_{oc}}\frac{dV_{oc}}{dT} - \frac{1}{T}) \tag{11}$$

3 Experimental Setup and Measurement procedures

The developed setup (Figure 14) integrates a temperature chamber with a single long pulse solar simulator. The solar simulator was developed by Eternalsun Spire, specialist in solar simulation, the temperature chamber in co-operation with Weiss Technik, specialist in environmental simulation. This combination operates according to the oven principle presented in section 2.3.1, which should theoretically give the most accurate results. The goal of this setup is to improve accuracy and reproducibility of current-voltage (IV) measurements at non-standard temperatures and so improve accuracy of temperature coefficients and IEC power rating measurements. Improving this accuracy reduces uncertainty of PV yield predictions and thus reduces financial risk, which can accelerate the large scale adaption of photovoltaics.

Figure 14: Temperature Controlled Lab Flasher (TCLF) integrating a solar simulator and a temperature chamber, developed by Eternalsun Spire to perform current-voltage measurements at non-standard testing conditions. The temperature chamber can move up, allowing a module to be placed and down to form an insulated environment for heating and cooling.

3.1 Solar Simulator

The solar simulator is a Spire 5600 Single Long Pulse flasher. The light is generated by two Xenon gas lamps, filtered to improve resemblance of the AM1.5G spectrum. The light is then guided to the test surface by the use of mirrors and diffusers, each with optimized orientation ensuring homogeneous irradiation at the test surface. A direct feedback loop between a silicon based monitor cell and the lamp control electronics ensures lamp stability throughout the whole pulse. This monitor cell is calibrated at the beginning of (a series of) tests using a calibrated reference cell or module. As a result of this control loop, the lamp properties and the system electronics, a stable light pulse up to 270ms can be provided, which is advantageous for measuring high efficiency, capacitive, photovoltaic technologies (such as c-Si/a-Si Heterojunctions) [32]. Besides the lamp and the optical control, there is a system dedicated to measuring IV curves. The module is connected through a 4-wire connection, allowing current and voltage to be measured simultaneously and minimizing effects of cable resistance. To measure the IV curve a variable load is applied, which is varied in such a way that more measurement data is collected around the maximum power point of the PV module (which is for most applications the most important

part of the curve, as well as the part of the curve with highest rate of change). From the measured IV curve, other values such as the P_{max}, Fill Factor, R_s, R_{sh} and efficiency are determined.

3.1.1 Irradiance and optical properties of the solar simulator

The irradiance uniformity of the setup is visualized in Figure 15. For accurate IV measurements, the irradiance incident on a module should be as uniform as possible. Generally cells are connected in series, thus module current will be limited by the cell generating the lowest current. If a part of the module receives less than average irradiance, this will limit the performance of the rest of the module as well, resulting in an incorrect measurement. Areas with relatively high irradiance are referred to as ”hot” areas, areas with relatively low irradiance are referred to as ”cold” areas. The left uniformity map is based on a 96-point measurement used for IEC60904-9 classification. This is created by averaging each four by four row and column pairs from the high-resolution uniformity measurement as shown on the right. The distribution with the hot and cold pattern visible in the high-resolution uniformity map is typical for the Spire 5600 simulator and is a result of the orientation of the two Xenon lamps, the diffusers and the mirrors. IEC60904-9 defines spatial uniformity based on the maximum and minimum irradiance measured in the test surface, Equation 12: The simulator can be classified in class A (the highest standard) according to IEC60904-9 Ed.2 (non-uniformity $<2\%$) and A+ according to the upcoming IEC60904-9 Ed.3 (non-uniformity $<1\%$) as only 64 measurement points are required for the uniformity determination (so the 96 point uniformity is sufficiently detailed).

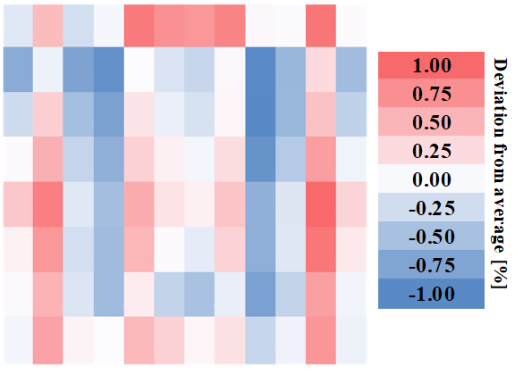

Figure 15: Simulator irradiance uniformity for IEC60904-9 classification (left) Note: high resolution non-uniformity measurement removed for public manuscript

$$non - uniformity\,[\%] = \frac{irradiance_{max} - irradiance_{min}}{irradiance_{max} + irradiance_{min}} \times 100\% \tag{12}$$

The spectrum of the solar simulator is plotted in Figure 16. If the reference device (used for calibration) and the device under test (DUT) have a different spectral response, a spectral mismatch error will affect the result of the measurement (this will be further elaborated in Section 5.3.3). This error is proportional to the difference between the AM1.5G (reference) spectrum, thus the closer the resemblance of the solar simulator spectrum and the AM1.5G reference spectrum, the lower the impact of a spectral mismatch between the reference device and the device under test. Even though spectral filtering is used, there are still some peaks visible which are typical for Xenon lamps. The spectrum is measured at 96 points on the simulator (ensuring the spectrum is similar everywhere on the test area) using a Pulse Analysis Spectroradiometer System (PASS) [33] as provided and calibrated by the US National Renewable Energy Laboratory (NREL).

Figure 16: Measured Spectrum of the solar simulator next to the AM1.5G reference spectrum (removed for public manuscript)

In the IEC spectral classification, the distribution of energy between specified photon wavelengths is compared for the simulator and the reference AM1.5 spectrum. This is visualized in Figure 17. A classification (C/B/A,A+) is assigned based on the deviation of the energy in the specific bin. The spectrum of the simulator is classified as A+ according to both current and proposed IEC60904-9 norm, which means a maximum deviation in energy from the AM1.5 spectrum of $\pm$ 12.5% in the worst case.

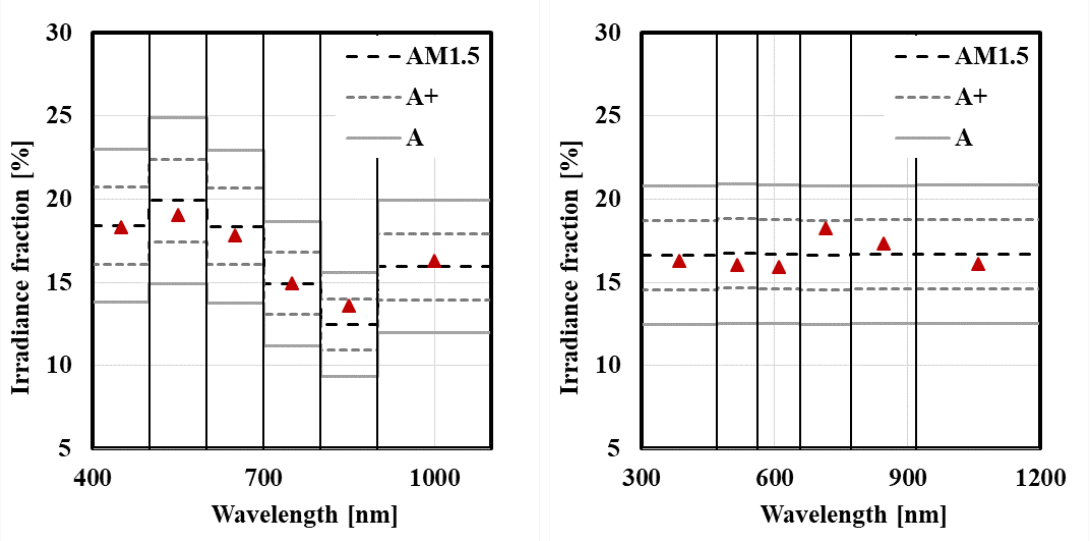

Figure 17: Measured fraction of irradiance (indicated in red) in wavelength bins as specified per IEC60904-9 Ed.2 (left) and proposed IEC60904-9 Ed.3 (right). Note that the spectrum according to IEC60904-9 Ed.2 is defined from 400nm to 1100nm, whereas IEC60904-9 Ed.3 extends the first and the last bin to 300nm and 1200nm and has a different distribution of bins.

The third important property is the temporal stability of the pulse. Two components are considered: the short term instability (STI) and the long term instability (LTI). The short term instability describes the maximum change in intensity between the acquisition of a current-voltage-irradiance data point. However in most modern simulators, as well as in the applied setup, these are obtained simultaneously in which case the STI is considered class A+ per IEC60904-9 Ed.3. The long term instability is defined in Equation 13 and basically represents the maximum relative change of the light intensity during acquisition of the IV curve. A 0.05% LTI is achieved over 200ms of pulse, which is easily surpassing class A per IEC 60904-9 Ed.2, or A+ per IEC60904-9 Ed.3.

$$Temporal\,instability\,(\%) = \frac{irradiance_{max} - irradiance_{min}}{irradiance_{max} + irradiance_{min}} \times 100\% \tag{13}$$

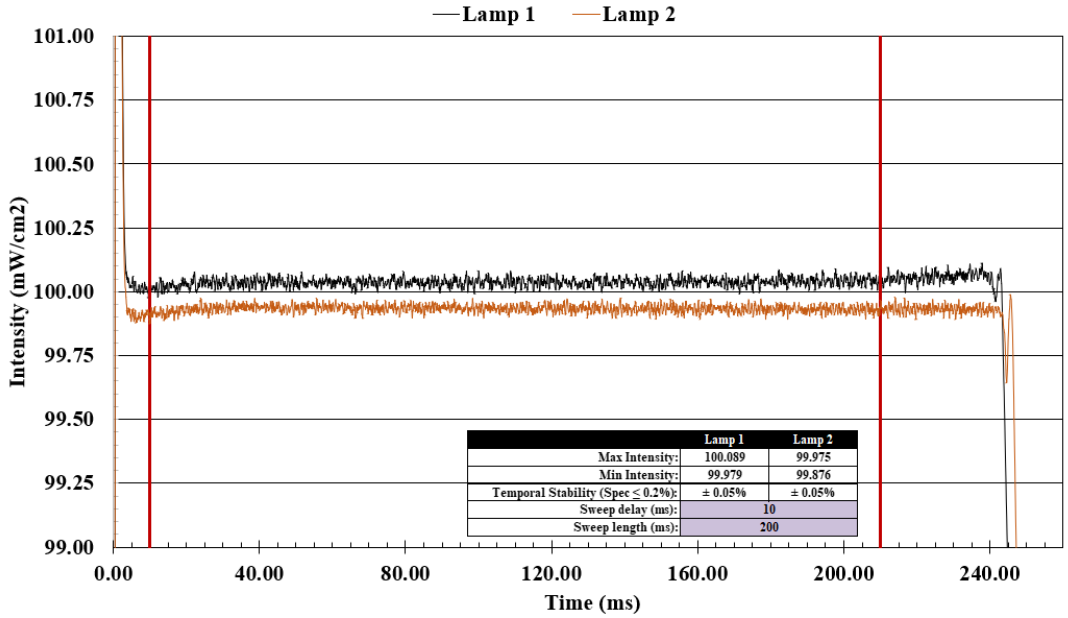

Figure 18: Long term instability $\pm 0.5\%$ of the light pulse measured over 200ms. By addition of extra capacitors (providing energy to the lamps), the length of the pulse can be further extended up to 270ms

3.1.2 Electrical system and software of the solar simulator

The measurement circuit is based on a Measurement Computing DT9834 DAQ. The module voltage is reduced by a voltage divider, selected through a switching relay depending on the voltage range. This voltage is digitized by the DAQ and forwarded to the software. A somewhat similar process is applied for the current, however this is measured over a shunt. The shunt resistor is also selected through a switching relay, depending on the range of module current. Additionally, this circuit contains a MOSFET, which is slowly opened up or closed depending on sweep direction. By doing this, the PV module is subjected to a variable load and the full IV curve can be measured. The circuits with aforementioned voltage dividers, shunt resistors and switching relays are developed and calibrated in-house, using devices traceable to international standards. Alternatively, external calibration can be done if ISO17025 accreditation is needed. For each current and voltage range, two known currents and voltages are applied, which are measured with calibrated equipment before the input of the system and compared to the displayed values in the system software. Based on the deviations, gains and offsets can then be applied. The software is being developed by Eternalsun Spire. It is used to control the simulator, collect the data from the DAQ and process this data into full IV curves. From these (approximately 3500 point) IV curves, the PV module parameters are extracted and stored in a database.

3.2 Temperature chamber

The temperature chamber is developed by Weiss Technik in cooperation with Eternalsun Spire. It is placed on top of the solar simulator and can be moved up and down through electromechanical actuators. When the chamber is raised the module can be placed and wiring can be connected. When the chamber is closed, a thermally insulated space is formed in the chamber, closed off by the simulator glass. Temperature can be controlled between 10°C and 85°C by forced convective heating/cooling. The module is placed on 13.5mm thick spacers, or conveyors with similar height, allowing air to flow past the front and the back of the module. The air circulation is controlled by 3 fans and air temperature is controlled by heating coils and a heat exchanger in a feedback loop with a PT100 temperature sensor.

Module temperature data is collected by 9 T-type thermocouples, attached on the rear surface of the module with (3M-425) aluminium tape (Figure 19). This data is read out by a Pico technology TC08-USB datalogger. Temperature non-uniformity measured on the rear surface of the module, defined as $(T_{max} - T_{min})/2$, is $\pm$1°C at an air temperature of 85°C, down to $\pm$0.2 °C for air temperatures between 25°C and 50°C.

3.3 Measurement procedure

This section describes the used procedure to determine PV module temperature coefficients, including calibration of the lamp intensity. After the detailed step by step description, an overview (assuming a calibrated setup) is given in Figure 20.

1. The temperature chamber is opened/moved up and the simulator is calibrated to the desired intensity using a reference module (or alternatively to a World Photovoltaic Scale (WPVS) reference cell) calibrated by an accredited laboratory. The reference module is placed on the test area at room temperature, flashed and measured. Based on the measured I_{sc} and the target I_{sc} provided by the reference laboratory, the intensity of the lamps will be increased or decreased and another IV measurement is performed. This process is repeated until the measured I_{sc} is within set tolerance of the target value. Simultaneously, a monitor cell inside the solar simulator measures the irradiance from the lamps. The monitor cell I_{sc} read out during the last flash of calibration is stored and will function as a target after the reference module is removed. These monitor cells are in a direct control loop with the lamps and will correct the lamp intensity from pulse to pulse as well as during the pulse.

2. The calibration module is removed and the device under test (DUT) is placed. If a calibrated WPVS cell is used instead of a calibration module, it is possible to keep the cell in the test surface (next to the DUT) to provide a traceable irradiance measurement.

3. 9 Sensors are attached to the rear surface of the module using 3M aluminum (thermally conductive) tape, in a 3x3 formation as shown in Figure 19 and the module cables are connected to the test leads of the solar simulator. The readings of these sensors will eventually be averaged to determine the surface temperature of the backsheet of the module.

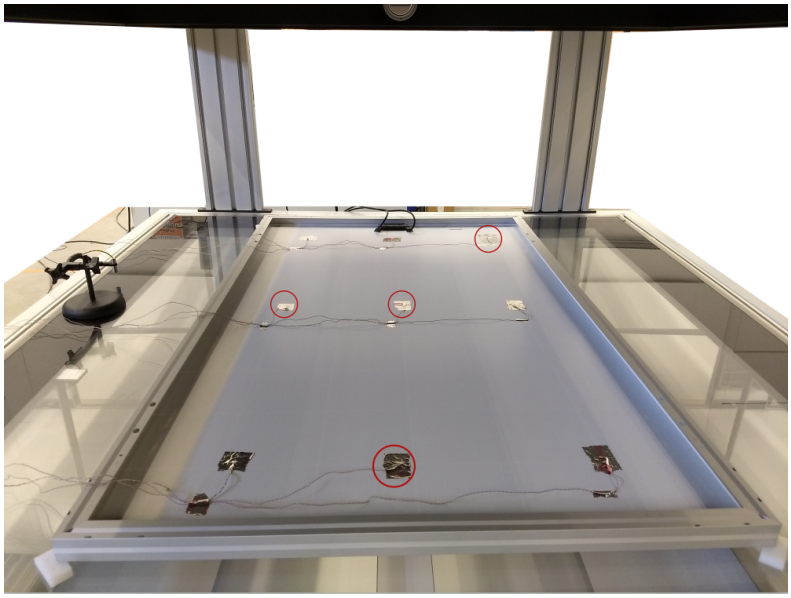

Figure 19: A 60-cell c-Si PV module placed in the (opened) temperature coefficient lab flasher. 9 T-type thermocouples are attached to the rear surface of the module in 3x3 formation. The four circles indicate the positions of temperature sensors required per IEC60891.

4. IV measurements are started with a constant interval and a temperature recipe (with setpoints for the air temperature) is run. Simultaneously, logging of the module temperature is started. The temperature in the chamber is first ramped up to the maximum temperature of interest, causing the DUT temperature to rise as well. Once the temperature setpoint is reached, the temperature is kept at this setpoint until the cell temperature is stable as well, which is monitored by the V_{oc} variation (directly affected by cell temperature) between a number of successive flashes. Currently V_{oc} is considered stable when 3 consecutive IV measurements return V_{oc} values within the machine repeatability specification for V_{oc}. Once V_{oc} stability is observed, 3 additional IV measurements are performed, these will be used to extract the module parameters. After these 3 additional IV measurements, the air temperature will go to the next setpoint in the temperature recipe and the process will be repeated until the temperature recipe is finished. These temperature recipes generally include the temperatures from the power matrix as defined in IEC61853-1 (Section 2.3).

5. In data processing, the temperature data measured by the temperature sensors on the rear surface of the module is averaged. This averaged module temperature is coupled to the IV measurements based on timestamps. Generally the temperature is logged at a much higher frequency than IV measurements are obtained, resulting in negligible delay between temperature and IV measurements. The IV parameters of interest are determined from the IV curves and used to determine temperature coefficients. The parameters from the 3 IV measurements are averaged for the reporting, but individual parameters, temperature sensor readings and full IV curve data are stored as well. The temperature coefficient measurements in this work are all performed at an irradiance level of $1000 W/m^2$, it is also possible to measure the IV curve at multiple irradiance levels (and multiple temperature setpoints) to fill the IEC61853-1 matrix.

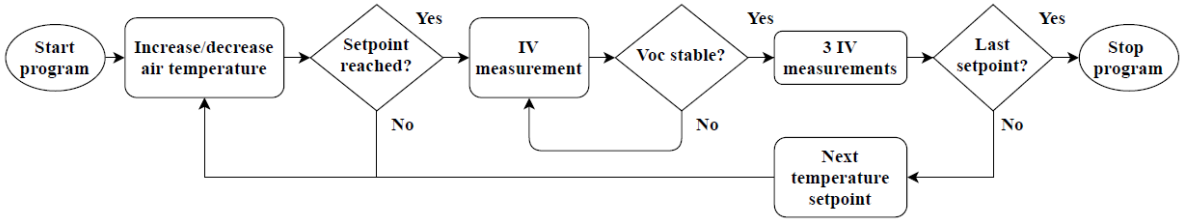

Figure 20: Flowchart of the developed test procedure assuming a calibrated setup and connected device under test

4 Temperature Coefficients of Silicon based PV

In this section the results are presented of the performed temperature coefficient measurements on a set of Aluminum Back Surface Field (Al-BSF), Passivated Emitter Rear Cell (PERC) and Silicon Heterojunction (SHJ) photovoltaic modules. Each subsection briefly explains the typical cell structure of the considered technologies, after which the measurement results are presented. These results will be used for the uncertainty analyses presented in the next section. A summary of the tested PV modules is shown in table 1. Each module has its own identification (ID) based on [Technology] – [Structure (mono/poly)] – [Datasheet P_{max}] – [Module brand and type]. A suffix indicates cases where multiple PV modules of the same brand and type are tested. If the modules are non-commercial and/or no datasheet P_{max} is known, this is indicated by empty square brackets.

Table 1: Summary of the tested PV modules and their datasheet STC parameters

ID	Technology	P_{MAX} [W]	V_{OC} [V]	I_{SC} [A]	# of cells	Comments
BSF-p-280-A_1	Aluminum Back Surface Field	280	38.2	9.52	60	
BSF-p-280-A_2	Aluminum Back Surface Field	280	38.2	9.52	60	
BSF-p-275-A	Aluminum Back Surface Field	275	38	9.45	60	
BSF-p-260-B	Aluminum Back Surface Field	260	37.8	9.01	60	
BSF-p-275-B	Aluminum Back Surface Field	275	38.7	9.25	60	
PE-m-290-C	PERC	300	39.7	9.73	60	
PE-m-295-D	PERC	295	39.48	9.7	60	
SHJ-m-285-E	Silicon Heterojunction	285	63.5	5.91	88	
SHJ-m-[]-F_1	Silicon Heterojunction	[N/A]	[N/A]	[N/A]	72	Pre-production
SHJ-m-[]-F_2	Silicon Heterojunction	[N/A]	[N/A]	[N/A]	72	Pre-production
SHJ-m-[]-G	Silicon Heterojunction	[N/A]	[N/A]	[N/A]	60	Non-commercial

4.1 Temperature coefficients of Al-BSF Modules

Aluminum Back Surface Field (Al-BSF) cell technology has been the largest cell technology for many years, and a large part of the currently installed modules is based on this technology. While currently being surpassed by higher efficiency technologies such as PERC, Al-BSF based modules are still very useful for evaluation of the test procedure and setup, as there is plenty of knowledge and reference data available at Eternalsun Spire and in literature.

4.1.1 Al-BSF Technology

The structure of an Al-BSF cell (Figure 21) is relatively simple. A pn-junction is formed between positively doped silicon, the bulk, and a thin layer of negatively doped silicon, the emitter. Electrodes are connected on the front and rearside of the cell, collecting and transporting charge carriers through the module and through an external circuit. An anti reflective coating on top of the emitter reduces reflection, resulting in improved photon absorption, thus an increase in photon generated current. A highly doped Aluminum p^+ layer is applied between the rear electrode and the p-type bulk. In this p^+ layer, more (negatively charged) acceptor ions are present, creating a more negatively charged region between the bulk and the rear electrode. As a result, negatively charged electrons are repelled from the rear electrode, reducing recombination at the bulk-electrode interface. This effect is called field effect

passivation.

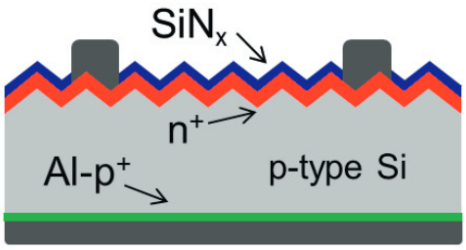

Figure 21: Standard Al-BSF Industrial Solar Cell. Image adapted from: Krügener, J; Harder, N, Weak light performance of PERC, PERT and standard industrial solar cells, Energy Procedia 2013 [5]

4.1.2 Al-BSF module measurements

Table 2: Datasheet parameters of the tested Al-BSF modules

ID	Datasheet STC parameters					Datasheet temperature coefficients [%/°C]		
	P_{max} [W]	V_{oc} [V]	I_{sc} [A]	V_{mp} [V]	I_{mp} [A]	P_{max} (γ)	V_{oc} (β)	I_{sc} (α)
BSF-p-280-A_1	280	38.2	9.52	31.3	8.95	-0.41	-0.31	0.05
BSF-p-280-A_2	280	38.2	9.52	31.3	8.95	-0.41	-0.31	0.05
BSF-p-275-A	275	38	9.45	31	8.88	-0.41	-0.31	0.05
BSF-p-260-B	260	37.8	9.01	30.7	8.5	-0.4	-0.27	0.024
BSF-p-275-B	275	38.7	9.25	31.5	8.74	-0.4	-0.27	0.024

Five commercial Al-BSF modules (Table 2) are tested with the main purpose to validate the performance of the setup. All the modules are 60 cell, p-type poly modules, 3 modules are from brand A, 2 modules are from brand B. For the two modules from brand B, additional measurement results from an external institute (Fraunhofer ISE) are available for comparison. It has to be noted that these results are obtained over a year ago and in the meanwhile the modules have been used as reference modules and/or to check performance of newly built systems. The handling of these modules can have caused small damages such as micro-cracks, thus results might not be fully representative.

Table 3 shows a comparison of the measured relative temperature coefficients with the manufacturer specifications, Figure 22 shows the P_{max}, V_{oc}, I_{sc} and Fill Factors parameters plotted at different temperatures.

Table 3: Measured and manufacturer specified temperature coefficients of the Al-BSF modules

ID	P_{max} Temperature Coefficient			V_{oc} Temperature Coefficient			I_{sc} Temperature Coefficient		
	Datasheet [%/°C]	Measured [%/°C]	Deviation [%]	Datasheet [%/°C]	Measured [%/°C]	Deviation [%]	Datasheet [%/°C]	Measured [%/°C]	Deviation [%]
BSF-p-280-A_1	-0.410	-0.405	1.21	-0.310	-0.307	0.91	0.050	0.0407	18.61
BSF-p-280-A_2	-0.410	-0.394	3.96	-0.310	-0.300	3.22	0.050	0.0386	22.80
BSF-p-275-A	-0.410	-0.411	0.25	-0.310	-0.309	0.20	0.050	0.0383	23.35
BSF-p-260-B	-0.400	-0.419	4.69	-0.270	-0.310	14.74	0.024	0.0369	53.70
BSF-p-275-B	-0.400	-0.411	2.80	-0.270	-0.308	14.20	0.024	0.0421	75.62

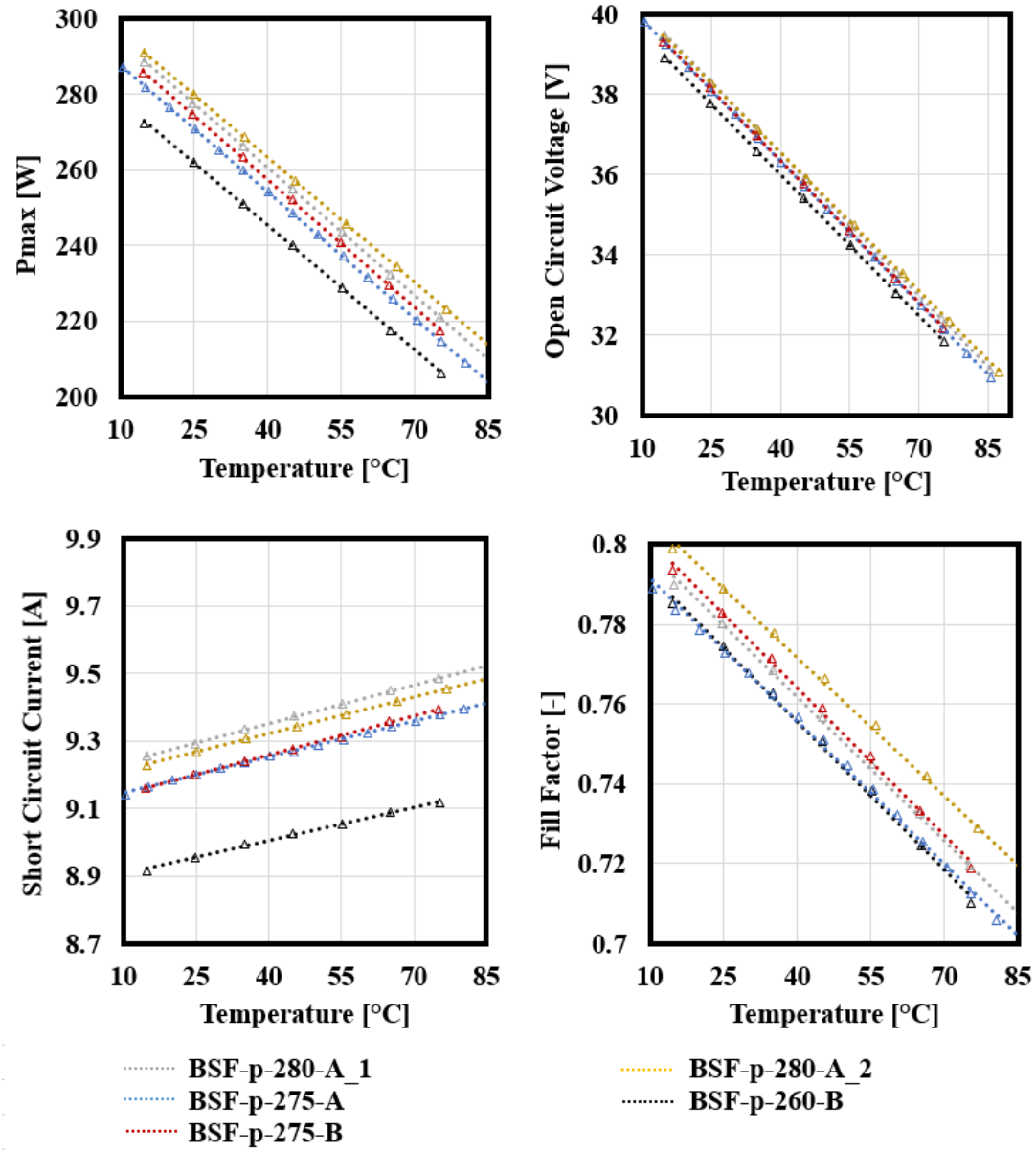

Figure 22: Maximum Power Point, Open Circuit Voltage, Short Circuit Current and Fill Factor of the five Al-BSF modules measured at various temperatures between 10 and 85 degrees

From these results, some initial observations can be made:

- Similar slopes, thus temperature coefficients, are measured for all modules
- Linear fitting seems to be applicable to all the parameters, with the coefficient of determination $R^2 \gg 0.99$
- P_{max} temperature coefficients are consistent within 5% of the manufacturer specifications, V_{oc} temperature coefficients within 5% for the modules of brand A, a larger deviation of 15% is observed for the modules of brand B, I_{sc} temperature coefficients show the largest variation: up to 25% and 75% for the brand A and brand B respectively.
- Different temperature coefficients are measured for modules of the same types and brands

As the modules are based on the same cell technology, similarity of the temperature coefficients is expected. It is noteworthy however that modules of the same brand and type can still show some variation. The V_{oc} temperature coefficient reported on the datasheet of brand B seems to be too high (too favourable) compared to the measurements. As the modules of brand A are based on the same cell technology with similar efficiencies, it could be caused by an incorrect determination of the V_{oc} parameter by manufacturer B. The largest (relative) deviations are observed in the I_{sc} coefficient, which could be a result of a different spectrum used for the test, in combination with the (temperature dependent) spectral response of the module which is not corrected for due to lack of available data. Overall, the measured P_{max} coefficients are consistent with expectations for both modules, the modules of brand B however show relatively large deviations for both V_{oc} and I_{sc} coefficients.

Additionally, results from the two modules of brand B are compared to results obtained by Fraunhofer ISE in Table 4. At Fraunhofer ISE, a similar method is used for temperature control, in combination with another highly accurate solar simulator. This likely explains the small differences observed in V_{oc} and P_{max}. Larger differences, of same magnitude, are observed in the I_{sc} temperature coefficient, which are, again, possibly caused by differences in solar spectra of both solar simulators.

Table 4: Results measured with the developed temperature coefficient setup compared to results by Fraunhofer ISE

ID	P_{max} Temperature Coefficient [%/°C]			V_{oc} Temperature Coefficient [%/°C]			I_{sc} Temperature Coefficient [%/°C]		
	TCLF	Fra -ISE	Deviation [%]	TCLF	Fra -ISE	Deviation [%]	TCLF	Fra -ISE	Deviation [%]
BSF-p-260-B	-0.419	-0.413	1.43	-0.310	-0.310	0	0.0369	0.047	27.4
BSF-p-275-B	-0.408	-0.405	0.74	-0.306	-0.309	0.98	0.041	0.051	24.39

While the temperature dependency of the series resistance appears to be similar for all the modules, larger deviations are observed in the temperature dependencies of the parallel (shunt) resistances, Figure 23. Even between modules of the same type (red/black and blue/gray/yellow), large differences are observed. The parallel and series resistance are approximated by the inverse of the slope of the IV curve at I_{sc} and V_{oc} respectively. These slopes are obtained through linear fits to the datapoints around I_{sc} and V_{oc}. As can be seen in the Figure 23, especially the parallel resistance does not show a clear trend with temperature for all the modules. This could be a result from the fitting method, since the parallel resistance is determined by the slope of the IV curve at I_{sc} is very small in absolute form. As a result, small fluctuations in the measurement data can have large effects on the parallel resistance.

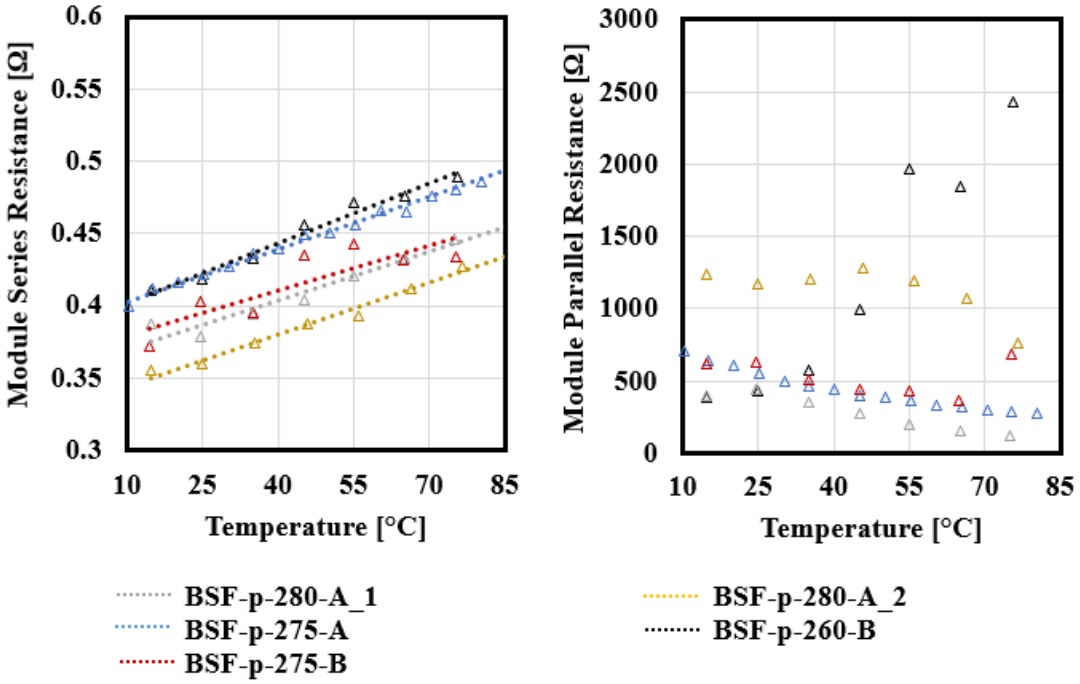

Figure 23: Series and parallel resistance of the five Al-BSF modules measured at various temperatures between 10 and 85 degrees. No trendline is plotted for the parallel resistance to improve readability.

4.2 Temperature coefficients of PERC Modules

PERC is currently the dominating technology in the PV market. Compared to classic Al-BSF cell technology, higher efficiencies (>20% in manufacturing) are obtained as a result of improved surface and interface passivation. Several implementations are clustered under the PERC name [34], of which the most common variations are the PERL (Passivated Emitter Rear Locally doped) and the PERT (Passivated Emitter Rear Totally diffused).

4.2.1 PERC Technology

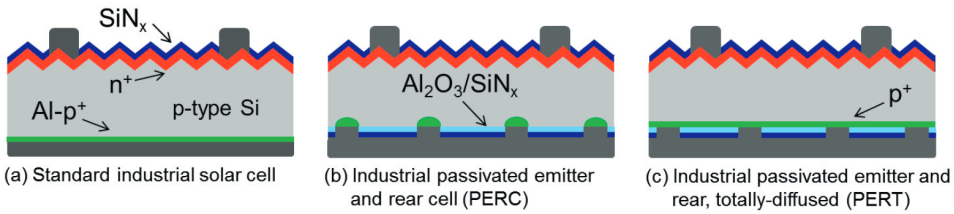

Figure 24: Left: Standard Al-BSF Industrial Solar Cell. Middle: Industrial Passivated Emitter Rear Locally doped (PERL) cell. Right: Industrial Passivated Emitter Rear Totally diffused (PERT) cell. Image adapted from: Krügener, J; Harder, N, Weak light performance of PERC, PERT and standard industrial solar cells, Energy Procedia 2013 [5]

Common to both the PERL and the PERT concepts, Figure 24, is the passivated emitter. A passivating layer, often SiO_2/SiN_x is deposited on top of the emitter passivating dangling bonds. As a result, the density of trap states at the surface is decreased, reducing surface recombination. Besides the emitter, also the rear side of the cells is passivated, improving the response to low wavelength photons. Small openings in the rear passivation layer allow contact between the rear electrode and the bulk silicon. These contact areas are passivated similar to the Al-BSF cell reducing interface recombination. Whereas PERL

cells have this passivation layer only locally at the metal – semiconductor interface, PERT cells have this passivation layer across the whole interface region of the bulk silicon, the electrodes and the passivated areas between these contacts.

4.2.2 PERC Measurements

Table 5: Datasheet parameters of tested PERC modules

ID	Datasheet STC parameters					Datasheet temperature coefficients [%/°C]		
	P_{max} [W]	V_{oc} [V]	I_{sc} [A]	V_{mp} [V]	I_{mp} [A]	P_{max} (γ)	V_{oc} (β)	I_{sc} (α)
PE-m-290-C	290	39.7	9.73	31.2	9.29	-0.45	-0.35	0.07
PE-m-295-D	295	39.48	9.7	32.19	9.17	-0.39	-0.28	0.04

Two commercial PERC modules are tested, the datasheet values are shown in table 5 and the results are presented in Table 6 and Figure 25

Table 6: Measured and manufacturer specified temperature coefficients of the PERC modules

ID	P_{max} Temperature Coefficient			V_{oc} Temperature Coefficient			I_{sc} Temperature Coefficient		
	Datasheet [%/°C]	Measured [%/°C]	Deviation [%]	Datasheet [%/°C]	Measured [%/°C]	Deviation [%]	Datasheet [%/°C]	Measured [%/°C]	Deviation [%]
PE-m-290-C	-0.45	-0.386	14.18	-0.35	-0.284	18.93	0.07	0.031	55.43
PE-m-295-D	-0.39	-0.381	2.34	-0.28	-0.276	1.31	0.04	0.033	16.84

Both PERC modules have a similar efficiency, and also similar behaviour with temperature. Whereas PE-m-290-C (plotted black) has a somewhat lower V_{oc} and I_{sc}, the Fill Factor is significantly better compared to PE-m-295-D. In comparison to the manufacturer datasheet, PE-m-290-C shows large deviations in all the temperature coefficients, while the measurements of PE-m-295-D are almost consistent with manufacturer specifications. Compared to the Al-BSF modules, the I_{sc} temperature coefficient is lower, less beneficial, but the V_{oc} and P_{max} temperature coefficients are higher, more beneficial. Figure 26 shows PE-m-290-C has a better series and parallel resistance with respect to PE-m-295-D, likely causing the better fill factor of PE-m-290-C. Similar to Al-BSF modules a clear relation is observed between temperatures, parallel and series resistance, however again much less linear compared to the other IV parameters.

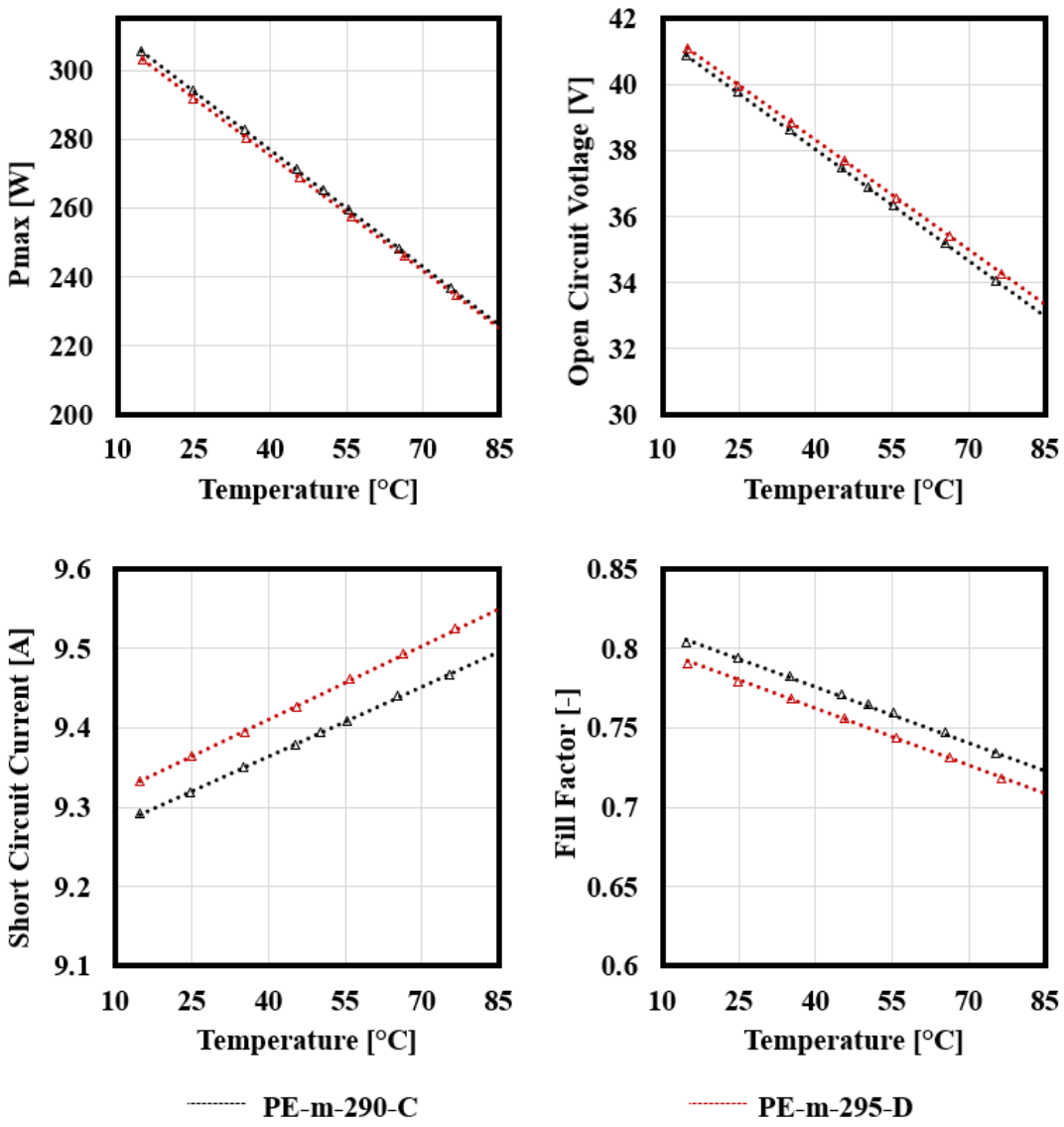

Figure 25: Maximum Power Point, Open Circuit Voltage, Short Circuit Current and Fill Factor of the two PERC modules measured at various temperatures between 10 and 85 degrees

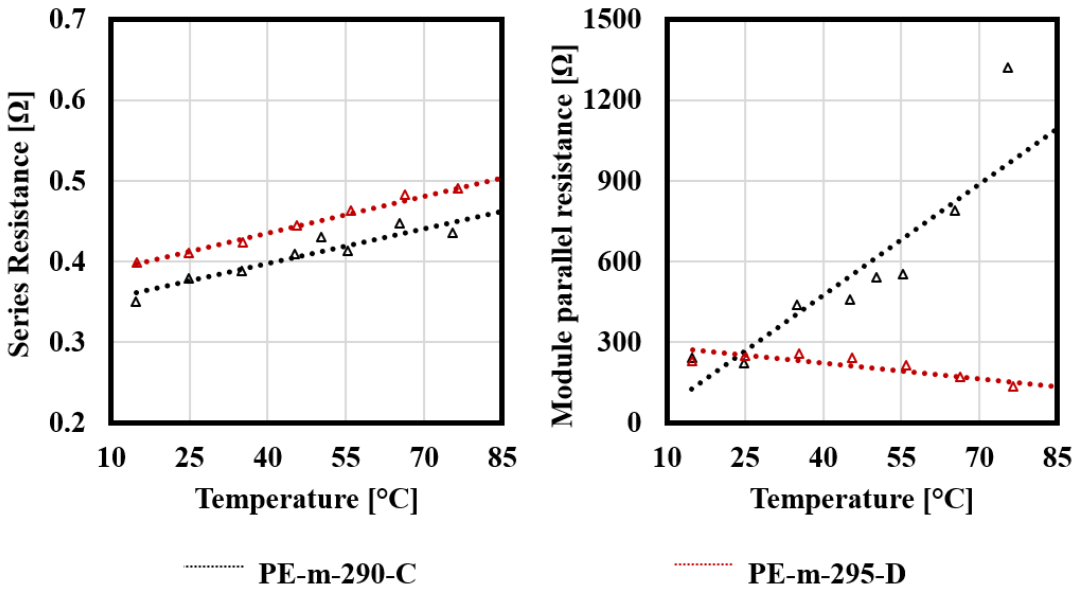

Figure 26: Series and parallel resistance of the two PERC modules measured at various temperatures between 10°C and 85°C

4.3 Temperature coefficients of Silicon Heterojunction Modules

The marketshare of Silicon Heterojunction (SHJ) cell technology is expected to increase from approximately 3% to 15% in the next 8 years [35]. SHJ cells are build around high quality n-type crystalline silicon wafers, with the surface passivated by thin layers of amorphous silicon. This passivation enables very high efficiency c-Si cells [36]. Real world degradation as a result of light and elevated temperatures (LETID) and potential induced degradation (PID), known to occur in many PERC modules, is not present in SHJ modules as a result of the n-type wafers used.

4.3.1 Silicon Heterojunction Technology

Figure 27 shows the structure of an SHJ cell. An intrinsic layer of hydrogenated a-Si is added to reduce the interface defect density between the c-Si and the doped a-Si. As the conductive properties of the a-Si are relatively poor, a transparent conductive oxide (TCO) layer (often Indium Tin Oxide, ITO) is added improving carrier transport towards the electrodes on the front- and rearside of the cell. A tradeoff here is that the TCO is usually not fully transparent, increasing parasitic absorption thus reducing the cell current.

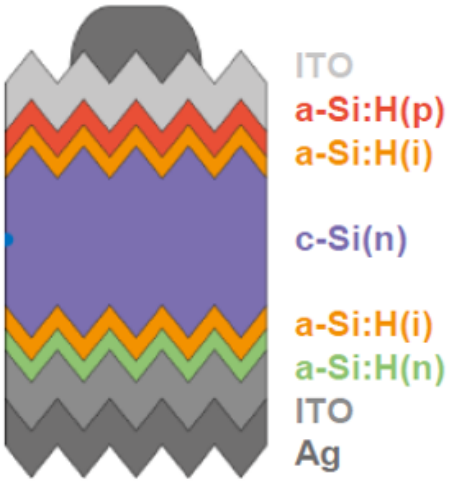

Figure 27: Structure of a Silicon Hetero Junction Solar cell: Illustration by Haschke J., Temperature dependence and infrared response of silicon based solar cells: simulation and experiment, QEERI seminar, 2016

4.3.2 Silicon Heterojunction Measurements

One commercial and three non-commercial modules are tested. Only the commercial module comes including STC parameters specified by the manufacturer, the parameters of the other modules are unknown. The results are presented in Table 8 and Figure 28.

Table 7: Datasheet parameters of the SHJ modules

ID	Datasheet STC parameters					Datasheet temperature coefficients [%/°C]		
	P_{max} [W]	V_{oc} [V]	I_{sc} [A]	V_{mp} [V]	I_{mp} [A]	P_{max} (γ)	V_{oc} (β)	I_{sc} (α)
SHJ-m-285-E	285	63.5	5.91	52	5.49	-0.29	-0.250	0.030
SHJ-m-[]-F_1	N/A	N/A	N/A	N/A	N/A	N/A	N/A	N/A
SHJ-m-[]-F_2	N/A	N/A	N/A	N/A	N/A	N/A	N/A	N/A
SHJ-m-[]-G	N/A	N/A	N/A	N/A	N/A	N/A	N/A	N/A

Table 8: Measured and manufacturer specified temperature coefficients of the SHJ modules

ID	P_{max} Temperature Coefficient			V_{oc} Temperature Coefficient [%/°C]			I_{sc} Temperature Coefficient [%/°C]		
	Datasheet [%/°C]	Measured [%/°C]	Deviation [%]	Datasheet [%/°C]	Measured [%/°C]	Deviation [%]	Datasheet [%/°C]	Measured [%/°C]	Deviation [%]
SHJ-m-285-E	-0.29	-0.27	1.21	-0.250	-0.241	0.91	0.030	0.030	0
SHJ-m-[]-F_1	N/A	-0.306	N/A	N/A	-0.245	N/A	N/A	0.029	N/A
SHJ-m-[]-F_2	N/A	-0.316	N/A	N/A	-0.249	N/A	N/A	0.026	N/A
SHJ-m-[]-G	N/A	-0.269	N/A	N/A	-0.254	N/A	N/A	0.025	N/A

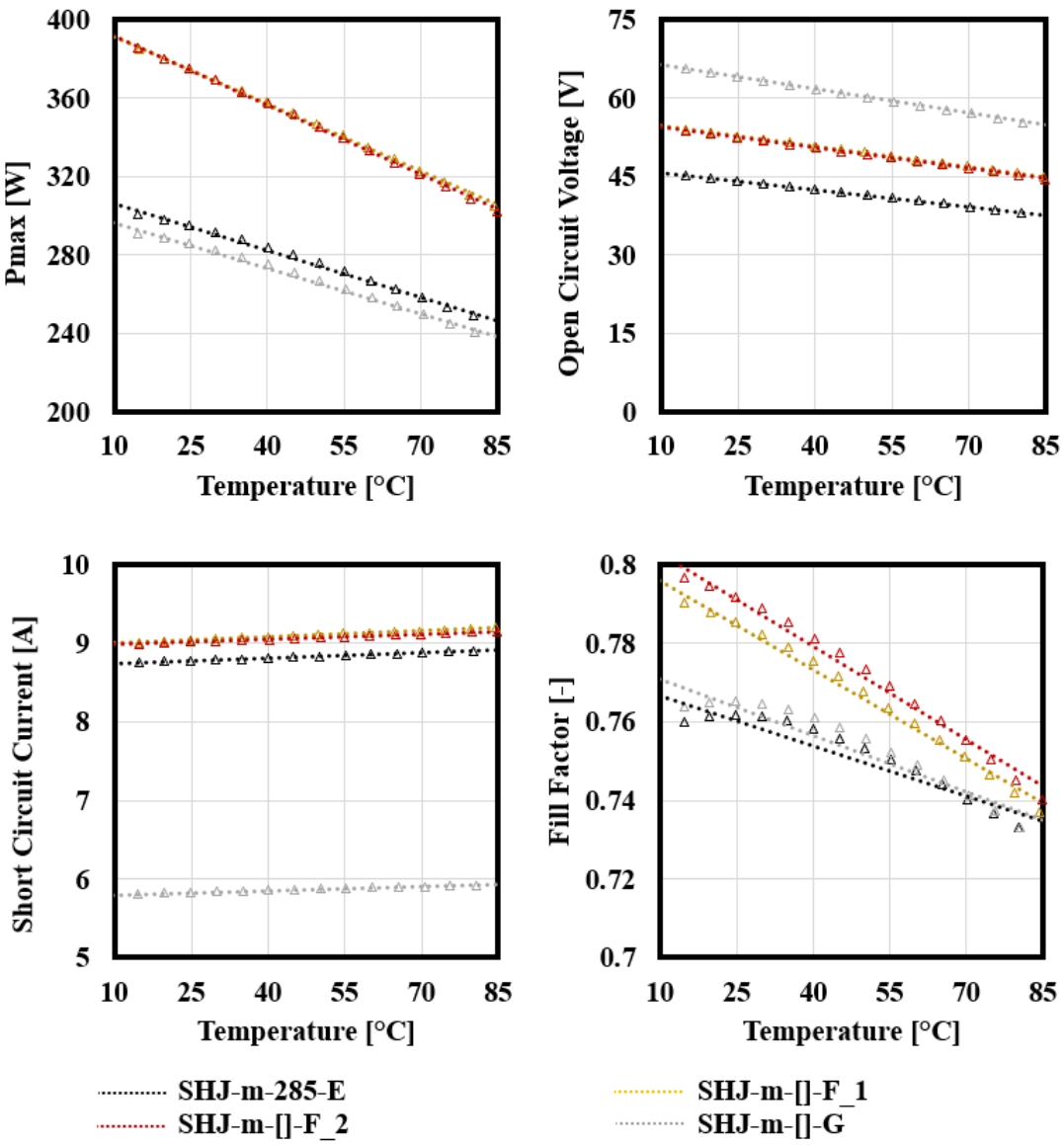

Figure 28: Maximum Power Point, Open Circuit Voltage, Short Circuit Current and Fill Factor of the four Silicon Hetero Junction modules measured at various temperatures between 10 and 85 degrees

The SHJ modules SHJ-m-285-E and SHJ-m-[]-G give some interesting results. The fill factors show an almost parabolic shape when varying the temperature between 10°C and 85°C between measurements at 10 degrees and 55 degrees. The V_{oc} and I_{sc} do not show this non-linearity, but a small proportion of this effect is propagated into the P_{max} temperature coefficient. The P_{max} temperature coefficient is therefore a function of the temperature at which it is determined and a linear fit seems less appropriate. This effect is previously observed on a cell level [37] and is likely a result of charge carrier transport mechanisms. At lower temperatures, the carrier transport is limited by thermionic emission across a local potential barrier at the interface of the amorphous and crystalline silicon. This barrier decreases non-linearly with increasing temperatures [38], improving carrier transport and reducing the contribution of this barrier to the fill factor. At higher temperatures the effect of this barrier becomes less significant and the fill factor changes more linear with temperature. This effect is only very slightly visible in fill factor of the other two SHJ modules, where it is almost negligible for the P_{max} temperature coefficient.

IEC 60904-10 defines requirements for PV modules to be considered linear (temperature coefficients can only be applied for linear modules). With respect to temperature only one requirement is defined: ”For

the curve of open-circuit voltage and short-circuit current versus temperature, the normalized standard deviation of the slope should be below 0.1" (IEC60904-10)

Where the standard deviation of the slope is calculated through Equation 14, after which it is normalized by the slope of the linear regression line.

$$\sigma_s = \sqrt{\frac{\sum(\Delta Y_i)^2}{(n-2)\sum(\Delta X_i)^2}} \tag{14}$$

As the non-linearity is a result of the changing fill factor, it comes to no surprise the modules can be considered linear according to this definition, with the highest normalized standard deviation $\frac{\sigma_s}{slope} = 0.02$ for I_{sc}. Even when also considering the σ_s of the Fill Factor and P_{max}, the module can be considered linear, which is a result of the linear behaviour at higher temperatures.

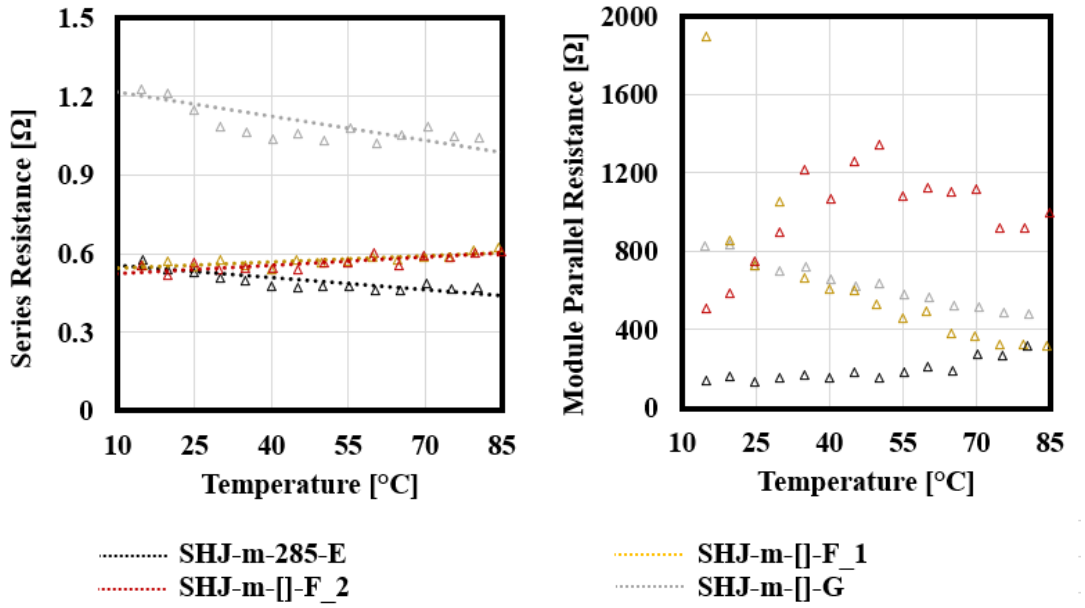

Figure 29: Series and parallel resistance of the four SHJ modules measured at various temperatures between 10°C and 85°C

Figure 29 shows the series and the parallel resistance plotted against temperatures. Different from all other measured modules, SHJ-m-285-E and SHJ-m-[]-G both show a negative temperature dependency for the series resistance, which is likely caused by the decreasing interface resistance. The temperature dependency of the parallel resistance of the two modules of brand and type F shows large variations even though both modules are of the same brand, type and technology and production batch.

4.4 Temperature coefficients of c-Si modules and open circuit voltage

A clear relation is observed between the cell V_{oc} at STC and the V_{oc} and P_{max} temperature coefficients, as can be seen in Figure 30. Better passivation not only leads to higher STC efficiency, but also to better performance at increased temperatures.

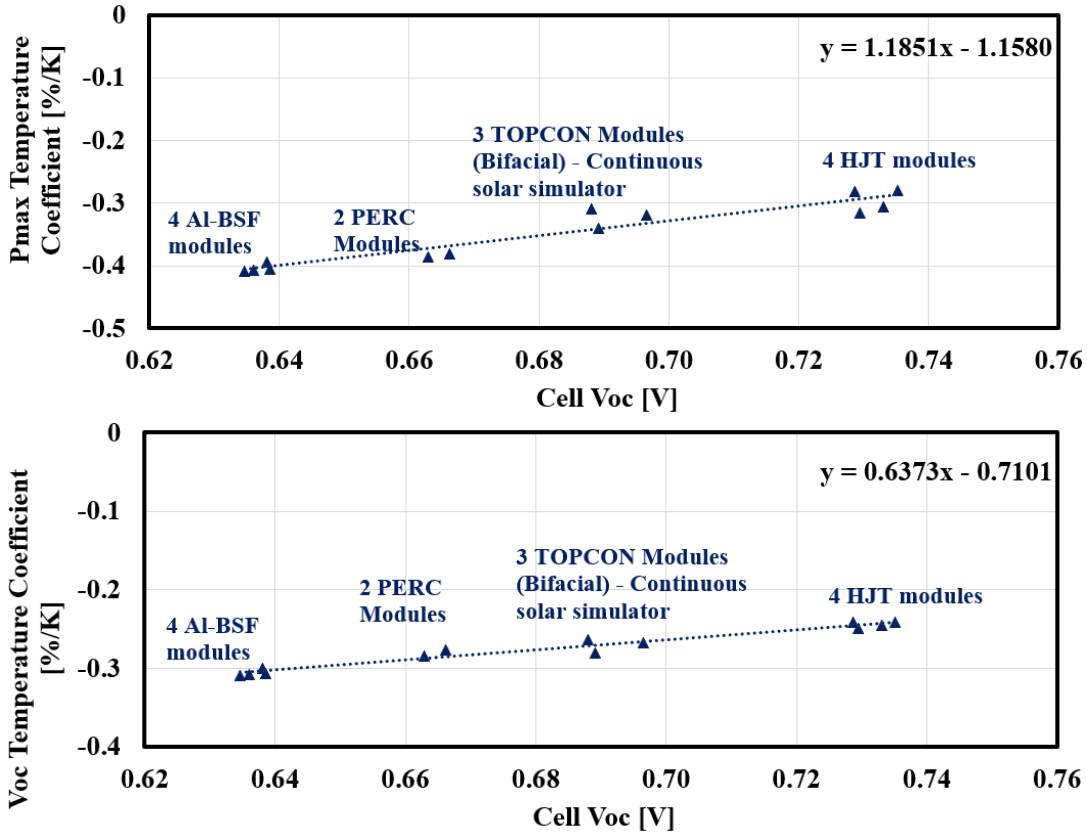

Figure 30: Relative P_{max} and V_{oc} temperature coefficients of the measured modules plotted against cell V_{oc} at STC. A clear positive relation is visible, which can be used to estimate the temperature coefficients based on the cell V_{oc}

As the relative temperature coefficient is obtained by dividing the absolute temperature coefficient by the STC value, a higher STC value will directly lead to a better relative temperature coefficient, even with the same absolute temperature coefficient. Figure 31 shows the absolute temperature coefficient of the cells plotted against the cell V_{oc} at STC, from which can be concluded that the observed relation is not only the result from the increase in STC performance. Note that the absolute temperature coefficient on the vertical axis in Figure 31 is the temperature coefficient per cell, which allows for comparability between modules that have a different numbers of cells.

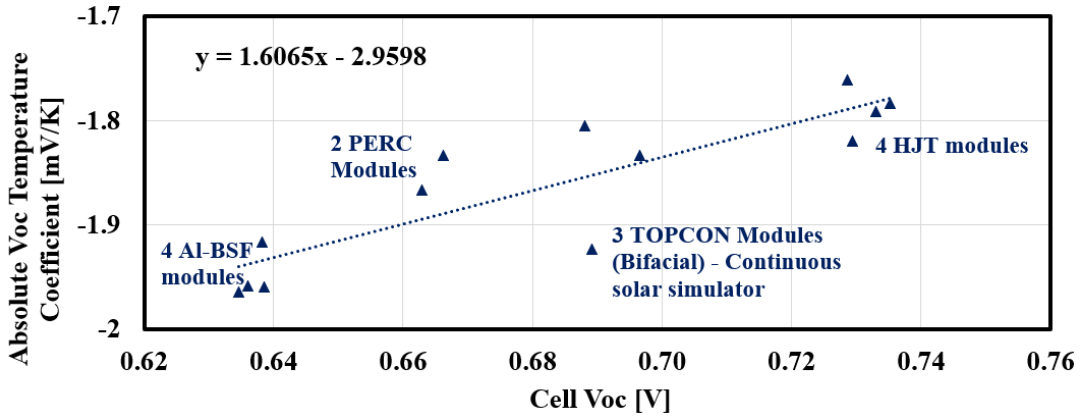

Figure 31: Absolute V_{oc} temperature coefficients against cell V_{oc}, which shows that the relation between cell V_{oc} and temperature is also visible in the absolute temperature coefficients. Note: the absolute temperature coefficient on the vertical axis is the temperature coefficient per cell, which enables comparability between modules that have a different numbers of cells.

This relation is observed before [39] and an interesting application based on this relation is recently presented by Y. Hishikawa et al. (AIST) [6]. Here the temperature coefficients are both measured as well as calculated based on the relation between cell V_{oc} and temperature coefficient. These results are then used to translate IV curves of c-Si modules over a range of 40°C. Differences between measured and calculated results are below $\pm 1.5\%$ for the V_{oc}, I_{sc} parameters as well as for the P_{max} parameters. As this procedure is currently under consideration by the IEC, some data obtained in this thesis will be presented to provide additional reference material.

The theoretical relation between the temperature coefficient (TC) and the cell voltage, derived from the single diode model by Hishikawa, is given in equation 15. This equation is found to be a good approximation for a voltage range of the (cell's) IV curve from approximately 0.5V to 0.7V. In this equation, v_1 and v_2 are the cell voltages at the two considered temperatures T_1, T_2, with a current level offset equal to ΔI_{sc}. This is visualized in Figure 32, note that ΔI_{sc} is already defined as ΔI. Additionally, n is the diode ideality factor, E_g the bandgap and q the Boltzmann's constant.

$$TC_{cell} = \frac{v_2 - v_1}{T_2 - T_1} = \frac{1}{T_1}(v_1 - \frac{nE_g}{q}) \tag{15}$$

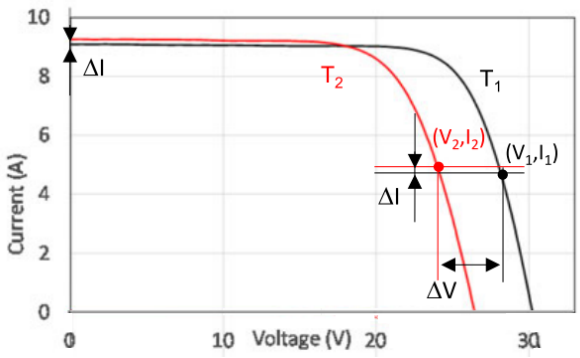

Figure 32: IV curves of a c-Si PV module measured at 1000 W/m^2, at 25°C (T1) and 65°C (T2). Additionally, the datapoints V_1, V_2, I_1, I_2 required to calculate the TC using equation 15 are marked. Figure adapted from: Y. Hishikawa et al. (AIST) [6]

In Figure 33, equation 15 is plotted for a voltage range of 0.5V to 0.75V. Here it is assumed that $\frac{nE_g}{q} = 1.232$V, which represents a diode ideality factor of 1.1 and a c-Si bandgap of 1.12eV. In the left of Figure 33, the results of Hishikawa et al. are presented and the results obtained at Eternalsun Spire are shown in the right. For the results from Eternalsun Spire, 3 modules (1 AL-BSF, 1 SHJ, 1 PERC) are randomly selected. Based on IV measurements at 25°C and 65°C, TC_{cell} is calculated and multiplied with T_1 (approximately 25°C, 293.15K). This product is then plotted against the cell voltage v_1 for 4 different voltage points of the IV curve. Note that Hishikawa et al. consider many more datapoints, however 4 datapoints already allows basic comparability.

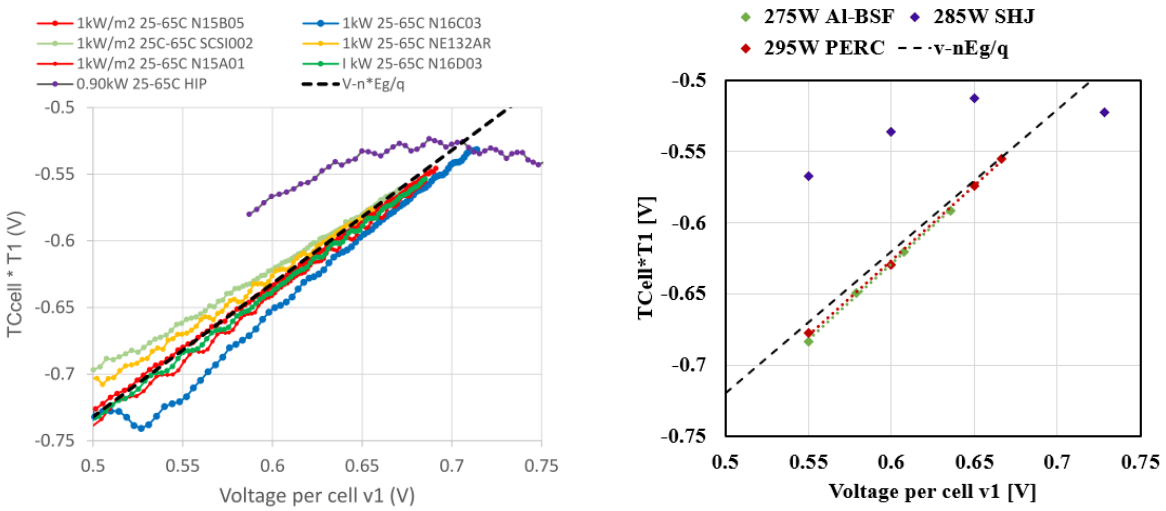

Figure 33: The product of T_1 and TC_{cell} plotted against v_1 for several modules based on experimental IV curves measured at 25°C and 65°C. The dashed black line represents the calculated result, which is based on the theoretical TC from equation 15 with $\frac{nE_g}{q} = 1.232$. Left: results obtained by Hishikawa et al.; Right the results by Eternalsun Spire for 3 randomly selected modules based on different c-Si technologies.

Both the results from Hishikawa et al. and the results obtained at Eternalsun Spire show that, except for the SHJ modules, the measured temperature coefficient can be approximated by the temperature coefficient calculated from equation 15. Both the SHJ module measured by Hishikawa et al. (plotted in purple, marked as "HIP" in the legend) and the SHJ module measured at Eternalsun Spire show clear inconsistency with the other modules and equation 15. This can be caused by the thermionic effect briefly discussed in section 4.3.2, which affects the change of the IV curve with temperature. As a result, the suggested procedure for IV curve corrections developed by Y. Hishikawa et al., is (in current form) probably not applicable for some SHJ modules.

5 Uncertainty in Photovoltaic Measurements

Imagine, in your living room at home, some of the laminate flooring is worn out and needs to be replaced. Luckily you kept some spare pieces which only need to be cut to the desired length, as shown in Figure 34. With the ruler and saw you have available, each spare can be cut to 30 cm with a potential maximum random error of ± 5 mm. The combined length of the replacement pieces could thus be anywhere between 59 cm and 61 cm. However, even though the length of each spare has equal probability to be anywhere between 29.5 cm and 30.5 cm, the combined length is less likely to be 59 cm or 61 cm as it is unlikely both (independent) errors are working to full extend in the same direction. What is the length you would aim for to be sure the spare pieces will fit in?

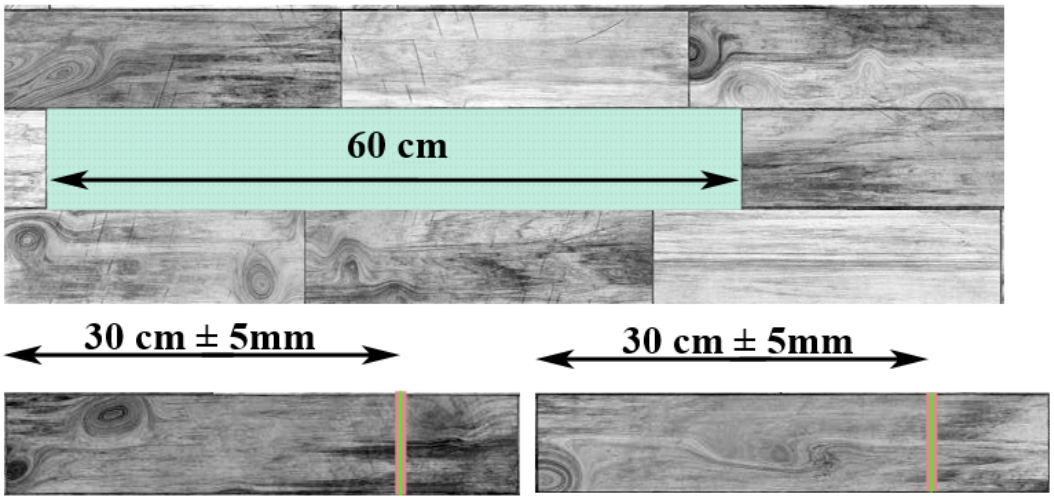

Figure 34: Visualisation of the laminate problem. Figure adapted from: www.galerie21.nl

This section will give insight into the effects of such uncertainties, now applied in the measurements of PV modules. The effect of measurement uncertainties on the PV energy yield is discussed in section 5.1, the underlying statistics and literature examples of uncertainty analyses on PV measurements in section 5.2, after which the uncertainty of the developed setup will be analysed in section 5.3. In section 5.4 a brief sensitivity analysis will be performed and finally section 5.5 will elaborate on some uncertainty components occurring in practice, especially relevant for PV industry.

5.1 The impact of Measurement Uncertainty on Energy Yield Predictions

Investors and purchasers, thus also manufacturers of PV modules, have high interest in accurate knowledge on the uncertainty of photovoltaic (PV) power measurements. Uncertainty in the nameplate capacity for example, introduces uncertainty in the energy yield prediction, which propagates into financial uncertainty. Manufacturers should therefore account for any uncertainty in the measurement when determining the P_{max} of a PV module. A majority of the manufacturers provides a positive power guarantee on the P_{max} of a module (e.g. 300 W, -0% / +3%): the module produces at least 300W and up to 3% extra at standard testing conditions (STC). As the P_{max} is currently one of the main pricing parameters, having to account for measurement uncertainty negatively affects the module sales price. An approximation based on common industry measurement uncertainty levels shows the effect on the revenue loss in Figure 35. This figure shows manufacturer revenue loss against P_{max} measurement uncertainty for a 300W module, assuming a module price of €0.30/W and 3W or 5W binning of the modules, typical for current industry [40], compared to the effect without binning. These losses are significant in the

competitive PV market, driving the industry to reduce measurement uncertainty through improvement of PV testing methods.

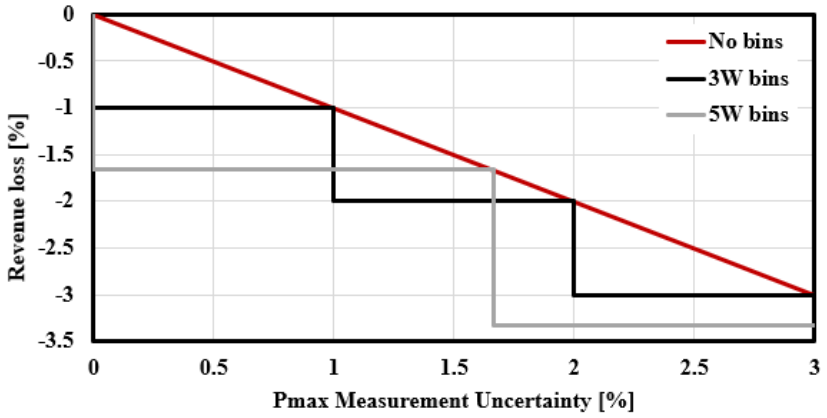

Figure 35: Approximation of the effect of measurement uncertainty onto the price of a photovoltaic module, assuming a 300W module and a module price of €0.30/Wp

Over the last years there has been increased interest for module performance at non-standard testing conditions, with the aim to enable better simulation of outdoor module behaviour and thus reduce the financial uncertainty even further. Various models underlying energy yield simulations make use of the module temperature coefficients to determine the performance at non-standard operating conditions. Uncertainty in this coefficient contributes to the uncertainty in the energy yield estimation. The effect of this uncertainty will be larger when operating temperatures are far from STC (e.g. hot climates), which can be seen in Figure 36. Here a theoretical 3.6 kW system is designed using NREL's System Advisor Model [41] and an energy yield simulation is performed for a moderate climate (Scheveningen - The Netherlands) and a desert climate (Badla - India), The P_{max} temperature coefficient is varied by 10%, from -0.4% to -0.44% for both climates. Differences in simulated energy yield integrated over the year are 0.3% and 1.3% for the moderate and hot climate respectively by varying the temperature coefficient by 10%. Such differences can have considerable impact on the LCOE as discussed in section 1.3 and are causing financial risk.

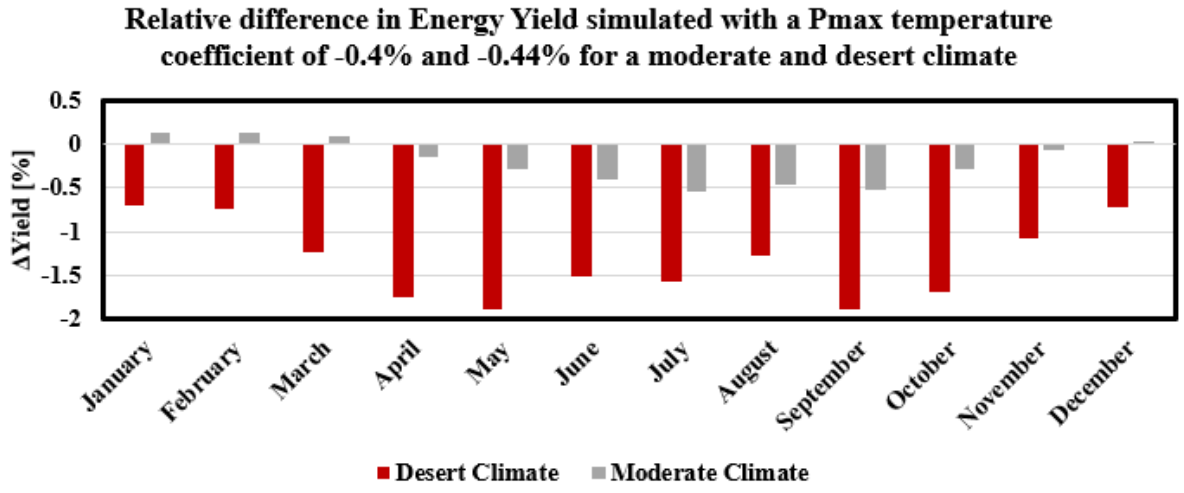

Figure 36: Difference in simulated energy yield for a moderate and desert climate, with a P_{max} temperature coefficient of -0.44%/°C relative to a P_{max} temperature coefficient of -0.4%/°C for a small photovoltaic system. Simulated using the NREL System Advisor Model

5.2 Quantifying uncertainty: Uncertainty analyses

Uncertainty analyses are used to identify and quantify the significant (and insignificant) contributors to measurement uncertainty. One could distinguish two methods: bottom-up and top-down analysis [42]. In the bottom-up analysis, the measurement system and procedure are analysed, uncertainties of all the individual components and procedures are calculated (or estimated, e.g. from practical experience or modelling) and then combined into a final uncertainty number. The top-down analysis is through "round robin" testing, where the uncertainty is determined from the spread of results after measuring a set of the same PV devices at different laboratories and/or using different methods. Both methods complement each other: in the bottom-up approach assumptions and approximations must often be made, which can be validated using the top-down approach. The top-down approach can show differences between laboratories and equipment which then can be understood by looking at the bottom-up analysis. These analyses are generally performed according to the "Guide to the expression of Uncertainty in Measurement" (GUM) [43] developed by the Joint Committee for Guides in Metrology (JCGM). The goal of this guide is to provide basic guidelines for evaluation of uncertainty for a wide range of industries and various fields of research.

5.2.1 Introduction into uncertainty: statistics, uncertainty propagation and the Guide to expression of Measurement Uncertainty

The statistics behind uncertainty and uncertainty propagation will be explained by use of a practical example. Imagine rolling a single "fair" die. There will be equal (1/6) probability on any discrete number from 1 to 6. Now roll another die and sum the result. For the sum to be 2 or 12, both dice need to land on 1 and 6 respectively. The probability to roll one of these numbers is then (1/6)*(1/6) = (1/36). For the sum to be four, it is possible to roll 1 with the first die and 3 with the second, 3 with the first die and 1 with the second and finally it is possible rolling 2 with both dice. Now, there are not one, but 3 possible realizations, visualized in Figure 37. This can be extended to 3 or more dice (or rolls). Figure 38 presents this concept in the form of probability diagrams, also called probability density functions (PDF). For discrete variables this is technically called a probability mass function, in this context no distinction is made since only continuous variables are considered in upcoming paragraphs. Even though a die has a uniform (rectangular) probability distribution, as in the top-left of Figure 38, the more dice (or rolls) are considered, the more the sum of the outcome will look like a Gaussian (normal) distribution, as seen in the bottom-right of Figure 38. Note how the outermost options become more and more unlikely when increasing the number of dice. This is the basis for the Central Limit Theorem, which states that when sufficient samples are summed, the (normalized) summed outcome will approach a Gaussian distribution, no matter the distribution of the individual samples.

	1	2	3	4	5	6
1	2	3	4	5	6	7
2	3	4	5	6	7	8
3	4	5	6	7	8	9
4	5	6	7	8	9	10
5	6	7	8	9	10	11
6	7	8	9	10	11	12

Figure 37: Possible realizations of rolling two fair dice

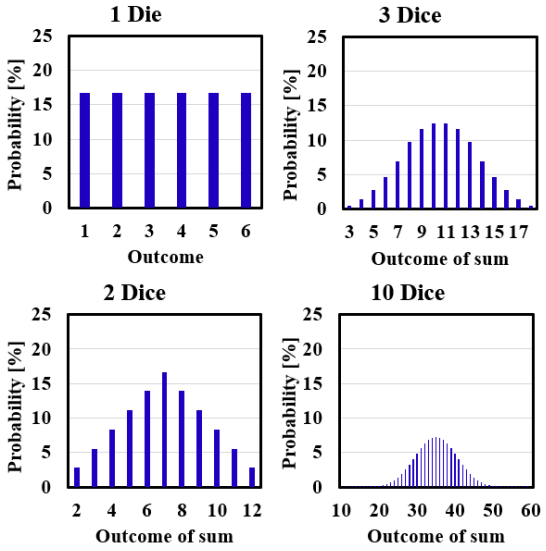

Figure 38: Sum of outcomes plotted against the probability of that sum for 1,2,3 and 10 dice. Note the change in probability distribution with the increasing number of dice.

Uncertainty in photovoltaic measurements works very much in the same way. Often measurements are affected by errors of which the magnitude is not known exactly but can be described in statistical ways. If multiple errors are combined, it is unlikely they all work to their full extend and in the same direction. This is the same principle which makes the probability on the outer limits of multiple dice become lower when increasing the number of dice. A standard T-Type thermocouple, for example, is known to have a maximum error of $\pm$ 1°C. If a module of 25°C would be measured with only 1 sensor, this sensor could measure anywhere between 24°C and 26°C. Assuming this error is randomly distributed with a rectangular (uniform) distribution, there is an increased probability that the errors will average out when more sensors are used. This is similar to the probability diagram of the four dice discussed above and is shown through a Monte Carlo simulation. In such simulations, the outcome of a system is evaluated for a varying range of inputs. In this theoretical example, 1, 4 or 9 sensors are placed in a room at 25°C. By doing many iterations, a large number of errors is sampled from a rectangular distribution, these errors are then used to determine the theoretical sensor readings. These are then plotted in the form of a histogram in Figure 39. The plotted temperatures are determined from the average of 1, 4 or 9 sensors, of which a possible result can be seen in the top row of Figure 39. Note that more sensors isn't necessarily better. In the top-mid graph, the 4 sensor combination is closer to the true value than the 9 sensor combination for a set of 9 sensors. However, as can be seen in the middle and bottom rows of Figure 39, increasing the number of sensors will lead to a smaller spread of possible errors, thus a more accurate measurement result in the majority of cases.

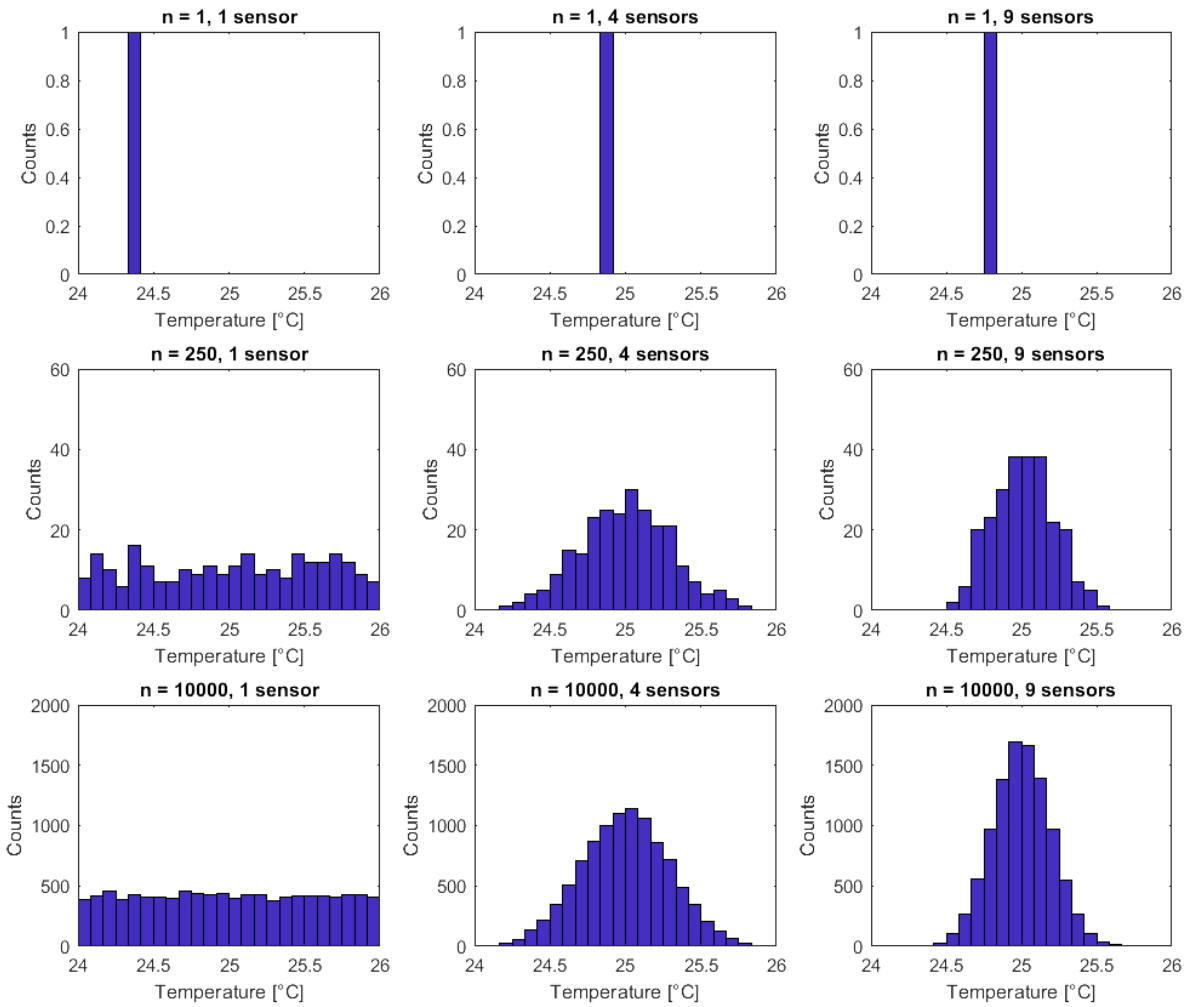

Figure 39: Result of a Monte Carlo simulation on the possible outcomes of 1,4 or 9 T-Type thermocouple(s) measuring a temperature of 25°C for 1, 250 and 10000 iterations

These histograms provide a good indication on the possible spread of the results and start to take a shape similar to the rectangular and the Gaussian distribution when more iterations are considered. Gaussian distributions are determined by two variables: the mean μ and the variance σ^2. For a normal distribution the standard deviation (σ) represents a 68.3% confidence interval: when measuring infinite times, 68.3% of the measurements will fall within this range. A higher confidence interval can be obtained by expanding the uncertainty: 1σ, 2σ and 3σ represent a confidence interval of approximately 68.3%, 95% and 99.7% respectively. Often σ is normalized by the mean, creating the normalized standard deviation. When estimating measurement uncertainty, the (estimated) range of possible errors is described by such probability distributions. The normalized standard deviation of one such distribution is called the relative standard uncertainty. For this work, the rectangular and Gaussian distribution are the most relevant. Rectangular distributions are used when there is only information about the limits, the maximum magnitude of the error and there is no reason to believe the error is biased. Gaussian distributions are used if there is a reason to believe the error is likely to be close to some mean value, but some extremes are observed every now and then, or when the uncertainty component is formed by a combination of various sub-components. When sufficient sub-components are combined, the result will approximate a Gaussian distribution according to the central limit theorem [44].

For uncertainty propagation, 2 cases can be distinguished: addition / subtraction and multiplication / division. If the uncertainties are uncorrelated, addition in quadrature of the standard deviations can be

used to obtain a combined standard uncertainty.

A simplified example of a case where uncertainties are added is presented in the beginning of this chapter (Figure 34). The length of each piece of laminate could be expressed as the "true" length (L) + the error (e) caused by inaccuracy in the cut and the measurement. This error can be described by a probability distribution, determined by the mean μ and standard deviation σ. Here σ represents the uncertainty. As the laminate pieces are both cut with an accuracy of $\pm 0.5cm$ and there is no further knowledge, the error could be described by a rectangular distribution centered around 0, with a minimum and maximum of $\pm 0.5cm$. To calculate the uncertainty of the combined length ($L_1 + L_2$) of the two pieces, the uncertainties (σ_1, σ_2) of both cuts can be added in quadrature as shown in Equation 16. Note that for a rectangular distribution centered around 0, σ is calculated by dividing the limit of the distribution by the square root of 3 and the length of each plint is $30cm \pm 0.5cm$

$$\sigma_{L1+L2} = \sqrt{(\frac{0.5}{\sqrt{3}})^2 + (\frac{0.5}{\sqrt{3}})^2} = 0.41cm \rightarrow L_1 + L_2 = 60cm \pm 0.41cm \tag{16}$$

This means, that the total uncertainty of sawing the two pieces of laminate is $\pm$ 0.41 cm. When taking a total safety margin of 0.41cm (so 0.41/2 cm on each piece of laminate), there is (roughly) an 68.3% (k=1) probability that the pieces fit the gap in your floor. Doubling this safety margin (k=2) to 0.82 cm there is a 95% probability the pieces will fit! Note that in practice, more samples (more plints) should be considered, as the central limit theorem is only valid when the sample size is sufficiently large.

If the uncertainty has to be determined for a product (such as a volume, V), the normalized standard deviations should be added in quadrature as shown in Equation 17. Here L,W and H represent length, width and height, σ_L, σ_W and σ_H represent the uncertainty in length, width and height respectively.

$$V = L * W * H \rightarrow \frac{\sigma_V}{|V|} = \sqrt{(\frac{\sigma_L}{|L|})^2 + (\frac{\sigma_W}{|W|})^2 + (\frac{\sigma_H}{|H|})^2} \tag{17}$$

In case the output has a higher dependency on a change in one variable compared to a change in another variable, sensitivity coefficients can be included. For a general equation $z = f(x, y)$:

$$\sigma_Z = \sqrt{(\frac{\partial z}{\partial x}\sigma_x)^2 + (\frac{\partial z}{\partial y}\sigma_y)^2} \tag{18}$$

5.2.2 Application of the GUM on IV measurements at STC

A number of papers is available in literature where accredited PV laboratories present bottom-up uncertainty analyses for the measurements of PV modules at STC. Even though the GUM provides clear guidelines on the determination and propagation of uncertainties, it is too general to obtain fully consistent uncertainty analyses for specific applications such as photovoltaic measurements. While some components are well-defined and can be quantified using standardized methods, this is not the case for all components. Often the value must be estimated based on results from simulations, real world experience or statistical analysis.

Table 9 shows the major uncertainty contributors for P_{max}, presented by Fraunhofer ISE for the calibration of c-Si PV modules as published in "Uncertainty in PV Module Measurement—Part I: Calibration of Crystalline and Thin-Film Modules" by D. Dirnberger and U. Kraling [7].

Table 9: Uncertainty values reported for the calibration of c-Si photovoltaic modules at Fraunhofer ISE [7]

	Contribution to P_{max} uncertainty [%]
Effective irradiance	0.567
IV Curve	0.367
Reproducibility Factor	0.364
Correction to STC	0.226
Fit	0.044
Temperature	0.033

In equation 19, these components are then added in quadrature to obtain the k = 1 (68.3%) combined uncertainty.

$$u_{Pmax} = \sqrt{u_{Irr}^2 + u_{IV}^2 + u_{Repro}^2 + u_{STC}^2 + u_{Fit} + u_{Temp}^2} = 0.802\%, k = 1. \tag{19}$$

Expanding this uncertainty to a k = 2 (95%) confidence interval results in $u_{Pmax}(k = 2) = 2 * 0.802\%$ = 1.6%, which is a typical uncertainty on the P_{max} of Fraunhofer reference modules used in many labs and factories as a calibration standard for their equipment.

The **effective irradiance** describes the uncertainty on the absolute value of the actual irradiance incident on the module. This comprises amongst others the calibration uncertainty of the World Photovoltaic Scale (WPVS) reference cell (this is measured simultaneously with the device under test (DUT) at Fraunhofer, and can be considered an alternative to the reference module commonly used at Eternalsun Spire), light uniformity and spectral mismatch. Uncertainty on the **IV curve** is related to effects that affect the shape of the IV curve, rather than just I_{sc} or V_{oc}. An example could be capacitive effects [45], which under- or overestimates the measured module current (thus changes the IV curve) depending on the direction (I_{sc} to V_{oc} or reverse) of the IV sweep. This effect is especially relevant for high efficiency c-Si technologies. The **reproducibility factor** accounts for uncertainties and correlations not aware of and/or not considered in the others, such as inconsistencies in the procedure or variations in test conditions. This number is based on measurements on 9 modules with the same method every 3 weeks for multiple years, the spread of the results is considered to be the uncertainty. **Correction to STC** uncertainties are related to imperfect knowledge of correction parameters such as temperature coefficients, which are required for correction of the measurements to STC. These corrections to STC allow for industry wide comparability of the results. The uncertainty of the **Fit** accounts for uncertainty between conversion of the rough data towards the final parameter. Electrical noise for example can introduce (small) irregularities in the module IV data. Generally, the presented IV curve and its parameters are the result of a fit between these rough data points. Finally the **Temperature** component accounts for uncertainties in the true module temperature. This can, amongst others, be caused by inaccuracies of the temperature sensors, or deviations between the cell temperature and the temperature measured at the outside of the module.

A more visual way to show the contribution of each uncertainty component is by the use of the sunburst diagram in Figure 40. In this figure also the most relevant sub-components of each uncertainty factor are shown. Note that for this figure, the uncertainty contributions from Table 9 are squared, showing their actual contribution to the final combined uncertainty, as this is calculated by addition in quadrature. It can be seen that a large part of the P_{max} uncertainty is related to uncertainty in light intensity and spectrum.

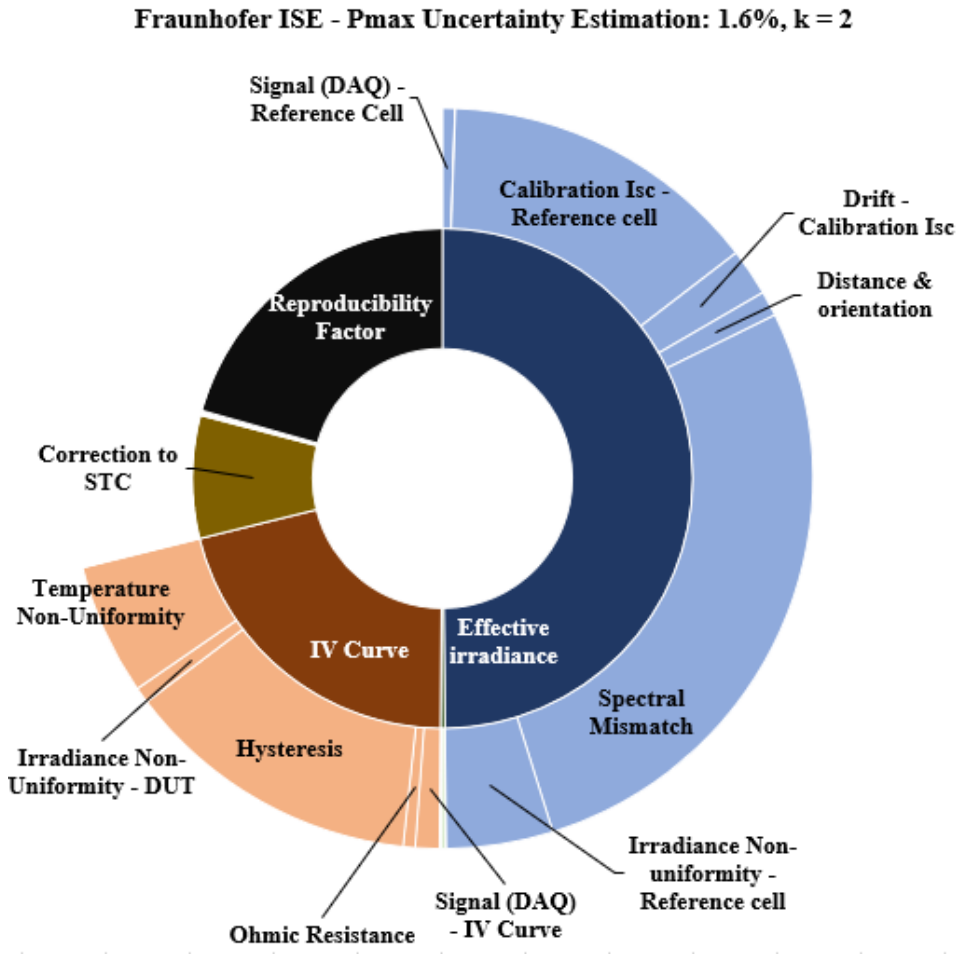

Figure 40: Visual interpretation of uncertainty drivers for the calibration of c-Si photovoltaic modules at Fraunhofer ISE [7]

The sub-components will be briefly explained, a more detailed explanation is available in Appendix A. Uncertainty in the **Signal (DAQ) - Reference Cell**, affecting the irradiance measurement, is mainly the result of noise on the signal going from the calibrated WPVS reference cell to the DAQ. Additionally, the DAQ itself can introduce noise or offsets into the signal. Generally, many samples are considered and averaged, which reduces the effect of signal noise. In combination with accurate electrical calibration of the DAQ, this results in a relatively low contribution to the uncertainty. The **Calibration I_{sc} - Reference cell** represents uncertainty of the I_{sc} value of the WPVS reference cell at $1000W/m^2$. At Fraunhofer, a "primary" reference cell is used, calibrated with a very low uncertainty by PTB (the National Metrology Institute in Germany). This calibration value changes slightly throughout the years e.g. by material degradation, which is covered by the **Drift - Calibration** I_{sc} component. The change of the calibration I_{sc} is estimated from yearly recalibrations of the cell. The **Distance & Orientation** component accounts for any differences between the distance or angle of the device used for calibration (in this case the WPVS reference cell), to the light source and the distance or angle of the device under test (DUT) to the light source. Naturally, when one of the devices is closer to the light source, the intensity of the incident light will be higher. The **Spectral Mismatch** accounts for any uncertainty resulting from differences in the spectral response of the WPVS reference cell and the DUT. While corrections are applied for these differences, there will always remain uncertainty as the spectral response of the DUT and reference cell are only known with some uncertainty and so is the spectrum of the simulator. **Irradiance Non-uniformity - Reference cell** covers uncertainty by non-uniformity in the irradiance, which can cause that the irradiance measured by the WPVS reference cell is not fully representative for the irradiance incident on the DUT. This will cause a (systematic) offset error when correcting to the target irradiance

(e.g. $1000W/m^2$ at STC).

In the IV curve uncertainty budget, there is another DAQ related component: the **Signal (DAQ) - IV Curve** component. This accounts for the signal noise and DAQ offset on the current and voltage measurement of the DUT, thus on the IV curve itself. **Ohmic resistance** accounts for any additional resistance between the 4-wire measurement point and the DUT (such as bad connectors, or cable adapters). Additional resistance could cause a small shift in the voltages in the IV curve. The **Hysteresis** is related to the difference in forward/backward sweeping, which is caused by module capacitance in combination with a dynamically applied load. **Irradiance non-uniformity** in the area where the **DUT** is illuminated can reduce all module currents, but also affect the shape of the IV curve. An example would be when a bypass diode is activated because of a cold spot on the test surface (a spot where the light-intensity is lower). This is essentially the same as partial shading of a module. If not all the PV module substrings (a substring being a string of series-connected cells protected by one bypass diode) are affected, this will mainly affect the P_{max} of the module rather than I_{SC} or V_{OC}. Temperature non-uniformity can also create additional effects on the IV curve, the uncertainty caused by temperature non-uniformity is determined by multiplying the temperature coefficients by the maximum temperature non-uniformity.

5.2.3 Application of the GUM on PV Temperature Coefficients

Most of the analyses, such as the one discussed in previous section, aim to determine the measurement uncertainty for STC conditions. In "Uncertainty Estimation of Temperature Coefficient Measurements of PV Modules", by B.Mihaylov et al [46], probably the only bottom-up uncertainty analysis applied on setups that measure PV temperature coefficients is presented. An analysis similar to the one from Fraunhofer ISE is performed, which is then extended to determine the measurement uncertainty of temperature coefficients as well as measurement uncertainty values for the temperature and irradiance levels in the IEC61853-1 Power Matrix. The overview of the model underlying the uncertainty analysis is shown in Figure 41. IV and temperature measurements are obtained at different temperatures. The P_{max} uncertainties are obtained and split in systematic and random sources and the uncertainty of the temperature coefficient is then calculated using an algorithm implementing a Generalized Gauss Markov Regression by NPL [47]. This method is basically a weighted least squares method to obtain linear fits, which can also take into account correlations between the uncertainties at different points.

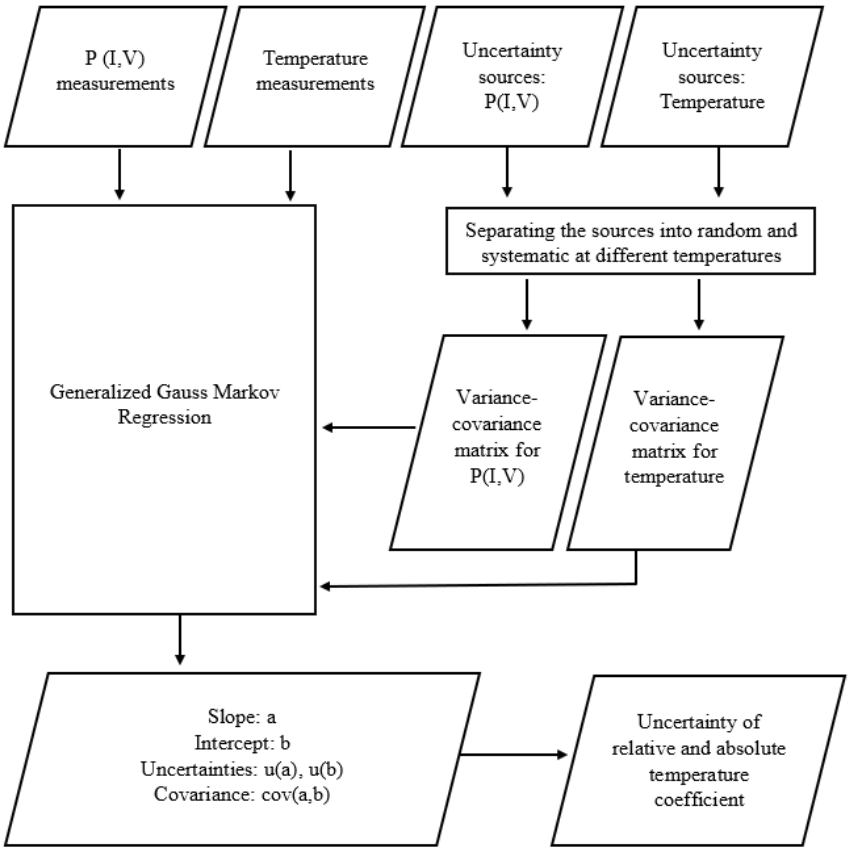

Figure 41: Procedure for evaluation of temperature coefficient uncertainty presented in "Uncertainty Estimation of Temperature Coefficient Measurements of PV Modules", by B.Mihaylov et al. Figure adapted from last-mentioned

This uncertainty analysis is then applied on 5 different measurement setups. To evaluate the validity of the analysis, two c-Si modules are tested on each of the 5 setups. The results are presented in Figure 42. For system A and B, the modules are tested in a temperature controlled chamber with a glass window, with an AAA and BBB class pulse based solar simulator respectively. System C is a continuous solar simulator that heats the PV modules by radiation. System D is an outdoor setup, where the modules are heated by natural illumination under clear sky conditions. In system E the modules are heated via a contact-heating mat and IV measurements are taken while the modules cool down. Temperature measurements in system E are based on a method developed at CREST, which uses the module voltage at a pre-defined injected current level to determine the module temperature. This is further elaborated in aforementioned work from Mihaylov et al. The observed deviations in P_{max} temperature coefficients are in agreement with the estimated uncertainties for four out of the five setups. The deviations from system B, the only system where the results are not within estimated uncertainty levels, are reportedly believed to be caused by emission peaks in the wavelength region where the spectral response of the PV modules shifts with temperature (this will be further discussed in section 5.5.3). The interaction of emission peaks with the (temperature induced) change in spectral response of the modules is not fully accounted for in the uncertainty estimation, resulting in an underestimation of the uncertainty of system B.

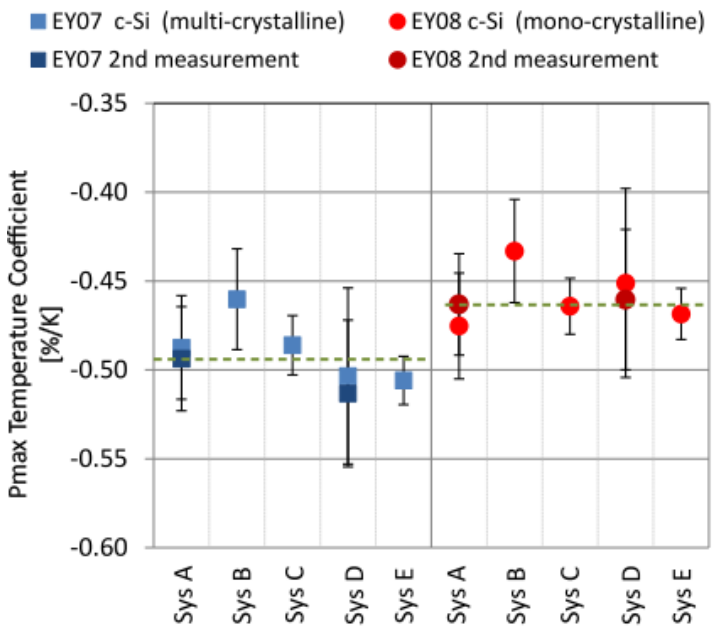

Figure 42: Temperature coefficients of two c-Si modules measured at 5 different measurement setups, including error bars as determined using uncertainty analysis presented above. Figure from: B. Mihaylov et al, "Uncertainty Estimation of Temperature Coefficient Measurements of PV modules"

5.3 Uncertainty analysis on the temperature coefficient setup

In this subsection, the uncertainty analysis on the developed measurement setup is presented. Emphasis will be on the module power, P_{max}, and its temperature coefficient, however a similar procedure holds for the other module parameters as well. First, section 5.3.1 will discuss the used uncertainty model. The inputs for this model are the STC uncertainties related to P_{max}, which will be discussed in section 5.3.2 and the temperature related uncertainties, which will be discussed in section 5.3.3. Finally, the results of the analysis are presented in section 5.3.4.

5.3.1 The uncertainty model

The uncertainty model is based on a Monte Carlo approach [48]. In this method, a quantity is iteratively calculated, each time varying the input data based on assigned probability distributions. The spread of the outcome of the results can then be used to estimate the propagation of the uncertainty. In this model, the iteratively calculated quantity is the temperature coefficient, and the varying input data are the errors affecting the temperature coefficient (further elaborated in section 5.3.2 and 5.3.3).

These variable inputs (errors) in the Monte Carlo simulation need to affect a set of initial power and temperature data. This data is based on a theoretical module of which the "true" P_{max} at STC and the "true" P_{max} temperature coefficient are assumed to be known. This P_{max} and its temperature coefficient are 300W and -0.4%/°C respectively. Based on these numbers, two vectors, one with P_{max} values and one with module temperature values are formed, which represent the (theoretical) "true" P_{max} values at a selection of module temperatures. The P_{max} and its temperature coefficient are representative for 60 cell PERC based c-Si modules, currently widely available in industry. The temperatures considered are based on the IEC69853-1 power matrix (section 2.3.2) supplemented with the minimum and maximum module temperatures that can be obtained in the temperature chamber. These vectors are from here on referred to as the baseline data: P_{max} = [318 312 300 270 240 228]; Temperature = [10 15 25 50 75 85].

The outcome of the model will be a set of temperature coefficients, obtained by least square fits of the corresponding P_{max} and temperature vectors. These vectors are formed from baseline data affected by the estimated measurement errors (of which the latter are varied each iteration). This can then be compared with the baseline data and corresponding temperature coefficient, to determine the combined effects of all the uncertainty contributors.

A condensed version of of a single iteration is shown in Figure 43. This example assumes 4 uncertainty contributors: two scale factor uncertainties and two random uncertainties. Additionally, only three P_{max} and temperature data points are considered for the baseline data. Each iteration starts with the baseline data, plotted in Figure 43-A. Figure 43-B then shows the result of applying the first scale factor error, sampled from the corresponding Gaussian distribution. The result of this will then be used as an input for the second scale factor error in 43-C (which is sampled from another distribution). After this, the two random errors are consecutively added in figure 43-D and 43-E. Finally the result from all the combined effects is shown (next to the baseline data) in Figure 43-F. Note how each scale factor error results in a rotation around 25°C and thus affects all the data points. Random errors will instead affect each data point individually, thus multiple errors need to be sampled from the same distribution every iteration when applying a random error as shown in 43-D and 43-E. This procedure will then be iterated, creating a range of possible outcomes.

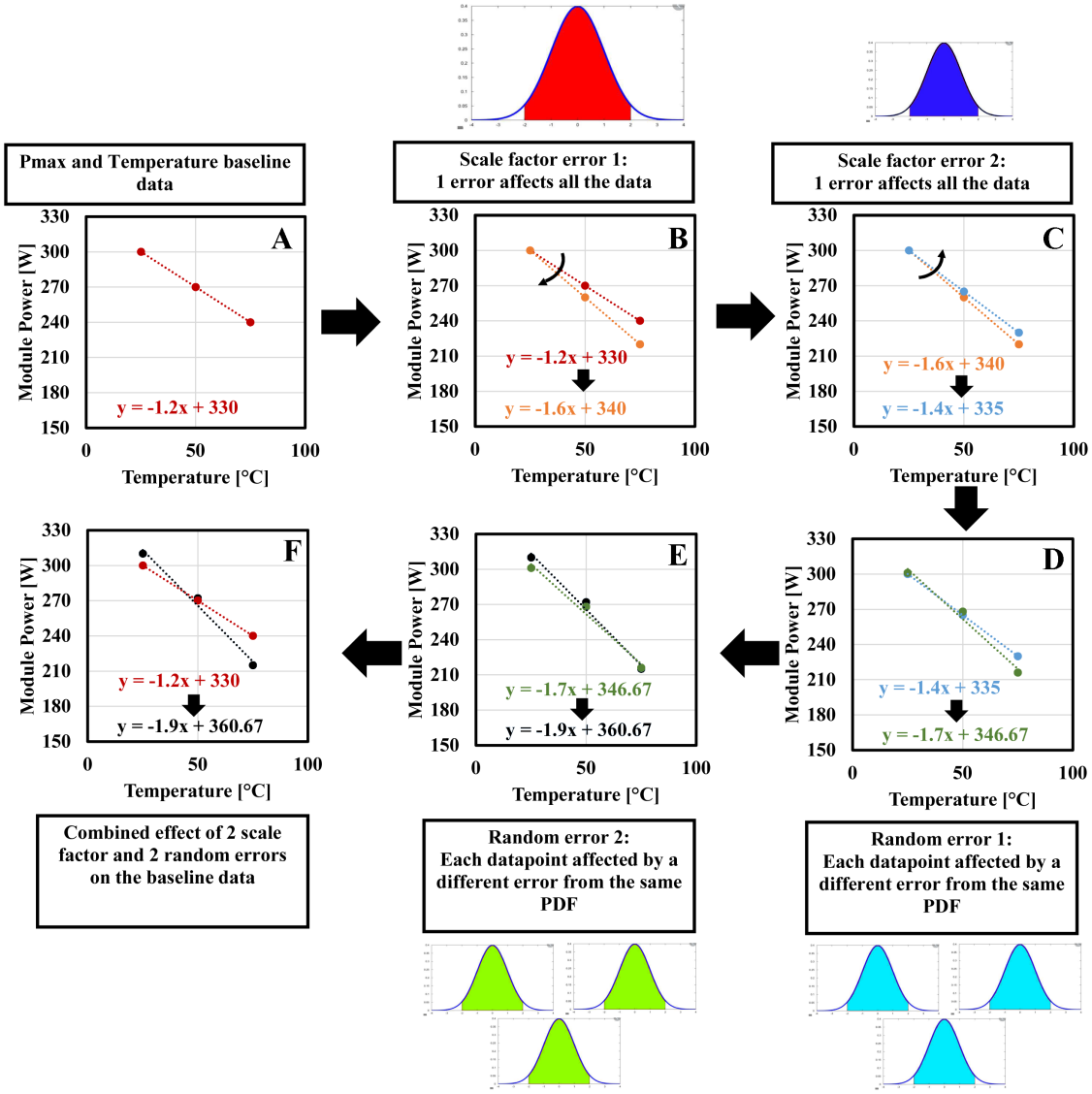

Figure 43: Application of a Monte Carlo simulation to determine the uncertainty propagation of various independent uncertainty contributors which are described by a probability density function

By comparing the range of outcomes with the baseline data, the uncertainty of the temperature coefficient can be estimated. Distinction is made between absolute and relative temperature coefficients. The absolute coefficient is the slope of the fit of P_{max} and the module temperature, the relative coefficient is the slope divided by the STC value of P_{max}. Consequently, the uncertainty of the absolute coefficient equals the uncertainty of the slope and the uncertainty of the relative coefficient is a result of the combined uncertainty of the slope and the STC uncertainty. For the uncertainty of the slope of the fit (the absolute temperature coefficient), it is important to distinguish offset, scale factor and random errors as these affect the temperature coefficient differently as observed seen in Figure 43-C and 43-D. This is additionally visualized in Figure 44. For the absolute temperature coefficient, any offset error can be neglected, as these do not affect the slope of the fit. Scale factor errors are often proportional to the temperature deviation from STC temperature (25°C), resulting in a rotation around 25°C. These errors thus have direct impact on the temperature coefficient. Random errors affect each point individually and in a random direction, thus usually have little effect on the slope of the fit.

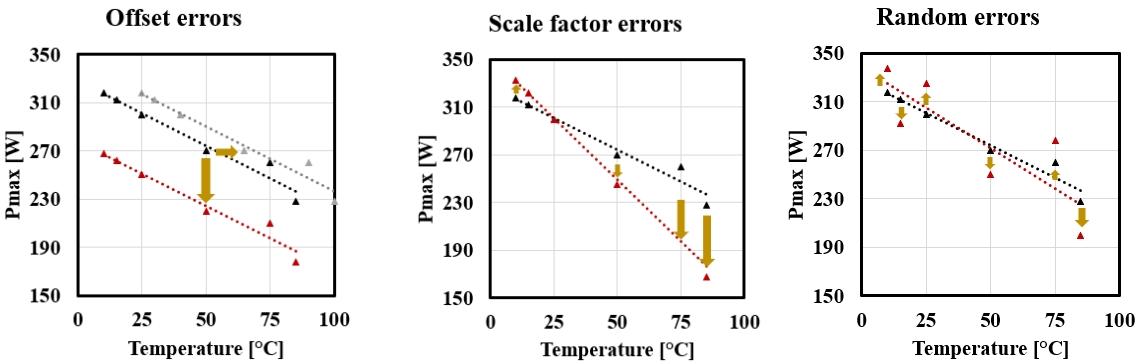

Figure 44: Visualization of offset, scale factor and random errors. Offset errors do not affect the slope of a fit, scale factor errors strongly affect the slope, random errors affect the slope to a limited extend. The effect of random errors will however decrease when considering more measurement points

To summarize the model: based on observations and estimations which will be discussed in section 5.3.2 and 5.3.3, probability density functions are created to describe each relevant uncertainty components. From these PDF's, scale factor and random errors are pseudo randomly sampled and the effect of these errors is then consecutively applied on the P_{max} versus temperature data. When all the errors are applied, an ordinary least squares fit is obtained and the slope and intercept of this fit are saved. This process is iterated for a large number of times, resulting in a range of possible fits. The mean and standard deviation of this fit are then analyzed and compared to the fit of the baseline values. The estimated uncertainty for the absolute temperature coefficient is then determined from the difference and spread between the simulated results and the baseline. The relative temperature coefficient is obtained by dividing the absolute temperature coefficient by the STC value. The uncertainty of the relative temperature coefficient is obtained through addition in quadrature of the uncertainties of both the absolute temperature coefficient and the STC value.

5.3.2 Uncertainty budget at standard testing conditions

Figure 45 shows the uncertainty budget for the Eternalsun Spire temperature coefficient setup at STC. Note that uncertainty components that have less than 2% contribution to the STC P_{max} are unmarked for readability. The relative contribution of each component depends on various drivers such as light quality, electrical calibration, environmental effects, module technology and operating procedures, thus Figure 45 is only valid under specific assumptions and conditions. In this case, a c-Si DUT is assumed and the setup is calibrated with a spectrally matched reference module (a module with the same spectral response as the DUT). As a result of this assumption, uncertainty caused by spectral mismatch is considered negligible. In practice there will always remain some uncertainty because of module to module variation. Uncertainty resulting from environmental effects is reduced by the temperature chamber which reduces effects such as incorrect temperature measurements caused by surrounding heat sources. A very good example of such an effect is shown in Figure 8 from [49], where an infrared (IR) reflection of the operator that handled the DUT is visible on the IR image, indicating a locally higher temperature. This would have resulted in a measurement error if an IR sensor was used for the temperature measurement. The uncertainty build-up will be different when other assumptions are made (e.g. a different module is tested), this will be discussed in section 5.4.

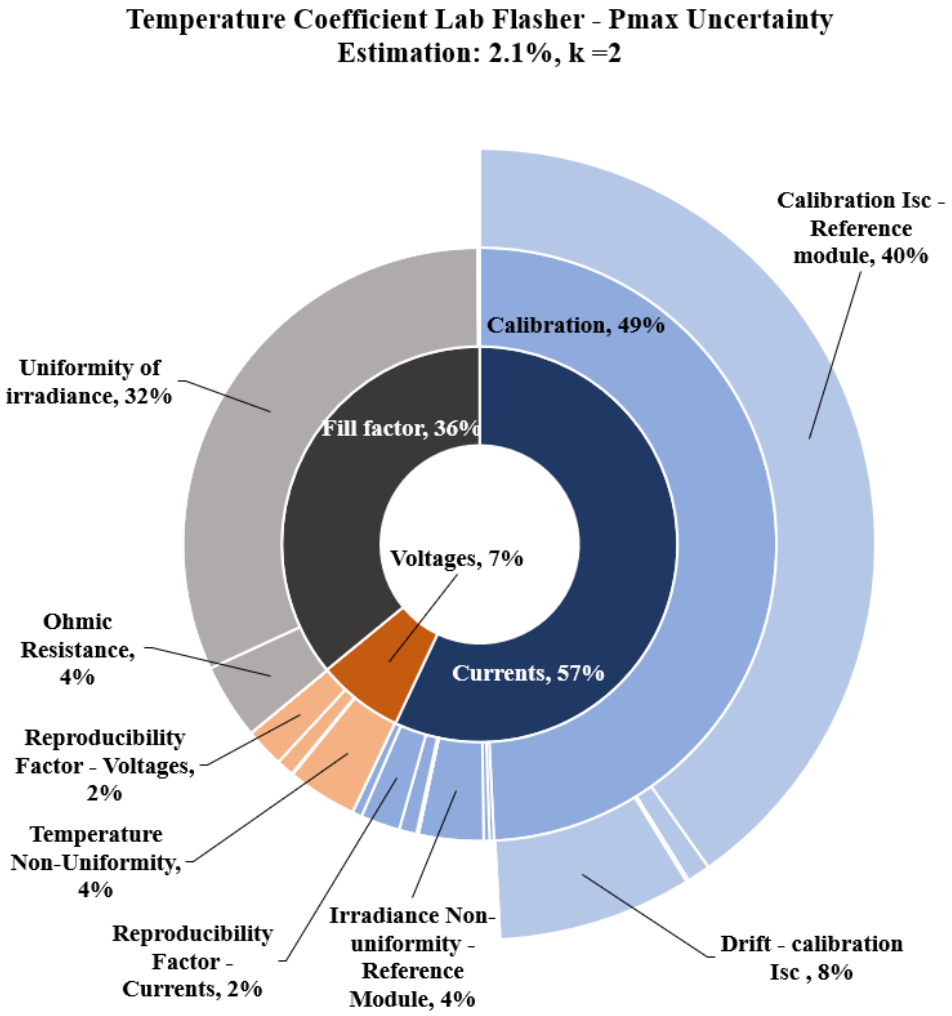

Figure 45: Uncertainty contribution of various uncertainty drivers in the Eternalsun Spire Temperature Coefficient setup, assuming a c-Si module under test with a spectral response matched reference module. Note: uncertainty drivers with a contribution below 2% are unmarked to improve readability

As seen in Figure 45, the largest effects are the result of optical components: the uncertainty on the calibration value of the reference module and the non-uniformity of the irradiance of the simulator. In practice, a third very significant effect is the spectral mismatch, which can be partially mitigated using spectral mismatch correction. This effect is currently not considered as it is assumed that a spectrally matched reference module is used for calibration. One could consider this close to optimal conditions. A summary of the largest effects and their magnitude will be given below in Table 10 - 12, a more extensive description and more background information is provided in Appendix A. As the uncertainty of P_{max} at STC is not the main goal of this thesis, many of the components presented in this section are based on previous estimations by Eternalsun Spire. Where possible, these estimations were evaluated and some uncertainty components were added or changed based on this work. This resulted in a more detailed and more extensive estimation of the STC uncertainty budget at Eternalsun Spire.

Table 10: Summary of uncertainties affecting the module short-circuit current. Note: the coverage factor describes the confidence level as discussed in section 5.2.1

Uncertainty in the currents				
	Estimated uncertainty [%]	Coverage factor	Distribution	Standard uncertainty [%]
Calibration Isc – Reference module	1.30	2	Normal	0.65
	▪ Provided by the calibration institute (Fraunhofer ISE) ▪ Based on the uncertainties of the setup and procedure used by the calibration laboratory and their reference device			
Drift – calibration Isc	0.5	1	Rectangular	0.289
	▪ Observations in literature for recalibration of c-Si reference cells [7], conservatively increased by 50% as a module is used ▪ Assumed yearly calibration ▪ Assumed correct handling (no damaging of the module, no additional microcracks)			
Uniformity of test area and form factor on calibration	1	3	Rectangular	0.193
	▪ Affected by the uniformity of the simulator o ± 0.9% over 96 locations (IEC60904-9), measured in high resolution ▪ Non-uniformities create local hot/cold areas similar to module shading, reducing cell currents, I_{SC} will be limited by the cell producing the least current that is not bypassed, often located at a cold area ▪ Assumed a reference module is used of similar size as the device under test. Coverage factor k = 3, as any cold spot affecting the calibration module will very likely also affect the DUT			
Reproducibility Factor - Currents	0.3	2	Normal	0.15
	▪ Based on statistical observations where a set of 10 modules is tested by different trained operators in-line in a top tier manufacturer ▪ Reproducibility effects could be caused by e.g. different placement of the module (indirect non-uniformity effects) or electrical signal noise ▪ Repeatability effects account for flash-to-flash variation, and accounts for random uncertainties not considered or not known of			

Table 11: Summary of uncertainties affecting the module open-circuit voltage. Note: the coverage factor describes the confidence level as discussed in section 5.2.1

Uncertainty in voltages				
	Estimated uncertainty [%]	Coverage factor	Distribution	Standard uncertainty [%]
Temperature Non-Uniformity	0.2	1	Normal	0.2
	▪ Effects of incorrect temperature measurement on the voltage correction of the module. ▪ Based on a 0.3%/°C Voltage temperature coefficient multiplied with the temperature uncertainty			
Reproducibility Factor - Voltages	0.3	2	Normal	0.15
	▪ Based on statistical observations where a set of 10 modules is tested on a similar solar simulator by different trained operators in-line in a top tier manufacturer ▪ Reproducibility uncertainty of voltages is mainly caused by differences in environmental circumstances (temperature). As the bespoke setup has integrated temperature control capabilities, this value is likely conservative			

Table 12: Summary of uncertainties affecting the module Fill Factor. Note: the coverage factor describes the confidence level as discussed in section 5.2.1

Uncertainty in Fill Factor				
	Estimated uncertainty [%]	Coverage factor	Distribution	Standard uncertainty [%]
Ohmic Resistance	0.2	1	Normal	0.2
	▪ Additional resistance between the module leads and the 4-wire measurement point can create a shift in the voltages except for V_{OC}			
Uniformity of irradiance - DUT	1	1	Rectangular	0.577
	▪ 3 times the uncertainty in Isc assuming 3 bypass diodes, confirmed with customer data where a reduction of 1% irradiance non-uniformity on a number of Eternalsun Spire solar simulators led to a reduction in simulator-to-simulator fill factor deviation of 0.6%			

The total combined uncertainty for the P_{max} measurement at STC using the TCLF is estimated at 1.05%, k=1, more commonly reported in the form of the expanded uncertainty: 2.1%, k=2. For the absolute temperature coefficient (the slope), all the offset uncertainties can however be ignored as described earlier in Figure 44. These offset uncertainties mainly comprise the optical uncertainties. The remaining uncertainties that are relevant for the uncertainty of the absolute temperature coefficient are the repeatability of the P_{max} and Temperature measurement as shown in Table 13. These both can be considered random errors and are directly obtained by statistical analysis on the measurement data.

Table 13: Summary of the STC uncertainties that can affect the absolute temperature coefficient

	Estimated uncertainty	Coverage factor	Distribution	Standard uncertainty
Repeatability Factor - P_{MAX}	0.15	2	Normal	0.075%
	▪ Based on various 16 hour tests, performed at discussed setup as well as similar solar simulators ▪ Normalized standard deviation of P_{MAX} below 0.15%			
Repeatability Factor – Temperature measurement	0.01°C	1	Normal	0.01°C
	▪ Based on maximum standard deviation of 3 consecutive measurements with 15 second interval, in 25 minutes of measurement data. A limited number of consecutive measurements is considered to limit the effect of changing temperatures.			

5.3.3 Temperature effects on the uncertainty budget

This section will elaborate on uncertainty components that become (more) relevant when testing at temperatures other than STC temperature. Three components will be discussed: spectral mismatch, the monitor cell temperature coefficient (which corrects the irradiance measurement) and scale factor errors in the module temperature sensors.

Spectral Mismatch at elevated temperatures

The first uncertainty component significantly affected by temperature is the spectral mismatch (MM). Equation 20 [50] shows how to calculate MM. MM is used as a correction factor for differences between the AM1.5G (STC) spectrum ($E_{ref}(\lambda)$) and the solar simulator spectrum ($E_{meas}(\lambda)$), taking into account the spectral response (SR) of both the reference device (used for calibration and/or to obtain a directly traceable irradiance measurement) ($S_{ref}(\lambda)$) and the DUT ($S_{sample}(\lambda)$). MM is unity if either the reference/calibration device and the DUT have the same SR, or if the solar simulator has a perfect AM1.5G spectrum (which is never the case in practice). If MM is above unity, the DUT can utilize a

larger part of the spectrum (thus effectively receives more irradiance) compared to the reference device and vice versa when MM is below unity. This can be corrected for by dividing the measured currents, thus also P_{max}, by MM.

$$MM = \frac{\int E_{ref}(\lambda)S_{ref}(\lambda)d\lambda \int E_{meas}(\lambda)S_{sample}(\lambda)d\lambda}{\int E_{meas}(\lambda)S_{ref}(\lambda)d\lambda \int E_{ref}(\lambda)S_{sample}(\lambda)d\lambda} \tag{20}$$

As discussed in section 2.4.1, the bandgap of the c-Si devices decreases with increasing temperature, increasing the probability for low-energy (high wavelength) photons to generate electron-hole pairs. This results in an increased SR at the near-bandgap wavelengths. Figure 46 shows the SR of a c-Si cell measured at 10°C, 30°C and 60°C.

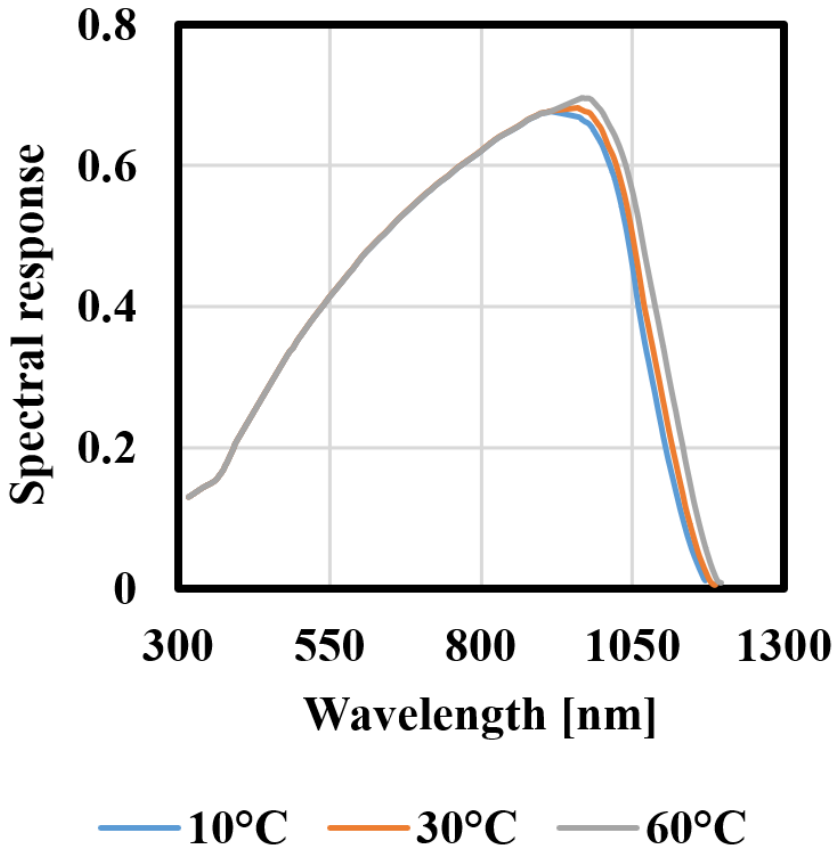

Figure 46: Measured spectral response of a c-Si cell at 10°C, 30°C and 60°C. Image adapted from: Y. Yang et al, "Understanding the uncertainties in the measurement of temperature coefficients of Si pv modules" 29th EUPVSEC, 2014 [8]

As a result the change in spectral mismatch with temperature, depending on the change in SR and the spectrum of the solar simulator. To estimate the effects of this SR change in combination with the developed setup, MM is calculated for different temperatures. In Figure 47, the calculated MM is compared with the MM at 25°C. It shows that MM decreases approximately linear with temperature considering the SR at 25°C as a reference. As a result, module currents (and thus P_{max}) would be underestimated by approximately 0.47% at a temperature of 65°C. This is in agreement with expectations as the energy content in the simulator spectrum is below the energy content in the AM1.5 spectrum in the wavelength region where the change in SR occurs (as was observed previously in Figure 16). For STC measurements MM is corrected for, either by using MM to set the proper light intensity, or by using MM to correct the measurement results afterwards. At elevated temperatures, this correction could also be performed [51], however in many cases temperature-dependent SR data (or the equipment to measure this) is not

available and no procedure is given in the widely used IEC standards [50].

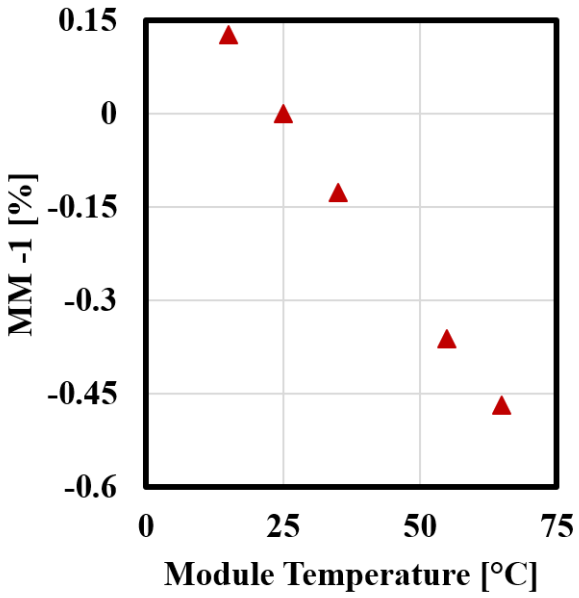

Figure 47: Variation of spectral mismatch with temperature, relative to spectral mismatch at 25°C

In a recently published paper by Y. Hishikawa et al. [52], the effect of temperature on spectral response of several c-Si modules is studied. The measured SR of various cells in mentioned work are used to determine the MM at 25°C and 65°C with the solar spectrum of the TCLF, of which the result is presented in Figure 48. As MM is approximately linear with temperature, the change in MM can be calculated in %/K. The average, -0.00957%/K, and standard deviation, 0.00266%/K, of the 5 considered cells are used to form a normal distribution describing this effect. It has to be noted that this effect could be larger for other c-Si cells and modules, however only a limited amount of data is currently available and more research is recommended. As it is assumed that this effect is not corrected for, the error because of MM is fully propagated into the total uncertainty budget even though it is biased to one side.

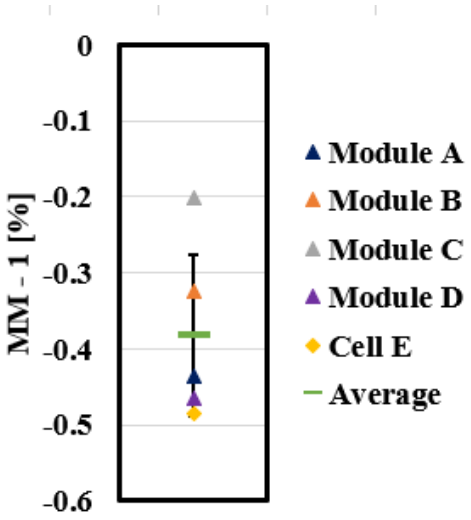

Figure 48: Spectral mismatch at 65°relative to 25°C as a result of the temperature induced change in spectral response of c-Si modules

The Monitor Cell Temperature Coefficient

The second uncertainty component is the temperature correction of the monitor cell (MC), a small c-Si cell placed in a regulation loop with the simulator lamps. This cell controls the irradiance based on the cell I_{sc} and a target current set during calibration. If the temperature of the monitor cell increases, the provided current should be corrected using equation 21 and the I_{sc} temperature coefficient of the MC to keep the lamps at the target irradiance. Here $I_{RC-corr}$ is the corrected I_{sc}, $I_{RC-meas}$ represents the uncorrected I_{sc} measured by the MC, α_{RC} is the I_{sc} temperature coefficient of the MC and T the MC temperature. As can be concluded from the large deviations between I_{sc} temperature coefficients observed in Section 4, this coefficient is hard to determine accurately, since it is both very small as well as a function of the simulator spectrum.

$$I_{RC-corr} = I_{RC-meas} * (1 - \alpha_{RC} * (T - 25°C)) \tag{21}$$

As long as the temperature is close to 25°C (STC temperature), the effect of an incorrect MC temperature coefficient is very limited. In the temperature coefficient setup however, even though the monitor cell is not directly in the temperature chamber but underneath the glass in the solar simulator, the monitor cell reaches temperatures up to approximately 65 °C during a typical temperature coefficient test, as can be seen in Figure 49. As a result, the effect of small errors in the MC temperature coefficient is amplified by large temperature deviations from STC.

As the MC short-circuit current is directly proportional to the irradiance, an error in temperature coefficient directly results in an offset in the irradiance. Figure 50 shows this effect for errors in MC temperature coefficient up to 50%. Note that the horizontal axis expresses module temperature, thus there is still some error at a module temperature of 25°C, as the monitor cell temperature is still a few °C higher as seen in Figure 49.

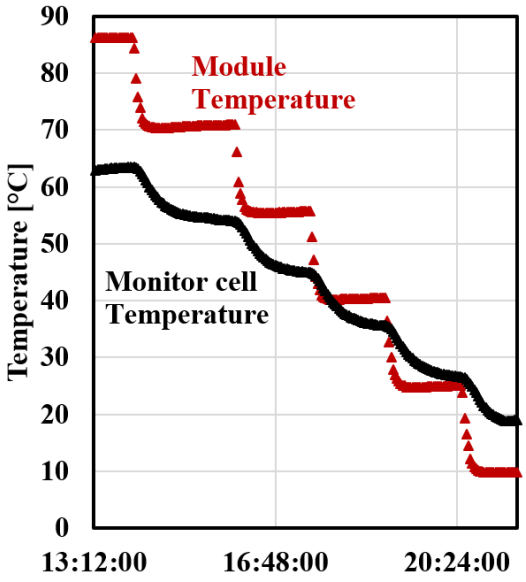

Figure 49: Monitor cell temperature and module temperature during a typical temperature coefficient test with the Eternalsun Spire temperature coefficient setup

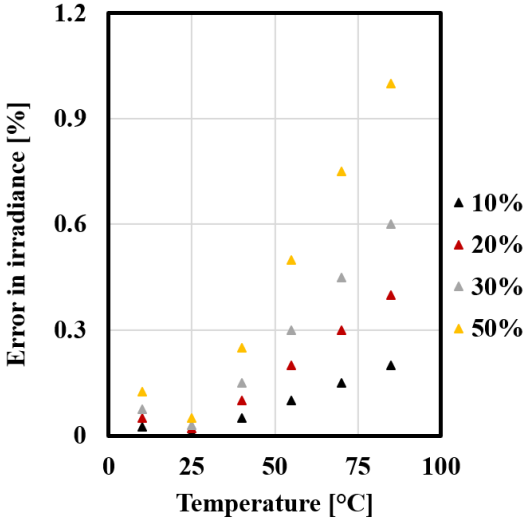

Figure 50: Error in irradiance at different module temperatures as a function of the magnitude in monitor cell temperature coefficient error

The temperature coefficient of the monitor cell is currently determined using a goal seek method. In this procedure a module with a well known I_{sc} temperature coefficient is placed on the simulator and is flashed with an interval as short as possible to heat the monitor cell. The trend between the monitor

cell temperature and the module I_{sc} is used to determine MC temperature coefficient. This temperature coefficient is then entered and the procedure is repeated to ensure the module I_{sc} remains stable. It is estimated by Eternalsun Spire that this procedure can obtain the MC temperature coefficient with a relative accuracy of approximately 20% (thus 20% of the I_{sc} temperature coefficient). This estimation is based on data provided by various customers of Eternalsun Spire, such as PV module manufacturers. Note that this effect can go either way, e.g. the coefficient can be 20% too high or 20% too low. When testing around STC, this is sufficiently accurate, as the monitor cell will hardly reach temperatures above 30°C under normal operation (in typical lab environments). For temperature coefficient testing, an error in the MC temperature coefficient in combination with large deviations from STC temperature, can result in significant errors in the measured temperature coefficients of the device under test. An alternative procedure to determine the MC temperature coefficient will be elaborated in section 6.

Temperature sensor scale factor errors

A third source for errors in the temperature coefficient measurement is the measurement accuracy of the temperature sensors. These sensors can have a measurement offset from the "true" temperature (e.g. always measure 0.5°C above the true temperature) and measurement scale factor errors (e.g. measure 0.5°C below the true temperature at 0°C and 0.5°C above the true temperature at 100°C). While offset errors will not affect the slope of the temperature coefficient, scale factor errors have direct impact.

The standard setup makes use of T-Type thermocouples. For T-Type thermocouples, the manufacturer accuracy specification is ± 1°C. In a theoretical worst case scenario, the sensors would measure 1°C below the "true" temperature at one side of the used module temperature range (10°C to 85°C), and 1°C above the "true" temperature at the other side of this range. The probability on this is however very low, as the measurement range of these specific T-type thermocouples is approximately 210°C and the ± 1°C measurement accuracy specification should also hold outside the 10°C - 85°C range.

To estimate a more realistic value of the scale factor error, the 9 T-type sensors available in the setup are wrapped closely together in a small piece of thermally conducting aluminium tape, which should give each sensor the same temperature. The bundled sensors are placed in the temperature chamber. The temperature of each individual thermocouple at 25°C and 75°C air temperature is compared with the temperature averaged from the 9 sensors. Based on extrapolation of these results, the scale factor error is estimated to be ±0.15°C over the range from 10°C to 85°C. As the scale factor errors of the 9 sensors are spread quite uniformly, this effect is modelled as a rectangular distribution, with the edges at ±0.15°C. The temperature scale factor error will work proportionally to full extent on both sides. Note that this could theoretically be biased as all sensors could e.g. be from a same batch with the same material properties and the average from the 9 sensors might be biased to some extend.

Another possible way would be to scale the accuracy limits by the fraction of the measurement range used. The ±1°C is for these specific thermocouples is valid for the a measurement range from -75°C to 135°C. Considering the module temperature is measured from 10°C to 85°C, the fraction of the range would be 75/210=0.35°C. The accuracy specification could then be scaled, to ±0.35 °C. Note that this approach is not valid for the temperature offset, only for temperature scale factor as absolute errors can still be up to ±1°C.

Increasing the number of sensors can average out effects of scale factor errors assuming the errors are randomly distributed amongst different sensors. However, with the ±0.15°C scale factor error over the full range combined with the other effects discussed above, increasing the number of sensors has a negligible effect on the temperature sensor scale factor error component in the temperature coefficient uncertainty. However, it will help to determine the true back sheet temperature more accurately. This will be elaborated further in the sensitivity analysis in 5.4.

5.3.4 Uncertainty of P_{max} Temperature Coefficients: Simulation Results

In previous sections, 5 components affecting the P_{max} temperature coefficient are identified: 1. Repeatability of the P_{max} measurement; 2. Repeatability of the temperature measurement; 3. The temperature induced change in spectral mismatch; 4. Uncertainty on the monitor cell temperature coefficient; 5. Scale factor errors in the temperature sensors. These components are summarized in Table 14 and used as an input for the Monte Carlo simulation described in section 5.3.1.

Table 14: Summary of uncertainty components used as an input for the Monte Carlo Simulation

Summary of the inputs for Monte Carlo simulation	
Repeatability – P_{MAX}	▪ Normal distribution centered on 0, with standard deviation 0.15% of P_{MAX}
Repeatability – Temperature measurement	▪ Normal distribution centered on 0 with standard deviation 0.01°C
Temperature effect on Spectral Mismatch	▪ Normal distribution centered on -0.00957%/°C, with 0.00266%/°C standard deviation
Monitor cell temperature correction	▪ Rectangular distribution centered on 0, with limits at ± 0.008%/°C, assuming a 0.04% temperature coefficient
Temperature sensor scale effect error	▪ Rectangular distribution centered on 0 with limits at ± 0.15°C
"True" temperatures	▪ Vector with 6 temperatures [°C] ▪ [10,15,25,50,75,85]
"True" P_{MAX}	▪ Vector with 6 P_{MAX} values [°C] ▪ [318 312 300 270 240 228]

The simulation is iterated for 10000 runs and for each iteration the absolute temperature coefficient is determined using other draws from the input uncertainty distributions on the baseline data. The result is a set of 10000 Power-Temperature vectors, to which linear least square fits are applied. These fits can be described by the slope (the absolute temperature coefficient) and the intercept with the vertical (P_{max}) axis. These values are stored, a visualisation of the first 100 values is shown in Figure 51. For comparison, the "true" temperature coefficient (thus without any measurement errors) is plotted as a dashed green line. The temperature coefficients returned from the simulation are biased, overestimating the temperature coefficient (in absolute terms). This is most likely a result of the shift in spectral response, as this effect is the only effect which is biased instead of averaged at 0. This means that when a temperature coefficient is measured with the TCLF, it is likely to be overestimated (in absolute terms) compared to the "true" temperature coefficient.

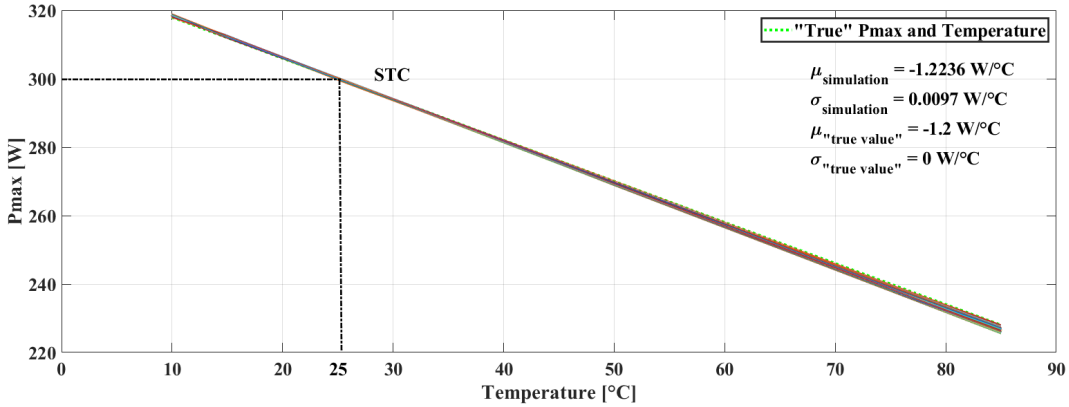

Figure 51: P_{max} versus temperature for the first 100 iterations of the Monte Carlo simulation.

Figure 52 shows the distribution of the simulated absolute temperature coefficients in histogram form. The shape of the histogram is approaching the shape of a Gaussian distribution. The bias is much more visible in this form, with the ”True” temperature coefficient far outside the 95% confidence interval. A mean absolute temperature coefficient of -1.2236W/°C is obtained, with a standard deviation of 0.0097W/°C, or in normalized form, a (k=1) relative standard deviation of 0.79%. This would implicate that, when not including the additional uncertainty as a result of the bias (or correcting for the MM-related bias), the absolute temperature coefficient would have a (k=2) standard uncertainty of 1.58%. However, since no correction is applied for this bias in practice, the uncertainty caused by this bias should be accounted for and the 2σ deviation furthest from the ”true” absolute temperature coefficient should be used to report the uncertainty on the measured absolute temperature coefficients. The 2σ furthest from the ”true” absolute temperature coefficient is located at -1.2430W/°C, so 0.0426W/°C from the ”true” value. The k = 2 relative standard uncertainty is now estimated at 0.0430/1.243*100% = 3.46%.

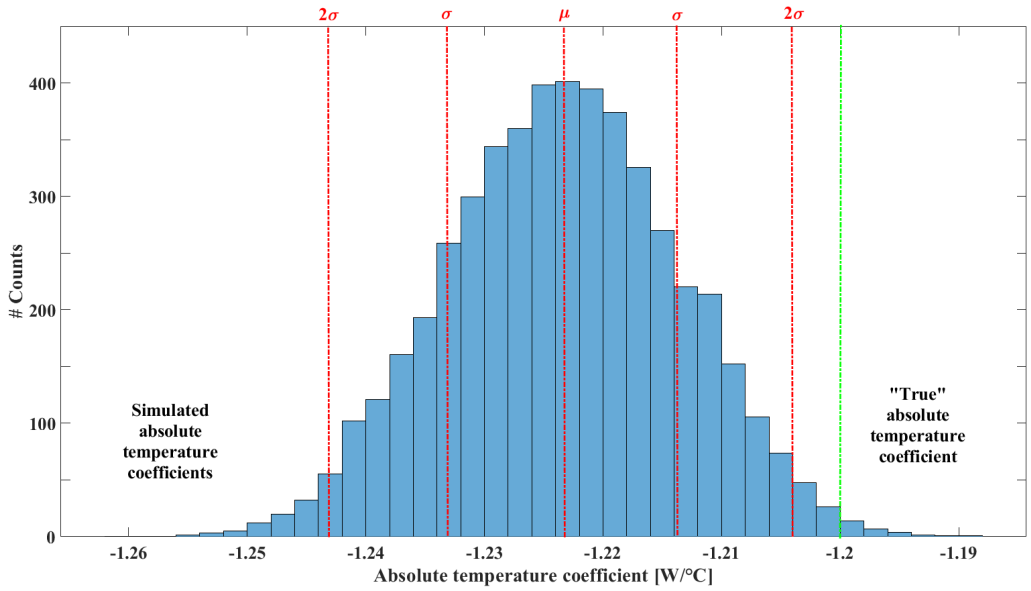

Figure 52: P_{max} temperature coefficients: Histogram of the absolute temperature coefficients resulting from 10000 iterations of the Monte Carlo simulation

For many readers, the relative temperature coefficient might be more commonly known, as it is generally mentioned on the specification sheets. This coefficient is determined by normalizing the slope by the

STC value of the parameter. This is done for the simulation results in Figure 53.

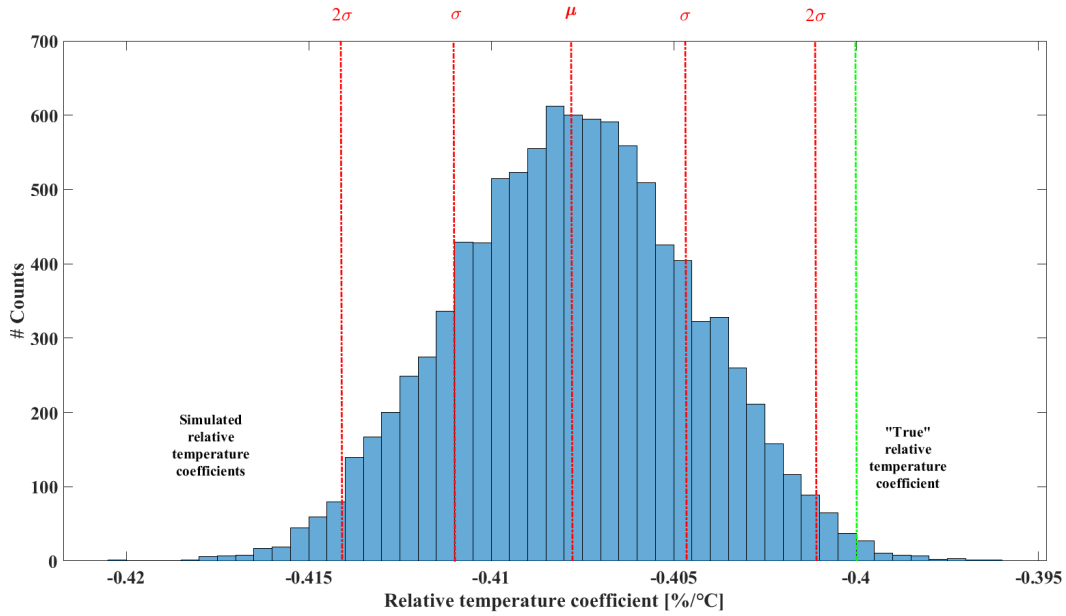

Figure 53: P_{max} temperature coefficients: Histogram of the relative temperature coefficients resulting from 10000 iterations of the Monte Carlo simulation

In contrast to the absolute temperature coefficient, any uncertainties in the STC measurement (e.g. simulator calibration) will affect the relative temperature coefficient. The uncertainty of the relative temperature coefficient can be determined by combining the uncertainty of the absolute temperature coefficient and the uncertainty in STC value (2.1%, k=2, section 5.3.2) through addition in quadrature. This results in an uncertainty for the relative temperature coefficient of 4.05% for c-Si modules, measured on the TCLF calibrated with a spectrally matched reference module (or alternatively WPVS reference cell). The results are summarized in Table 15

Table 15: Summary of the results on the P_{max} temperature coefficients measured with the temperature coefficient lab flasher

Parameter	**Simulated Result**	**k = 2 expanded Uncertainty**
Absolute temperature coefficient mean	-1.2236 W/°C	3.46%
Absolute temperature coefficient standard deviation	0.0097 W/°C	
Relative temperature coefficient mean	-0.4078 %/°C	3.46% - excluding STC uncertainty
Relative temperature coefficient standard deviation	0.0032 %/°C	
“True” absolute temperature coefficient	-1.2 W/°C	-
“True” relative temperature coefficient	-0.4 W/°C	
STC P_{MAX} uncertainty	-	2.1%
Combined uncertainty of the relative P_{MAX} temperature coefficient	**-**	**4.05%**

5.4 Sensitivity analysis

The results presented in section 5.3.4 are estimations where the measurement conditions can be properly controlled. This degree of control however, can not always be achieved in practice. Also, the inputs

are partly based on estimations and approximations which are not always possible to validate. To see the effect of such less controlled testing conditions or changes in other input parameters, the input parameters for the model are systematically varied. The seed of the random number generator is set to 0, so that each time the same "random" errors are drawn from the probability distributions in the model. This allows for comparability of the results when changing individual parameters.

First the final result for the developed setup, presented in section 5.3.4, is decomposed by systematically turning inputs on and off. The uncertainty budget is shown in Figure 54. The main contributors for the relative P_{max} temperature coefficient are the temperature induced spectral mismatch, the STC uncertainty and the monitor cell temperature coefficient. Repeatability effects are limited as these are both small in magnitude and affect each power and temperature point individually and in random direction, possibly cancelling out (part of) the effect on the temperature coefficient.

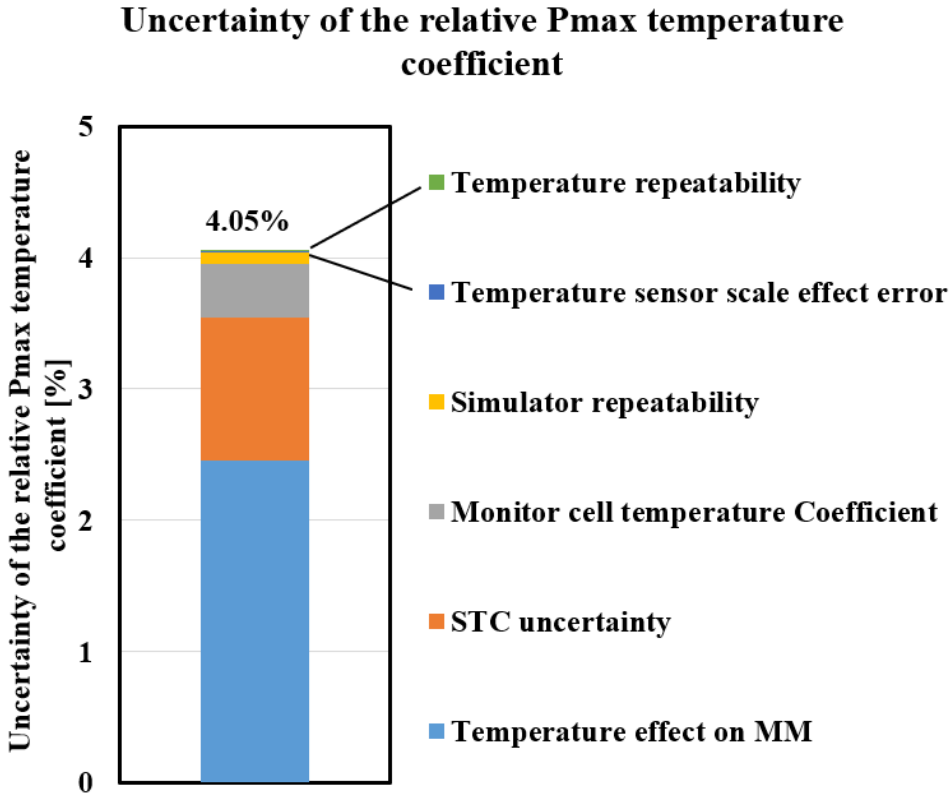

Figure 54: Uncertainty of the estimated relative P_{max} temperature coefficient

Now the model is adapted for four additional scenarios. In the second scenario ("Large T-MM effect"), the temperature effect on MM is changed to the largest value in Figure 48. In the standard scenario an average out of 5 cells is used for a more general application, however for some cells/modules this estimation might be over- or under-conservative. Besides MM, the other inputs remain constant. The third scenario ("40% MC Tempco uncertainty") is related to the uncertainty in the monitor cell temperature coefficient. In the standard scenario, this is estimated at 20%. Their is currently no better method to determine this uncertainty than expert judgement. These judgements are based on comparative measurements and analysis of long-term measurement data provided by PV module manufacturers using measurement setups from Eternalsun Spire. In the third scenario, this uncertainty is increased to 40% to visualize the effects of an incorrect determination. In the fourth scenario ("3% STC uncertainty"), less ideal STC circumstances are assumed. A reference cell or module is in practice never perfectly spectrally matched and sometimes no SR data of the DUT is available. Such inability to perform spectral mismatch corrections will increase STC uncertainty significantly. Finally, the fifth scenario ("1°C Temp.

scale factor error") covers the effect of scale-factor errors of the T-Type thermocouples for a worst case scenario, based on manufacturer specifications. The results are shown in Figure 55.

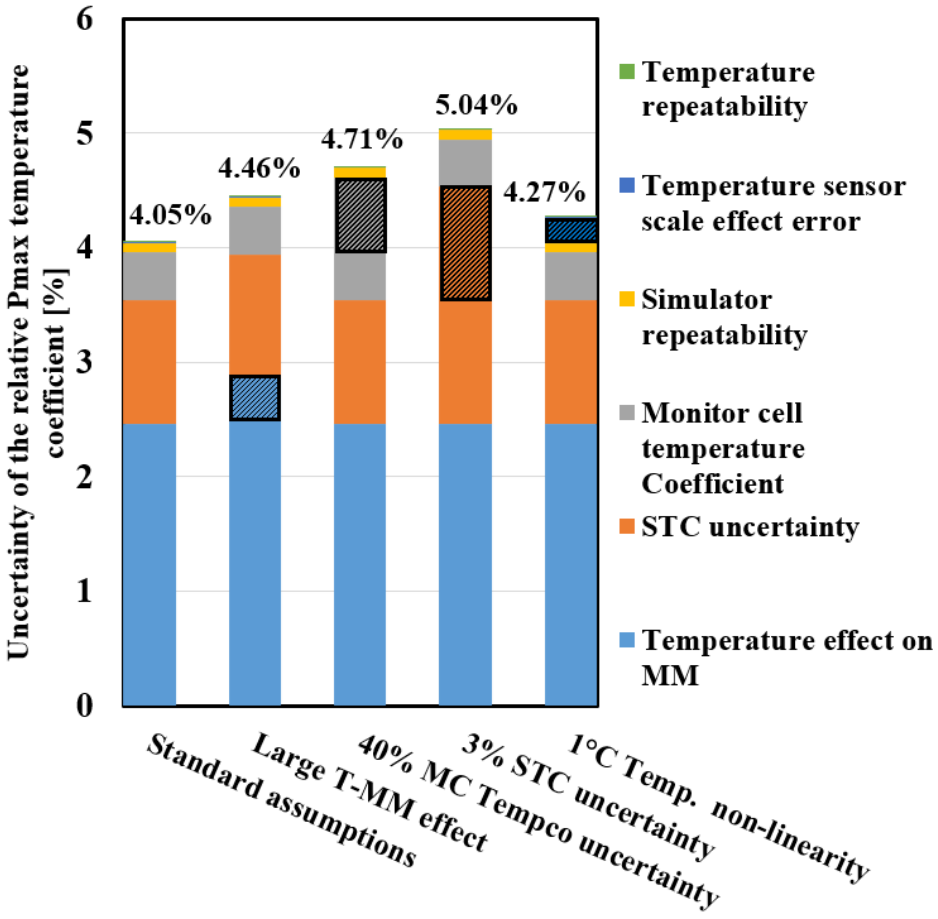

Figure 55: Uncertainty of the estimated relative P_{max} temperature coefficient for 5 different scenarios presented in section 5.4

Comparing the "Large T-MM effect" with the standard scenario from Figure 55, using the extreme temperature induced MM instead of the average value increases the estimated uncertainty by approximately 0.4%. Larger impact on the uncertainty is observed when considering a larger, more conservative monitor cell temperature coefficient uncertainty. Considering less ideal STC measurement conditions will also significantly increase the uncertainty of the relative P_{max} temperature coefficient. Finally, scale factor errors of the temperature sensors in a worst-case scenario only increases the uncertainty by 0.22%, thus a more detailed uncertainty estimation of this component will only have limited effects.

5.5 Temperature coefficient measurement uncertainties in industry practice

This subsection will elaborate on some measurement uncertainties currently observed in industry practice. First section 5.5.1 will discuss the implications of temperature coefficient non-linearity on the measurement accuracy of the temperature coefficient. Then 5.5.2 shows the possible effects of temperature non-equilibrium on the measurement results. Finally 5.5.3 shows how differences in simulator spectra can affect the temperature coefficient measurement.

5.5.1 Non-linearity of Silicon Heterojunction Technologies

As shown in Section 4, performance of Silicon Heterojunction (SHJ) based PV modules can be non-linear with temperature. IEC standards define module requirements to be considered linear. For linearity with temperature, sufficient linearity of V_{oc} and I_{sc} is required. The non-linearity in performance of SHJ modules is a fill factor effect however, which is not treated in IEC60904-10. As the V_{oc} and I_{sc} meet the linearity requirements, these modules can be considered linear. Because of this, the norms methods to determine temperature coefficients (Section 2.3.2) are valid for SHJ based modules as well. According to IEC 60891, temperature coefficients must be determined over the temperature range of interest, with 5°C intervals over a range of at least 30 °C. The measurement results from one of the SHJ modules are used to investigate the effect of the P_{max} non-linearity with temperature on the temperature coefficient uncertainty.

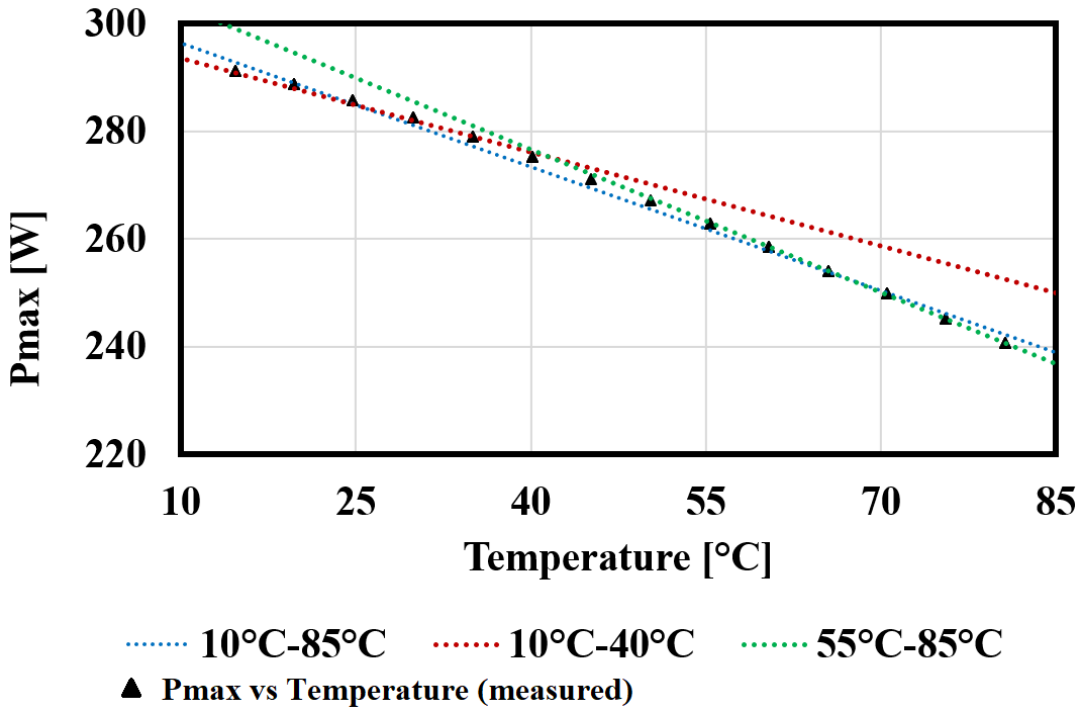

Figure 56: P_{max} versus temperature for a Silicon Heterojunction module. The triangles indicate the actual measurements, the dotted lines show the (extrapolated) linear fits for 3 ranges of interest: 10°C - 40°C (red); 55°C - 85°C (green) and 10°C - 85°C (blue)

Figure 56 shows the P_{max} versus module temperature from the selected SHJ module. Three linear trends are drawn, based on the linear fit on Power-Temperature data ranging from 1: 10°C to 40°C (red); 2: 55°C - 85°C (green); 3: 10°C - 85°C (blue). As can be seen, the temperature coefficient will vary significantly depending on the temperature range selected for the measurement or the linear fit. Relative P_{max} temperature coefficients for 5 different temperature ranges are calculated and shown in Table 16. All these temperature ranges are allowed according to the IEC procedures for temperature coefficient measurements. It is clear that much more than for other c-Si technologies (where P_{max} changes approximately linear with temperature), the temperature coefficient of SHJ modules can be highly dependent on the temperature range over which it is measured, with deviations up to 50% even when measured using the same setup. Neglecting this effect has large effects on the measurement uncertainty of the P_{max} temperature coefficient and will also increase uncertainty of the energy yield estimation.

Table 16: Relative P_{max} temperature coefficients for a commercial Silicon Heterojunction module using 5 different temperature ranges for fitting

Temperature range [°C]	Description	P_{MAX} Temperature Coefficient [%/°C]
10 - 85	Full range of TCLF	-0.270
10 - 40	Lowest possible 30°C range with TCLF	-0.204
25 - 55	STC and 30°C up	-0.264
55 - 85	Highest possible 30°C range with TCLF	-0.305
15 - 75	Range of the IEC Energy Matrix	-0.269

5.5.2 Natural Cooldown (”Hot potato”) method

In section 2.3.1 the natural cooldown (”Hot potato”) method is explained, which is commonly used to determine temperature coefficients of PV modules. Summarized, the module is heated in an oven or climatic chamber, taken out, placed on a solar simulator and then illuminated IV measurements are done while the module cools down to ambient temperature. As this procedure can also be performed on the developed temperature coefficient setup by opening the temperature chamber at high temperature, an accurate comparison can be made between the ”Hot Potato” and the ”Temperature chamber method” method (also ”Oven” method in section 2.3.1).

First the ”Temperature chamber” method is performed. The test-equipment is calibrated and a c-Si module is placed and heated until the module temperature is stable at 75°C. IV measurements are then obtained at module temperatures of 75°C, 65°C, 55°C, 45°C, 35°C and 25°C, with the module in thermal equilibrium at each temperature setpoint. After the module test with the ”Temperature chamber” method is completed, the module is heated to a module temperature of 85°C. The chamber is then opened up, exposing the module to ambient air and IV measurements with a 30 second flash-to-flash interval are done while the module cools down to ambient temperature.

The measured module parameters using both methods are summarized in Figure 57 and Table 17. As a result of the hot module exposed to the colder (approximately 25°C) ambient air, a temperature gradient is present between the inside and the outside of the module and there is no thermal equilibrium. This gradient is a function of the module temperature and the (ambient) air temperature [53]. The ”Hot Potato” method is likely to underestimate the true cell temperature, which is in agreement with expectations as the module is cooled from the outside while IV measurements are done. As the temperature gradient increases with a higher difference between in- and outside module temperature, the slope, thus the absolute temperature coefficients of the PV module parameters are not the same for the two methods. The hot-potato method thus adds a one-sided, scale-effect error which significantly affects the results.

Table 17: Relative temperature coefficients of a c-Si PV module measured using the ”Hot Potato” procedure and the Temperature chamber procedure on the same solar simulator

Relative temperature coefficient	Hot potato method	Temperature chamber method
P_{MAX} [%/°C]	-0.410	-0.380
FF [%/°C]	-0.168	-0.152
V_{OC} [%/°C]	-0.300	-0.276
I_{SC} [%/°C]	0.039	0.034

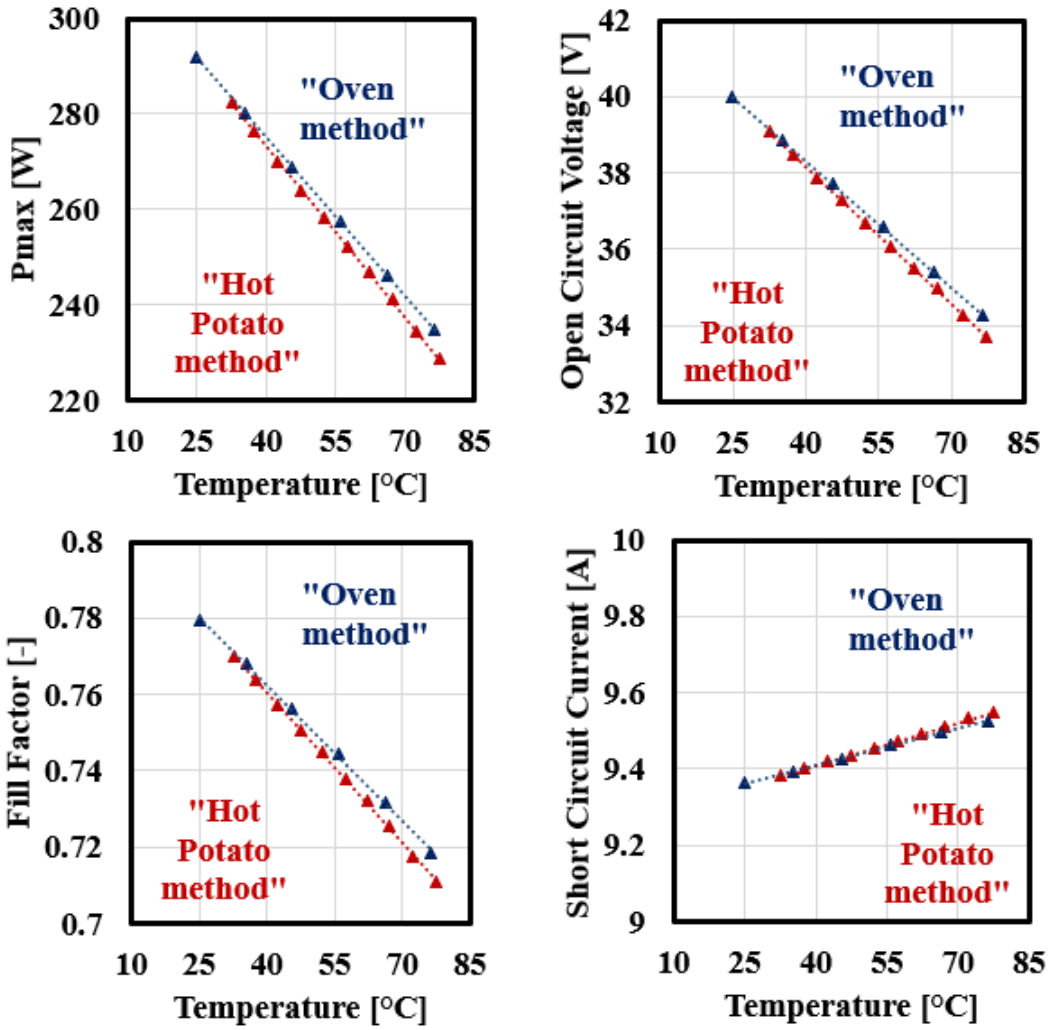

Figure 57: PV module parameters at various temperatures using the same solar simulator and two different temperature control methods: the ”Temperature chamber” method with the PV module in thermal equilibrium and the ”Hot Potato” method without thermal equilibrium

The magnitude of this effect is determined using the V_{oc} value (proportional to the cell temperature) as an ”internal” temperature sensor. Based on the V_{oc} measurements and the V_{oc} temperature coefficient obtained using the (more accurate) ”Temperature chamber” method, the internal temperature during the ”Hot Potato” method is determined and compared with the temperatures measured by the thermal sensors in Figure 58. As can be seen, especially for high module temperatures, the internal temperature is severely underestimated when using the ”Hot Potato” method. With decreasing temperatures, the temperature gradient, thus the junction-to-back temperature difference decreases and at ambient temperatures the difference is negligible.

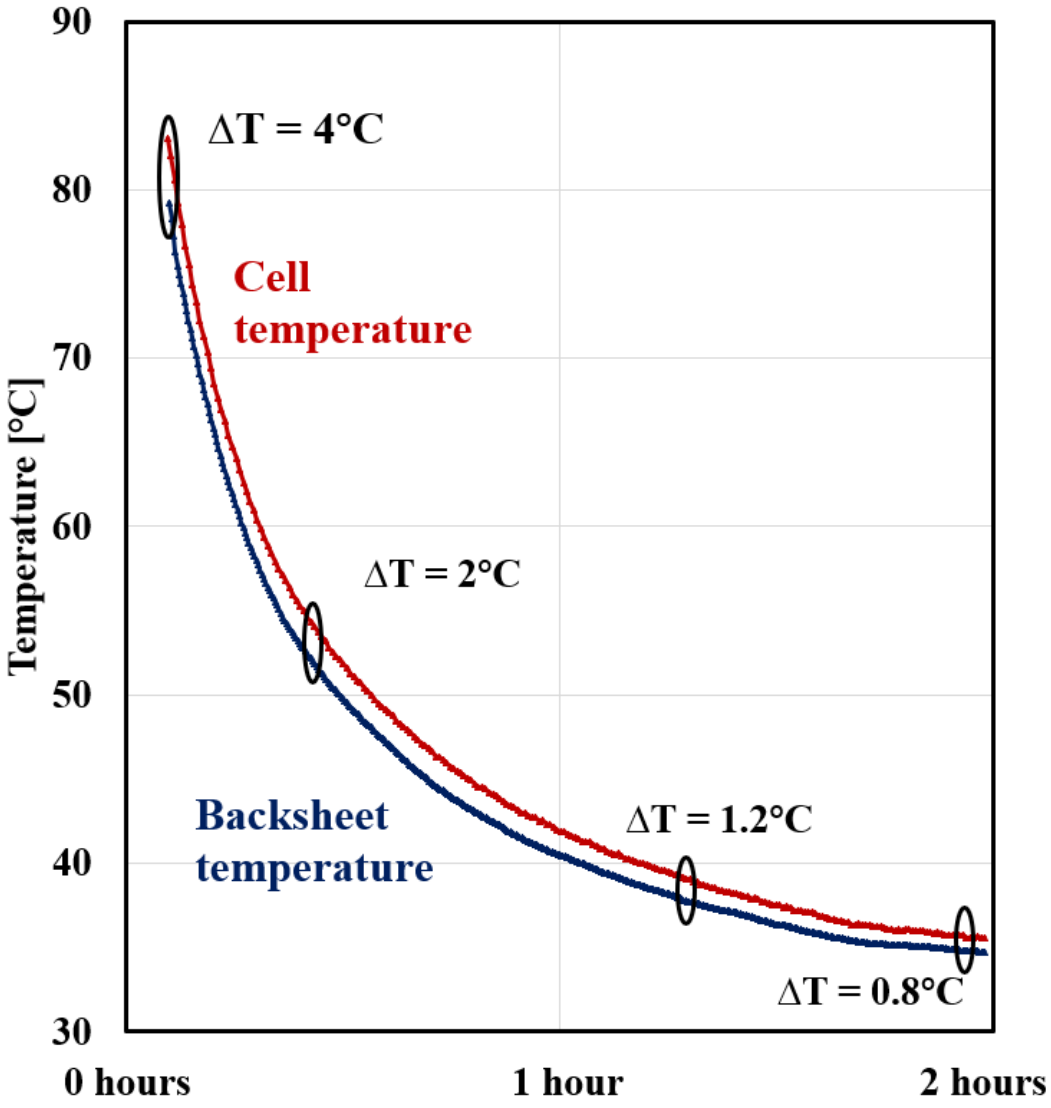

Figure 58: Backsheet temperature and cell temperature of a c-Si PV module while cooling down from 85 to ambient temperature in horizontal orientation. The backsheet temperature is determined from the average of 9 thermocouples placed on the backsheet, the cell temperature is calculated from the module V_{oc} and the temperature coefficient obtained using the Temperature chamber method.

This error in determination of the true cell temperature, typical for the ”Hot potato” method, is likely a significant contributor to observed differences in temperature coefficients reported in industry, as this method is known to be widely applied. Even with the same simulator, calibration and module, the relative difference from measuring the P_{max} temperature coefficient with the ”Temperature chamber” method and the ”Hot-potato” method is already 7%.

5.5.3 Effect of the simulator spectrum on the short-circuit temperature coefficient

As discussed in section 5.3.3, the spectrum of the solar simulator can have significant impact on the temperature coefficient. The effect of simulator spectrum is the largest for the I_{sc} temperature coefficient which is directly dependent on the simulator spectrum, however it is also directly affecting I_{mpp} and thus P_{max}.

To study this effect, a c-Si DUT is tested using the TCLF and a continuous solar simulator with tempera-

ture control capabilities. Even though this continuous simulator is not optimized for temperature coefficient measurements, it will be interesting for comparison as the spectrum in the wavelength region where the temperature induced shift in SR occurs is quite different from the TCLF spectrum. As the continuous solar simulator was still under construction, it was not absolutely calibrated and no reference irradiance was measured yet. From the construction of similar simulators, the uncalibrated irradiance is known to be in the range of $900W/m^2$ and $1100W/m^2$, however the exact value was not known. To compensate for the difference in irradiance of the TCLF and the continuous solar simulator, I_{sc} and P_{max} values measured with the continuous solar simulator are corrected by the ratio $I_{sc-TCLF}/I_{sc-continuous-sim}$ at 25°C. V_{oc} values are uncorrected. $I_{sc-TCLF}$ was obtained with the TCLF calibrated to $1000W/m^2$, so this correction can be seen as an irradiance correction of the continuous solar simulator measurements to $1000W/m^2$. The effect of this difference in irradiance on temperature coefficient is assumed to be negligible [54]. The maximum temperature non-uniformity on the backsheet of the DUT is $\pm$ 3°C under illumination and the DUT is oriented vertically (similar orientation as the module in Figure 11 in section 2.3.1). Uniformity, spectrum and stability are all rated A+ according to IEC60904-9 ed.3.

The results in Figure 59 show that even two high-end solar simulators with temperature control capabilities are used, P_{max} temperature coefficients can already show 5% relative deviations. The temperature dependency of the V_{oc} is almost similar, however the V_{oc} measured with the continuous solar simulator is consistently lower compared to the developed setup (TCLF) at the same temperature. This is the result of a junction-to-back error, as the continuous solar simulator is heating the inside of the DUT and cold air forced past the outside of the DUT to cool the DUT to desired temperature. As a result, the temperature measured on the back of the DUT, while using the continuous solar simulator, is below the average cell temperature of the DUT so that a lower V_{oc} is measured. In practice this offset can be corrected for. Differences in V_{oc} are about 1.2%, with a V_{oc} temperature coefficient of approximately 0.3%/°C this would indicate a 4°C back to junction difference in the continuous solar simulator, assuming the TCLF obtains full equilibrium between cell and rear surface temperature. The difference in I_{sc} temperature coefficient is relatively high, which is likely caused by the difference in simulator spectra.

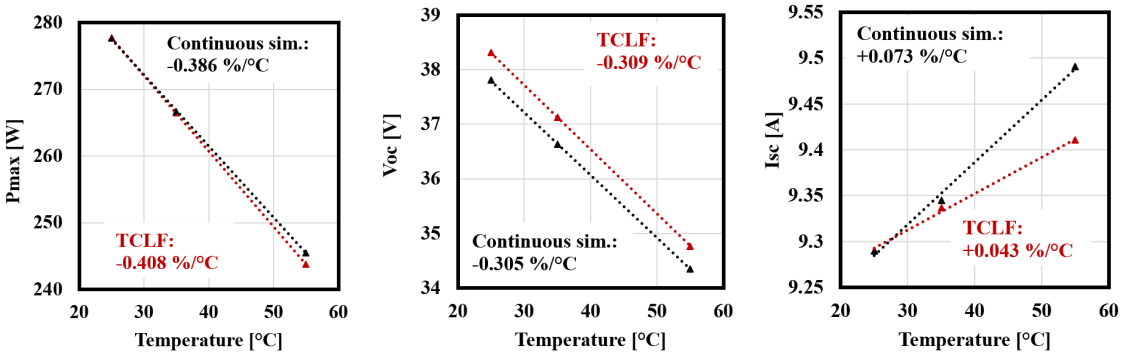

Figure 59: Comparison of an Al-BSF PV module, tested with a continuous solar simulator and with the temperature coefficient setup both developed by Eternalsun Spire. Black: results from the continuous solar simulator, Red: results from the temperature coefficient setup

The large difference in I_{sc} temperature coefficient is expected to be a result of the difference in simulator illumination spectra. Figure 46 in Section 5.3.3 shows that an increase in temperature of a c-Si cell results in an increased response between 900nm and 1200nm. Figure 60 shows the spectra of both the TCLF and the continuous solar simulator. Here it can be seen that especially in the region from 900nm to 1200nm, the continuous simulator has more light compared to both the AM1.5G reference spectrum and the TCLF spectrum.

Figure 60: Measured spectra of the Temperature Controlled Lab Flasher (TCLF) and the Continuous solar simulator compared to the AM1.5G reference spectrum (removed for public manuscript)

In theory J_{sc}, thus also I_{sc} can be calculated from Equation 6. The EQE's at 10°C and 60°C (obtained from the spectral response) of the c-Si cell in Figure 46 are used as input, with the photon flux $\phi(\lambda)$ as produced by the TCLF, the continuous solar simulator and the AM1.5G spectrum. The theoretical temperature coefficient can then be calculated by dividing the difference in I_{sc} by the difference in temperature (50°C). Note that the absolute I_{sc} depends on solar simulator calibration and spectrum. For comparability, the I_{sc} values measured by the simulators are scaled so that the I_{sc} at 20°C is equal to I_{sc} at 20°for the AM1.5G spectrum. This is the same as the irradiance- and spectral mismatch correction commonly performed at STC, however since no spectral response data at 25°C was available, data at 20°C is used.

Table 18: Theoretical I_{sc} temperature coefficient, based on measured simulator spectra and c-Si spectral response at 10°C and 60°C presented in Figure 46. More light in the low-energy wavelengths increases the I_{sc} temperature coefficient. Note that the temperature coefficient measurements are based on a c-Si module measured in-house and the EQE values are obtained from measurements in literature. While both c-Si technology, the degree of similarity of both spectra is not known

	Spectrum		
	Continuous simulator	**TCLF**	**AM1.5G**
I_{SC} @ 10°C [A]	9.15	9.19	9.17
I_{SC} @ 60°C [A]	9.49	9.35	9.39
I_{SC} Temperature Coefficient based on EQE [%/°C]	0.074	0.035	0.047
I_{SC} Temperature Coefficient based on measurements [%/°C]	0.073	0.043	n/a

This comparison shows that the I_{sc} coefficient is both in theory and practice highly dependent on the spectrum used for the measurement and for the continuous solar simulator there is a high level of agreement between the measured and calculated temperature coefficient. This is to be expected since the spectrum of the continuous solar simulator in the wavelength range where the shift in spectral response occurs is pretty constant. For the temperature coefficient setup there is quite a difference between the theoretical and the measured temperature coefficient. This could be caused by several components: 1. the temperature coefficient of the monitor cell integrated in the TCLF might be not fully correct (with an estimated relative error of 20%, this could explain 0.03A difference, which is approximately equal to the deviation between the measured and calculated temperature coefficient as discussed in section 5.3.3); 2: the used spectral response to calculate the temperature coefficient is not fully representative for the tested module and some irradiance peak (or drop) of the TCLF is affecting the I_{sc} calculated result. The spectrum of the continuous solar simulator is approximately constant in the range where the spectral shift occurs, thus the temperature coefficient measured with the continuous solar simulator is less affected by the exact wavelength range of the spectral shift.

5.5.4 Temperature sensors and temperature non-uniformity

While the IEC60891 describes to use (at least) 4 thermal sensors when measuring temperature coefficients, this amount is not always sufficient [55]. This mainly depends on the magnitude and distribution of the PV module temperature non-uniformity. A high number of sensors will generally give a better representation of the true average temperature of the module (rear) surface. To estimate the effect of the amount of temperature sensors in the TCLF, average temperatures from a 4- and 9-sensor configuration

are compared from data obtained during a typical temperature coefficient run. The 9-sensor configuration is placed in 3x3 formation as presented in section 3. The 4-sensor configuration is using the same sensors, however only data from the IEC60891 locations is used to determine the average temperature.

Table 19: Comparison of using 4 (IEC recommended) or 9 temperature sensors during a typical temperature coefficient run

Tair [°C]	**85**	**75**	**65**	**55**	**45**	**35**	**25**	**15**
Tmodule - 9 sensors [°C]	87.33	76.54	66.23	55.92	45.63	35.28	24.92	14.78
Tmodule - 4 (IEC) sensors [°C]	87.37	76.59	66.29	55.98	45.68	35.31	24.93	14.72
Difference: 4 vs 9 sensors in the TCLF [°C]	-0.04	-0.05	-0.06	-0.06	-0.04	-0.03	-0.01	0.06

In table 19 the averages from 4 and 9 sensors are compared for a 60 cell module in the TCLF. As a result of the low temperature non-uniformity, there is little difference between using the 4 IEC positions or using 9 additional temperature sensors for a standard 60-cell module in the TCLF. Effects on the temperature coefficient are below 0.1% thus can be considered negligible for this setup. It is more important in industry practice however, as accurate temperature control is not always available.

6 Discussion and Conclusion

6.1 Discussion

The measurement uncertainty for relative P_{max} temperature coefficients measured with the temperature coefficient lab flasher (TCLF) is estimated to be 4.05%. This estimation was done assuming a 60 cell c-Si device under test (DUT) and a spectrally matched reference module used for calibration, the latter can be considered close to optimal conditions for achieving a low measurement uncertainty. The TCLF is a useful tool to decrease measurement uncertainty for temperature coefficients, compared to existing methods in the PV industry. This improves accuracy of PV energy yield modelling and thus reduces financial risk.

This work is, to the writers knowledge, the second uncertainty analysis applied to a setup designed to measure temperature coefficients. The investigated setup in this work could be the first investigated commercially available setup which is specifically designed to measure temperature coefficients with low measurement uncertainty. In comparison with the other analysis [42], the estimated uncertainty in section 5.3.4 is approximately 1% to 3% higher. This is possibly caused by a different implementation of the uncertainty component resulting from the temperature induced change in spectral response of PV devices. Since in [42] a larger number of setups is investigated, the uncertainty component accounting for this (temperature induced) change in spectral response is considered symmetrical around 0. This consideration is made because a single estimation is made for all the different setups and their spectra were not all known. As a result of this generalisation, this uncertainty component, which could be strongly biased for specific solar simulators, is not so prominent in [42]. The estimated TCLF uncertainty is, however, lower compared to the $\pm 10\%$ uncertainties observed in practice [25][8]. Additionally, this work improves understanding on some uncertainty drivers observed in the PV industry. A large decrease in measurement accuracy is shown compared to the "Hot Potato" method which is widely applied in PV industry.
Furthermore, particularly relevant for SHJ modules, non-linear behaviour with temperature is found, which can result in significant errors in determination of the temperature coefficient when neglected. Based on these and other results showing similar non-linearity [37],[56], a note is suggested for the upcoming revision of the IEC60981 norm, which provides the procedure for measuring temperature coefficients.
The effect of the simulator spectrum on the temperature coefficient is elaborated from a theoretical background, substantiated with practical experiments. The interaction between simulator spectrum and temperature induced change in spectral response (SR) turns out to be a large uncertainty component setups involving solar simulators and could explain a significant part of the measurement deviations observed in literature [8]. The magnitudes of the estimated MM results are in agreement with results obtained in a recently published paper on temperature dependent SR [52]. The presented experiments and results in section 5.5 can support the PV industry in understanding and mitigating measurement errors currently occurring in practice.

The measurement results in section 4 and the experiments from section 5.5 are obtained using standard procedures, on a solar simulator that is proven to be accurate in the field. The uncertainty value is estimated using a Monte Carlo method, combining different uncertainty components. This model is a relatively straightforward application of the GUM supplement 1 on Monte Carlo analyses. The relation between the output and input values was generally known and no complex transformations are involved in the model. The accuracy of the model will be determined by the accuracy of the model inputs: 1. The temperature induced change in spectral mismatch (MM); 2. The temperature coefficient of the monitor cell; 3. The scale factor error of the thermal sensors; 4. The repeatability of the IV and temperature measurements.

1. A major contributor the temperature coefficient measurement uncertainty is the temperature induced change in MM. The average and standard deviation of this effect are based on literature-available measurements on 5 different PV modules and cells [52]. The simulation input value MM is based on the average of these 5 samples. With only 5 samples, the standard deviation of approximately 25% is large and shows that emission peaks in the simulator spectrum have significant impact on the temperature induced MM. As a result, this component is highly dependent on cell technology. It would be recommended to collect more data and confirm if this effect can vary even more for different module types or is in the currently estimated orders of magnitude.

Instead of expanding the estimated uncertainty (as done in the simulation), the combined uncertainty could be reduced significantly when a correction for the temperature change in MM would be applied. Labs could for example implement Peltier heating elements to adapt their existing SR measurement setup for SR measurements at elevated temperatures. A more economical alternative is suggested in aforementioned work [52]. Here it is found that correcting measurements for MM based on an average shift of the SR with temperature (0.45nm/K) in the high-wavelength (>900nm) region significantly improved results compared to uncorrected measurements. More research is advisable, but a recommendation is to at least mention the existence of the temperature effect on MM in the IEC standards, in particular the standards discussing temperature coefficients and/or spectral measurements.

2. The monitor cell temperature coefficient is another significant input for the model, as any error in here is proportional to temperature and thus has a direct effect on the temperature coefficient through irradiance and thus currents. The magnitude of this uncertainty component is based on expert estimation: measurements by Eternalsun Spire employees who determine this coefficient for each machine individually. However, these monitor cells are normally operating below 35°C, thus below operating temperatures in the TCLF. It is possible that the uncertainty for the temperature coefficient is underestimated because of this small operating range.

An alternative procedure to determine the monitor cell temperature coefficient is developed, however still needs to be thoroughly evaluated in practice. First, a PV module (preferably a reference module with calibrated/well known I_{sc} value) is placed in the temperature chamber, the chamber is set to 25°C (STC) and the monitor cell temperature correction is turned off. When the module has reached thermal equilibrium, the setup is calibrated to 1000W/m2. After calibration, an IV measurement is performed at 25°C. Then the chamber is opened, the module is taken out, the chamber is closed again and set to 85°C. As a result, the monitor cell (located in the solar simulator, not directly in the temperature chamber) will reach a temperature of approximately 65°C. Now the chamber is opened, the module is placed and an IV measurement is done right away. Because of the hot test surface, the module will heat up directly. However as the measurement is done seconds after the placement, the cell temperature is only slightly increased (which can be confirmed from the V_{oc} measurement). During this IV measurement, the monitor cell is still approximately 65°C due to the thermal inertia of the solar simulator and the air inside. The result is an I_{sc} of the same module, with a monitor cell temperature of 25°C and 65°C. As the irradiance is controlled based on the I_{sc} of the monitor cell (which is not temperature corrected), the irradiance and thus module I_{sc} will be lower. From this difference the required temperature correction and thus the monitor cell temperature coefficient can be calculated.

An second alternative is to apply optical filters on the monitor cells. Low-pass optical filters, such as KG3 or KG5 filters, will block almost all the light in the IR part of the light incident on the monitor cell. As the SR below $\sim$ 900nm hardly changes with temperature [52], and the shift in SR after $\sim$900nm accounts for almost the full effect of the I_{sc} temperature coefficient, the I_{sc} will remain constant with temperature. This would make these filtered monitor cells an interesting option for further reduction of the measurement uncertainty of the TCLF.

3. The temperature sensor scale factor error is estimated based on the worst temperature measurement

deviation from a single temperature sensor, compared to the average temperature of a set of 9 sensors. As the 9 sensors are all of the same brand, type and possibly the same production batch, production tolerances could have resulted in a temperature measurement deviation for the whole set of thermocouples. This would cause the estimation currently used in the model to be inaccurate. To mitigate this possibility, each thermocouple could be calibrated against a sensor with traceable calibration, supplied by an accredited institute. It has to be noted that the absolute magnitude of this effect is limited (as seen in Section 5.4).

4. Repeatability of the P_{max} and Temperature measurements are unlike the other uncertainty contributors based on statistical observations. These values are considered very well known as they are determined for each individual solar simulator and are well defined.

Various inputs for both the STC uncertainty estimation and the Monte Carlo simulation are based on expert judgement. While several crosschecks give high reason to believe these assumptions are reasonable for STC conditions, new assumptions are made to describe the temperature effects. It is recommended (and planned by Eternalsun Spire) to validate these approximations by (for example) round robin testing and direct comparisons with other setups, preferably designed to measure temperature coefficients with low uncertainty.

Finally, in section 4.4, data is presented supporting an alternative method to obtain temperature coefficients of PV modules as suggested in [6]. This could potentially be a simple, economical and accurate method to determine the performance PV modules at different temperatures than measured. As already discussed by the authors, more research is needed to confirm the applicability. Promising results are currently obtained for dark conditions and $1000W/m^2$ irradiance, but validity is yet to be confirmed for other irradiance levels. Additionally, deviations between the developed method and measurements are mentioned for SHJ technologies (confirmed in this work) and high efficiency back-contact PV modules, showing that the method can be less accurate for some technologies. Besides the practical limitations of the method, it is also important to consider that the suggested method is based on a mathematical derivation, combined with a general estimation of the nE_g product. There is no traceability to international standards, thus without an actual measurement it is hard to ensure that the method is valid for a specific module. This could limit the applicability of the method, since the traceability of measurement results is needed for accreditation of a PV lab. Such accreditation of a laboratory is often needed, since many (especially utility scale) customers require a 3rd party confirmation of the manufacturer datasheet values, which should be provided by an accredited laboratory, before doing a purchase [57]. The method could thus be a reasonable solution for labs that don't have the need for traceable measurements and are currently using less accurate techniques to determine the temperature coefficient. Therefore, it's applicability is in a somewhat different field compared to the TCLF developed by Eternal Sun, since the latter is developed to measure and validate results and evaluate such methods as developed in [6]. Additionally the TCLF is also designed for use with various PV technologies, whereas the method discussed above is limited to c-Si technology only.

6.2 Conclusion

A commercial setup designed to reduce measurement uncertainties in temperature coefficients is validated through practical experiments, backed up by a Monte Carlo based uncertainty analysis. The main uncertainty components for the developed setup are temperature-dependent spectral mismatch, the monitor cell temperature coefficient and STC uncertainty. The combined expanded (k=2) uncertainty for the developed setup is estimated to be 4.05% for the relative P_{max} temperature coefficient. Additionally, some uncertainty effects relevant for current industry are presented, such as non-linear performance of SHJ modules with temperature, effects of back to junction differences and the effects of solar sim-

ulator spectra. To reduce financial risk caused by measurement uncertainty of the P_{max} temperature coefficient, PV industry should be aware of the presented drivers when considering the equipment and procedure that will be used. This this work can help in this consideration.

A Uncertainty contributors: detailed descriptions and definitions

Signal (DAQ) - Reference Cell This component describes the uncertainty on the WPVS reference cell signal, thus between the connector of the WPVS reference device and the software. This includes the DAQ, cable and shunt resistor. Electrical calibration ensures accurate, traceable measurements. This electrical calibration can be done with a low uncertainty, therefore the uncertainty of the DAQ is often relatively low as well. In this specific application the component includes the shunt resistor as well.

Calibration I_{sc} - Reference cell The uncertainty of calibration of the reference device (a calibration module or WPVS reference cell) used for calibration. This is generally a PV device, of which the short-circuit current is measured to determine the illumination level. This PV device should be calibrated and its calibration should be traceable to a primary standard.

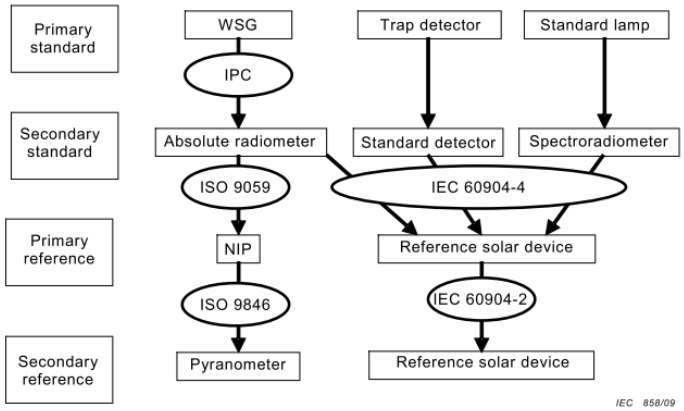

Figure 61: Calibration chain of PV reference devices. Figure: IEC60904-4

Figure 61 shows the calibration chain for PV reference devices as specified in IEC60904-4. More details on calibration methodology for primary and secondary standards can be found in [58][59][60]. The most relevant for this work however, is that reference solar devices are traceable either to SI units (through trap detectors and standard lamps) or the World Radiometric Reference, formed by a set of cavity radiometers held by the World Standardization Group (WSG). Each transfer down the calibration chain adds additional uncertainty, which should be defined and quantified as well as possible.

Primary reference devices are used by accredited solar laboratories and are restricted regarding size and technology. These primary references can be used to calibrate secondary reference devices, which can be both cells and modules. These are also referred to as golden references. Manufacturers or lower accredited PV laboratories will acquire such golden references, and use them to create working ("silver") references, used for regular system checks. When A or A+ solar simulators are used, calibration of the secondary reference device is often a large contributor to overall uncertainty. This is significantly smaller when a primary reference is used.

Drift - Calibration I_{sc} Long-term drift of the reference device used for calibration and/or irradiance measurement. Assuming correct handling (e.g. no damage on the reference device), the uncertainty as a result of drift is relatively low. These uncertainties levels are generally based on yearly re-calibrations of the same device, and it has to be noted that only a limited number of institutes have long-term data available and it is not always ease to distinguish drift as there are much more effects affecting calibration value.

Distance & orientation The intensity of the light incident on the device under test will be a function of the distance to the light source. Naturally, if the DUT is closer to the light source compared

to the reference cell, the irradiance measurement will not be representative. In the same way, the orientation can have effects. The response of a cell to perpendicular light might be slightly different from the response to light incident at an angle.

Spectral Mismatch The difference in spectral response between the reference device and the DUT, in combination with the deviation of the illumination source from the AM1.5g spectrum creates the need for a correction factor: the spectral mismatch factor. This is calculated by

$$MM = \frac{\int_a^b SR_{DUT}(\lambda)\phi_{meas}(\lambda)d\lambda}{\int_a^b SR_{DUT}(\lambda)\phi_{ref}(\lambda)d\lambda} \frac{\int_a^b SR_{ref}(\lambda)\phi_{ref}(\lambda)d\lambda}{\int_a^b SR_{ref}(\lambda)\phi_{meas}(\lambda)d\lambda} \tag{22}$$

With SR_{DUT} and SR_{ref} the spectral response of the DUT and Reference device, and ϕ_{DUT} and ϕ_{ref} the relative spectral irradiance of the solar simulator and the reference spectrum (for STC testing: AM1.5G) respectively.

The uncertainty in this correction factor is a result of the uncertainties in the cell and DUT spectral response, and the spectrum of the solar simulator. Determination of these components are a study on its own '[61]. The underlying components are wavelength dependent and the combined uncertainty is determined using a Monte Carlo approach.

Irradiance Non-uniformity - Reference Cell If the PV reference device (used for calibration and/or asolute irradiance measurement) is placed in a bright or dark spot, a bias error on the irradiance measurement will be introduced. Therefore the reference device is placed at a location with average irradiance. However, as the measurement of irradiance distribution and the placement of the cell are not exact, small errors can still occur. The uniformity is measured on a small area around the reference device, which should give the minimum and maximum bias error. This irradiance error is assigned a rectangular distribution, which is used for the final uncertainty.

Signal (DAQ) - IV Curve This component describes the uncertainty of the DAQ and measurement circuit used for the IV measurement. This is similar as the circuit for the irradiance measurement, however instead for the measurement of the module current and voltage.

Ohmic resistance Ohmic resistance before the four wire measurement point (such as adaptor cables) can introduce current dependent voltage drops. This will have no effect on current or V_{oc}, but can introduce a voltage shift of V_{mp} to the left affecting the P_{max}.

Hysteresis Hysteresis causes over or underestimation of the P_{max} depending on sweep direction, and is caused by dynamic effects in the cell during the IV measurement. During a forward (I_{sc} to V_{oc}) sweep, the applied bias voltage is increased step by step. With an increase of bias voltage, the charge distribution of the minority carriers in the bulk increases exponentially. Every time, then charge carriers have to redistribute to reach a new equilibrium distribution, which could be seen as charging of diffusion capacitance [45]. As these carriers are used for internal charging, they cannot contribute to the external cell current, and measured current will be underestimated until the equilibrium distribution is reached. This is particularly problematic for highly passivated modules with high carrier lifetimes and thus diffusion lengths as this capacitance is proportional to the diffusion length.

Irradiance non-uniformity The effect of irradiance non-uniformity on the IV curve is based on a simulation, where a model is made with a 6x10 cells 3 bypass diode module is tested with a $\pm 2\%$ typical non-uniformity profile. Based on this simulation and the 0.84% non-uniformity of the Fraunhofer setup, the uncertainty is estimated.

Temperature non-uniformity Here the maximum temperature non-uniformity of 1°C is multiplied by the temperature coefficient of current and voltage. These are combined and form the P_{max} uncertainty: this assumes the temperature that is measured is 1°different from the actual temperature.

References

[1] A. Smets, K. Jager, O. Isabella, R. v. Swaaij, and M. Zeman, *Solar energy: The physics and Engineering of Photovoltaic conversion technologies and systems*. Delft: UIT Cambridge, England, 1st ed., 2016.

[2] M. Derick, C. Rani, M. Rajesh, M. E. Farrag, Y. Wang, and K. Busawon, "An improved optimization technique for estimation of solar photovoltaic parameters," *Solar Energy*, vol. 157, no. November, pp. 116–124, 2017.

[3] D. Dirnberger, *Photovoltaic module measurement and characterization in the laboratory*. Elsevier Ltd., 2017.

[4] I. TC82, "IEC 61853-1 Irradiance and temperature performance measurements and power rating," 2011.

[5] J. Krügener and N. P. Harder, "Weak light performance of PERC, PERT and standard industrial solar cells," *Energy Procedia*, vol. 38, no. 0, pp. 108–113, 2013.

[6] Y. Hishikawa, T. Doi, M. Higa, K. Yamagoe, H. Ohshima, T. Takenouchi, and M. Yoshita, "Voltage-dependent temperature coefficient of the I-V curves of crystalline silicon photovoltaic modules," *IEEE Journal of Photovoltaics*, vol. 8, no. 1, pp. 48–53, 2018.

[7] D. Dirnberger and U. Kraling, "Uncertainty in PV Module Measurement—Part I: Calibration of Crystalline and Thin-Film Modules," *IEEE Journal of Photovoltaics*, vol. 3, pp. 1016–1026, 7 2013.

[8] Y. Yang, Y. Zhang, Q. Peng, Y. Chen, J. Feng, Z. Feng, P. Verlinden, P. Yang, and J. Chu, "Understanding the uncertainties in the measurement of temperature coefficients of si pv modules," in *29th European Photovoltaic Solar Energy Conference and Exhibition*, 2014.

[9] J. E. Mason, "World energy analysis: H2 now or later?," *Energy Policy*, vol. 35, no. 2, pp. 1315–1329, 2007.

[10] P. Netherlands Environmental Assessment Agency, "Insight into Energy Scenarios," no. September, 2019.

[11] D. Ansari, F. Holz, and H. Al-Kuhlani, "Energy Outlooks Compared: Global and Regional Insights," *Economics of Energy & Environmental Policy*, vol. 9, no. 1, 2020.

[12] S. Shafiee and E. Topal, "When will fossil fuel reserves be diminished?," *Energy Policy*, vol. 37, no. 1, pp. 181–189, 2009.

[13] US Department of Energy's Office of Electricity Delivery and Energy, "Economic benefits of increasing electric grid resilience to weather outages," Tech. Rep. August, US Department of Energy's office of Electricity Delivery and Energy, 2014.

[14] A. Berger and C. Tricot, "The greenhouse effect," *Surveys in Geophysics*, vol. 13, pp. 523–549, 11 1992.

[15] M. Allen, M. Babiker, Y. Chen, M. Taylor, P. Tschakert Australia, H. Waisman, R. Warren, P. Zhai, K. Zickfeld, P. Zhai, H.-o. Pörtner, D. Roberts, J. Skea, P. Shukla, A. Pirani, W. Moufouma-Okia, C. Péan, R. Pidcock, S. Connors, J. Matthews, Y. Chen, X. Zhou, M. Gomis, E. Lonnoy, T. Maycock, M. Tignor, and T. Waterfield, "IPCCC 1.5C: Summary for Policymakers," tech. rep., Intergovernmental Panel on Climate Change, 2018.

[16] S. N. Islam and J. Winkel, "Climate Change and Social Inequality*," 2017.

[17] International Renewable Energy Agency (IRENA), *Global Energy Transformation: A Roadmap to 2050*. 2018.

[18] IEA, "Snapshot of Global PV 1992-2014," 2015.

[19] N. Reich, E. Alsema, W. v. Sark, W. Turkenburg, and W. Sinke, "Greenhouse gas emissions associated with photovoltaic electricity from crystalline silicon modules under various energy supply options N.H.," *Progress in photovoltaics: research and applications*, vol. 19, no. January 2011, pp. 603–613, 2011.

[20] K. Komoto and J. S. Lee, "End-of-Life Management of Photovoltaic Panels: Trends in PV Module Recycling Technologies," tech. rep., International Energy Agency, 2018.

[21] D. Stolten and V. Scherer, *Transition to Renewable Energy Systems*. Wiley-VCH, 2013.

[22] A. Jaeger-Waldau, "PV Status Report 2016," *Publications Office of the European Union*, 2016.

[23] M. Richter, C. Tjengdrawira, J. Vedde, M. Green, L. Frearson, B. Herteleer, U. Jahn, M. Herz, and M. Köntges, "Technical Assumptions Used in PV Financial Models. Review of Current Practices and Recommendations," tech. rep., International Energy Agency, 2017.

[24] J. Mayer, "Current and Future Cost of Photovoltaics. Long-term Scenarios for Market Develpoment, System Prices and LCOE of Utility-Scale PV systems," tech. rep., Fraunhofer ISE, Berlin, 2015.

[25] B. Mihaylov, "Results of the Sophia module intercomparison part-1: stc, and temperature coefficients low irradiance conditions measurements of C-Si technologies," in *Proceedings of the 29th European Photovoltaic Solar Energy Conference and Exhibition*, (Amsterdam), pp. 2443 – 2448, WIP Renewable Energies Rights:, 2014.

[26] R. Valckenborg and B. van Aken, "Outdoor performance quantification and understanding of various PV technologies using the IEC 61853 matrix," in *36th European Photovoltaic Solar Energy Conference and Exhibition*, (Marseille), 2019.

[27] M. Joshi and S. Rajeev, "Reliable module temperature measurement: considerations for indoor performance testing," tech. rep., Black & Veatch, 2014.

[28] Y. Varshni, "Temperature dependence of the energy gap in semiconductors," *Physica*, vol. 34, pp. 149–154, 1 1967.

[29] M. Nell and A. Barnett, "The spectral p-n junction model for tandem solar-cell design," *IEEE Transactions on Electron Devices*, vol. 34, pp. 257–266, 2 1987.

[30] M. A. Green, "Solar cells—Operating principles, technology and system applications," *Solar Energy*, vol. 28, no. 5, p. 447, 1982.

[31] M. A. Green, "General temperature dependence of solar cell performance and implications for device modelling," *Progress in Photovoltaics: Research and Applications*, vol. 11, no. 5, pp. 333–340, 2003.

[32] M. Herman, M. Jankovec, and M. Topič, " Optimal I-V Curve Scan Time of Solar Cells and Modules in Light of Irradiance Level ," *International Journal of Photoenergy*, vol. 2012, pp. 1–11, 2012.

[33] A. M. Andreas and D. R. Myers, "Pulse analysis spectroradiometer system for measuring the spectral distribution of flash solar simulators," in *SPIE Proceedings volume 7046, Optical Modeling and Measurements for Solar Energy Systems II* (B. K. Tsai, ed.), (San Diego, California), p. 7046, SPIE, 9 2008.

[34] M. A. Green, "The Passivated Emitter and Rear Cell (PERC): From conception to mass production," *Solar Energy Materials and Solar Cells*, vol. 143, pp. 190–197, 2015.

[35] J. Trube, A. Metz, M. Fischer, A. Hsu, S. Julsrud, T. Chang, and B. Tjahjono, "International Technology Roadmap for Photovoltaic (ITRPV) 2016 Results," *International Technology Road Map for Photovoltaic*, 2017.

[36] P. J. Ribeyron, "Crystalline silicon solar cells: Better than ever," 2017.

[37] J. P. Seif, G. Krishnamani, B. Demaurex, C. Ballif, and S. De Wolf, "Amorphous/Crystalline Silicon Interface Passivation: Ambient-Temperature Dependence and Implications for Solar Cell Performance," *IEEE Journal of Photovoltaics*, vol. 5, no. 3, pp. 718–724, 2015.

[38] S. Sze and K. N. Kwok, *Physics of Semiconductor Devices*. Wiley, 3rd ed., 2007.

[39] M. Green, K. Emery, and A. Blakers, "Silicon solar cells with reduced temperature sensitivity," *Electronics Letters*, vol. 18, no. 2, p. 97, 1982.

[40] W. Hicks, "Little Uncertainty Remains at NREL, Thanks to Improvements in PV Performance Measurement," 2019.

[41] N. Blair, N. Diorio, J. Freeman, P. Gilman, S. Janzou, T. W. Neises, and M. J. Wagner, "System Advisor Model (SAM) General Description," no. NREL/TP-6A20-70414, 2018.

[42] B. Mihaylov, *Uncertainty considerations in photovoltaic measurements*. PhD thesis, Loughborough University, 2016.

[43] JCGM, "Guide to the expression of uncertainty in measurement," Tech. Rep. September, Joint Committee for Guides in Metrology, 2008.

[44] S. G. Kwak and J. H. Kim, "Central limit theorem: the cornerstone of modern statistics," *Korean Journal of Anesthesiology*, vol. 70, no. 2, p. 144, 2017.

[45] A. Edler, M. Schlemmer, J. Ranzmeyer, and R. Harney, "Understanding and overcoming the influence of capacitance effects of high efficiency silicon solar cells," *Energy Procedia*, vol. 27, pp. 267–272, 2012.

[46] B. Mihaylov, T. R. Betts, A. Pozza, H. Mullejans, and R. Gottschalg, "Uncertainty Estimation of Temperature Coefficient Measurements of PV Modules," *IEEE Journal of Photovoltaics*, vol. 6, no. 6, pp. 1554–1563, 2016.

[47] I. Smith and P. Harris, "NPL's Software to Support ISO/TS 28037:2010(E)," 2010.

[48] P. R. Guimaraes Couto, J. Carreteiro, and S. P. de Oliveir, "Monte Carlo Simulations Applied to Uncertainty in Measurement," in *Theory and Applications of Monte Carlo Simulations*, p. 13, InTech, 3 2013.

[49] C. Monokroussos, D. Etienne, K. Morita, V. Fakhfouri, J. Bai, C. Dreier, U. Therhaag, and W. Herrmann, "Impact of Calibration Methodology Into the Power Rating of C-Si Pv Modules Under Industrial Conditions," *28th European Photovoltaic Solar Energy Conference and Exhibition*, no. January, pp. 2926–2934, 2013.

[50] I. TC82, "IEC 60904-7: Computation of Spectral Mismatch Correction for Measurements of PV devices," tech. rep., 2008.

[51] C. R. Osterwald, M. Campanelli, T. Moriarty, K. A. Emery, and R. Williams, "Temperature-Dependent Spectral Mismatch Corrections," *IEEE Journal of Photovoltaics*, vol. 5, no. 6, pp. 1692–1697, 2015.

[52] Y. Hishikawa, M. Yoshita, H. Ohshima, K. Yamagoe, H. Shimura, A. Sasaki, and T. Ueda, "Temperature dependence of the short circuit current and spectral responsivity of various kinds of crystalline silicon photovoltaic devices," *Japanese Journal of Applied Physics*, vol. 57, no. 8, 2018.

[53] M. J. Moran and H. N. Shapiro, *Fundamentals of engineering thermodynamics*. John Wiley & Sons, 9th ed., 2010.

[54] C. Berthod, R. Strandberg, G. H. Yordanov, H. G. Beyer, and J. O. Odden, "On the Variability of the Temperature Coefficients of mc-Si Solar Cells with Irradiance," *Energy Procedia*, vol. 92, no. 1876, pp. 2–9, 2016.

[55] C. W. Hansen, M. Farr, and L. Pratt, "Correcting Bias in Measured Module Temperature Coefficients," tech. rep., Albuquerque, 2014.

[56] A. Abdallah, O. El Daif, B. Aïssa, M. Kivambe, N. Tabet, J. Seif, J. Haschke, J. Cattin, M. Boccard, S. De Wolf, and C. Ballif, "Towards an optimum silicon heterojunction solar cell configuration for high temperature and high light intensity environment," *Energy Procedia*, vol. 124, pp. 331–337, 2017.

[57] J. H. Wohlgemuth, *Photovoltaic Module Reliability*. John Wiley & Sons, 2020.

[58] D. W. Allen, G. P. Eppeldauer, S. W. Brown, E. A. Early, B. C. Johnson, and K. R. Lykke, "Calibration and characterization of trap detector filter radiometers," *Earth Observing Systems VIII*, vol. 5151, no. November 2003, p. 471, 2003.

[59] I. Rüedi and W. Finsterle, "The World Radiometric Reference and its quality system," *Proc. WMO Tech. Conf. on Meteorological and Environmental Instruments and Methods of Observation (TECO-2005), Instruments and Observing Methods, Bucharest, Romania, Government of Romania, Rep*, vol. 82, pp. 434–436, 2005.

[60] A. Fehlmann, G. Kopp, W. Schmutz, R. Winkler, W. Finsterle, and N. Fox, "Fourth World Radiometric Reference to SI radiometric scale comparison and implications for on-orbit measurements of the total solar irradiance," *Metrologia*, vol. 49, no. 2, 2012.

[61] J. Hohl-ebinger and W. Warta, "Uncertainty of the spectral mismatch correction factor in STC measurements on photovoltaic devices," *Progress in photovoltaics: research and applications*, vol. 19, no. January, pp. 573–579, 2011.